# An approach of compartmentalisation in development of non-isothermal chemical reactor network models for the high speed simulation of iso-octane combustion

Zamier Ahmed Khan

Thesis submitted to University of Cape Town
in partial fulfilment of the requirements for the degree of

Master of Science
In
Chemical Engineering

Dr R Rawatlal

February 2011

**Abstract**

Every aspect of the modern day life relies on combustion, be it in motor vehicles, industrial equipment or power generation. The downside to the extensive use of combustion technology is the environmental pollution produced by the process. The lack of fast solving models to simulate combustion hampers the investigation into the optimisation of combustion processes. In this study, the compartment approach in developing a fast and accurate simulation is used to investigate combustion systems.

A chemical reactor network (CRN) is proposed for the simulation of the combustion of iso-octane. The compartmentalisation of a combusting system involves proposing a reactor network based on the flow fields predicted by computational fluid dynamics (CFD). The first step in the development of such a model involves using of a reduced kinetic model representing thousands of combustion steps in a few elementary steps by lumping species. The reduced kinetic model used in this study consists of a five-step mechanism involving four pseudo species. The thermodynamic properties of the pseudo species in the system were regressed against experimental data and successfully validated using the plug flow and continuous stirred tank reactor sub-models. The reduced kinetic model was also further validated using Rapid Compression Machine data.

The current study also modified the methodology for developing a CRN in order to make the CRN more predictive as compared to previous studies. This was achieved by incorporating non-isothermal sub-models into the network instead of isothermal sub-models that rely on the CFD temperature field. The network parameters were also correlated to the inlet Reynolds number in order to further increase the predictive nature of the network for industrial applications and to allow for the systems performance to be predicted over a wide range of input conditions.

The investigation begins by conducting a CFD simulation of iso-octane combustion in a furnace and double inlet reactor assuming a one-step global reaction. On the basis of the CFD flow fields, a CRN was proposed and coupled to the reduced kinetics.

The resulting CRN for the furnace geometry and double inlet geometry was simulated and compared with that from CFD simulation. The CRN for the double inlet reactor revealed that the network parameters were not dependent on the inlet velocity thus the network was not correlated to the inlet Reynolds number.

However, the CRN for the furnace does depend on the inlet velocity and was correlated to the inlet Reynolds number. Both predictions for the furnace and double inlet reactor showed good agreement with the CFD data generated with the prediction of the CRN converging orders of magnitude faster than the CFD model. The correlated furnace network was also simulated and compared to the CFD results. Good agreement of CRN to the CFD model was found to be limited to a subset of inlet Reynolds numbers, mainly

lower Reynolds numbers since the CRN prematurely predicts the flame front at high Reynolds numbers. The novel cross-correlation of the network to an inlet condition of the furnace allows the CRN to adapt its temperature prediction orders of magnitude faster than the CFD.

Using compartmentalisation as a tool to investigate the hydrodynamics and a reduced kinetic mechanism coupled to the network, a fast solving combustion model has been developed that can be applied to a wide variety of combustion systems ranging from the simple (double inlet reactor) to the complex (industrial furnace). The fast solving combustion model makes real time optimisation of a system possible.

# Acknowledgements

Firstly I would like to give thanks to God without which nothing is possible. I wish to thank my parents for their invaluable support, inspiration and encouragement throughout my academic career.

I would like to thank the people who have helped and supported me throughout this study. I am grateful to my supervisor for his continuous direction and support from the initial concept phase to the final result. Without your guidance, the project would not have gone as smoothly.

To the modelling group at the University of Cape Town, our discussions and debates have played a significant role in the development of the ideas used in my project. Last but not the least I would like to thank my friends who kept me motivated to complete this study.

# Contents

# List of Figures

# List of Tables

# Part I

# Background

# Chapter 1

# Introduction

## 1.1 Background to the study

Every aspect of the modern day life relies on combustion, be it in motor vehicles, industrial equipment or power generation. The downside to the extensive use of combustion technology is the environmental pollution produced by the process. The possibility of global warming has seen new legislation being implemented to govern the pollutant emissions from combustion processes (Law, 2007). Fuel type, fuel blend composition, optimum air to fuel ratio in an engine, the effect of additives on pollutant formation are just a few of the parameters that can significantly affect the performance of a fuel. Understanding how these factors affect the combustion process is fundamental in reducing emissions and subsequently making the process more efficient.



## 1.2 Current Developments

There are two pathways taken to investigate combustion phenomenon, namely, experimental and computational methods. The experimental pathway requires data to be generated from the combustion equipment. Obtaining the data is time consuming and has large variations making the conclusions drawn via this method subject to error. An alternative to experimental analysis is to employ computer simulations to generate data. Computer simulations are significantly faster and yield accurate results provided the models used are applicable to each specific case.

There are various challenges associated with simulating a combustion event, namely, the numerical difficulty in integrating large systems of non-linear partial differential equations (PDE's), complex chemical kinetics and computational fluid dynamics. The kinetics of combustion require a detailed understanding of the chemical pathways that occur during a combustion event. Numerous studies have attempted a detailed modelling of primary reference fuel oxidation with varying success (Callahan et al., 1996, Curran et al., 2002).

The pathways usually include a large number of intermediate species and free radical molecules (Griffiths, 1994). Although combining this detailed chemical kinetic mechanism with the fluid flow is the most rigorous way of simulating combustion, it is the most computationally expensive. In general, the more detailed and fundamental the system of equations to be numerically solved, the larger the computational demand. Simplifications have to be made to alleviate the computational demand and obtain a fast and accurate solution. As the computational power of modern computing systems increase, the predictive speed of a reduced combustion will make real time optimisation of chemical processes possible.

One such approach is to simplify the kinetics by making use of a reduced kinetic mechanisms. The reduced kinetic mechanism maintains the most important features of the detailed mechanism but uses a smaller set of intermediates species and pseudo species in the mechanism. This is achieved by linking the kinetic parameters of the lumped reactions to the detailed scheme (Ranzi et al., 1997). The smaller set of chemical species can be incorporated into the fluid model with a significant improvement in computer performance.

Another recent development to ease the computational demand associated with combustion modelling is to use a compartmental approach to model the hydrodynamics of the system (LeMoullec et al., 2010, Falcitelli et al., 2002a). Traditionally, the hydrodynamics of the combustion system is modelled by the complete and rigorous set of Navier-Stokes equations with additional sub-models integrated within its broad framework making a quick analysis of the results very difficult (Westbrook et al., 2005). The network of ideal reactors serves as a surrogate to the rigorous Computational Fluid Dynamics approach. The nodes of the chemical reactor network (CRN) consist of either a plug flow reactor (PFR) or a continuous stirred tank reactor (CSTR) (Ponsich et al., 2009). These idealised reactor models may converge to solution in the order of seconds, thus avoiding the heavy computational demands otherwise required. Small-scale CFD simulations are first conducted assuming a simplified global expression for the kinetics to obtain the vector fields for the system where after a chemical reactor network is proposed from the CFD flow fields and coupled to a reduced kinetic mechanism for iso-octane.



## 1.3 Description of Combustion Systems

To explain the different levels of combustion simulation, lets consider the jet engine shown in Figure 1.1. Air is taken in and compressed by the fan blades. The compressed air is used as the oxidant in the combustion reaction. Jet fuel is injected into the combustion chamber after which it ignites. The reaction releases energy which is transferred to the turbines. The rotation of the turbine increases the speed of the compression step since turbine is attached to a central rotating axle that connects to the compressor. The exhaust

gases are then discharged from the unit.

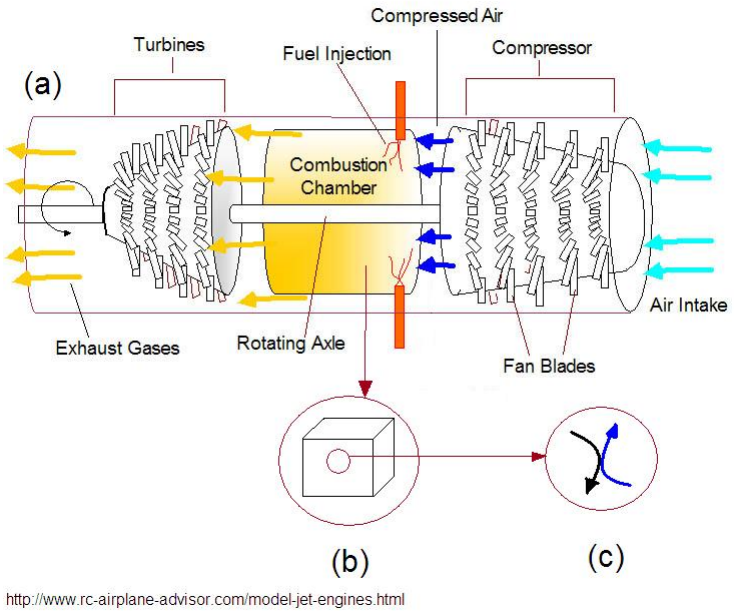


**Figure 1.1:** Schematic of a jet engine

The combustion event in Figure 1.1 can be described at three different levels namely macroscopic, microscopic and molecular.

### 1.3.1 Macroscopic Level

At the macroscopic scale (Figure 1.1a), a high level approach is adopted. Only the overall change (e.g. Temperature, pressure, concentrations) in the system is considered thus the detailed hydrodynamic information of the system is not calculated. The system is usually assumed to be at steady state.

### 1.3.2 Microscopic Level

At the microscopic scale (Figure 1.1b) the system is divided into smaller sub-volumes. Conservation equations are then written on each sub-volume. The aim here is to determine the velocity, temperature, pressure, and concentration profiles within the jet engine. These fundamental conservation equations written on this level is commonly known as the Navier-Stokes equations (Bird et al., 2002).

### 1.3.3 Molecular Level

Figure 1.1c shows a schematic representation of a fuel molecule colliding with an oxygen molecule. At the molecular scale (Figure 1.1c) we seek a fundamental understanding of the mechanisms of mass, energy, and momentum transfer in terms of molecular structure

and intermolecular forces (Bird et al., 2002). The chemical kinetics of the combustion process is particularly important at this level.

## 1.4 Computational Fluid Dynamics

The hydrodynamics of the combustion system are investigated using the laws that govern the conservation of mass, momentum and energy to solve the fluid dynamics component of the combusting system. The conservation of mass is given by Equation 1.1.

$$\frac{\partial \rho}{\partial t} + \nabla \cdot \rho v = 0 \tag{1.1}$$

(Bird et al., 2002)

Equation 1.1 states that the mass in the system is neither created nor destroyed. Although the total mass in the system remains conserved, the identity of the mass may change in terms of species concentrations. A transport equation that maintains the species mass is given by Equation 1.2

$$\frac{\partial \left(\rho m_i\right)}{\partial t} + \nabla \cdot \left(\rho v m_i\right) = \nabla \cdot \left(\rho D_{im} \nabla m_i\right) + r_i \tag{1.2}$$

where $t$ is time, $\rho$ is fluid density, $m_i$ is the mass fraction of species $i$ and $v$ is fluid velocity. The term $r_i$ is the chemical source term given in terms of species concentrations. The larger the quantity of species that are present in the kinetic mechanism, the more transport equations and function evaluations are needed to solve the system of equations and to evaluate the chemical source term (Law, 2007). Therefore simplifying the kinetics of combustion is crucial in reducing the computational demand.

The momentum balance in vector-tensor notation is given by Equation 1.3.

$$\frac{\partial \rho \boldsymbol{v}}{\partial t} = -\left[\nabla \cdot \rho \boldsymbol{v}\boldsymbol{v}\right] - \nabla p - \nabla \cdot \tau + \rho \boldsymbol{g} \tag{1.3}$$

The energy balance in terms of temperature for chemically reacting flow has been derived by Peters 2000 and is given by Equation 1.4.

$$\rho c_p \frac{\partial T}{\partial t} + \rho c_p \boldsymbol{v} \cdot \nabla T = \frac{\partial P}{\partial t} + \nabla \cdot (\lambda \nabla T) - \sum_{i=1}^{n} c_{pi}\, j_i \cdot \nabla T - \sum_{i=1}^{n} h_i r_i + q_r \tag{1.4}$$

The system of PDE's are solved using the numerical methods available in a CFD package (Fluent). An example of the CFD fields of an oxidiser is shown in Figure 1.2.

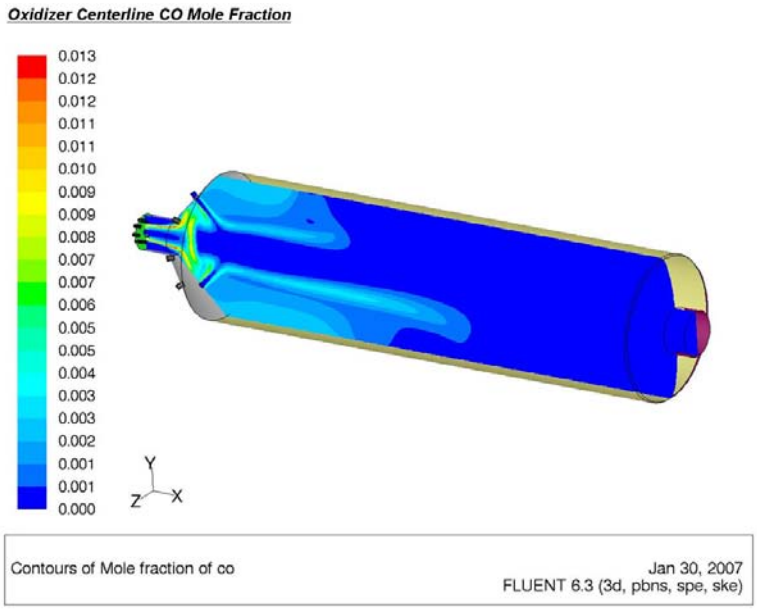


**(a)** Mole fraction of $CO$ in an oxidiser

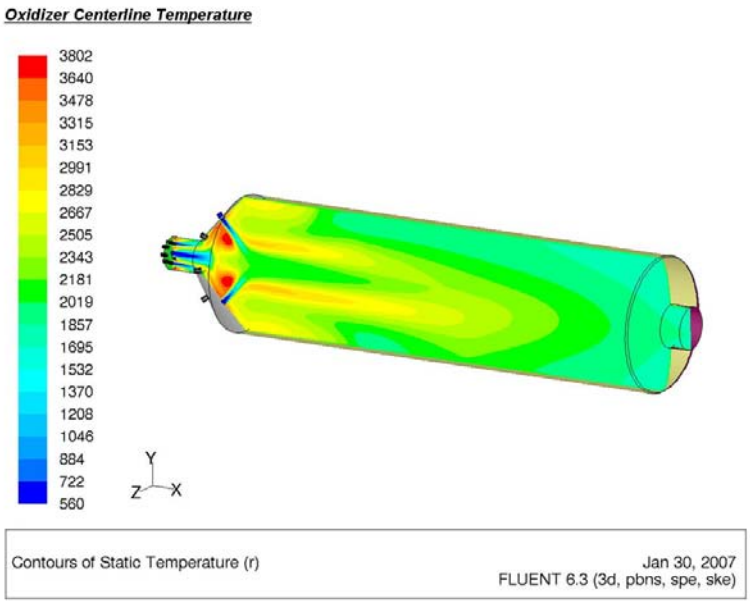


**(b)** Temperature in an oxidiser

**Figure 1.2:** CFD results for an oxidiser (http://www.gtkflow.com/index.html)

Figure 1.2 shows the concentration profiles and temperature profiles in the system. The profiles obtained from the CFD are coupled to the kinetics through the chemical source term. Thus, the kinetics are important in simulating any combustion event.

## 1.5 Combustion Theory

Before any kinetic mechanisms can be considered for a combustion event, the theory regarding flames has to be understood. The combustion reaction can be written in the

general mass exchange form given by Equation 1.5 where

$$1\ kg\, fuel + r\ kg\, oxidant \rightarrow (1+r)\ kg\, product \tag{1.5}$$

1 $kg$ of fuel reacts with $r$ $kg$ of oxidiser to form $(1+r)$ $kg$ of product. The process is an exothermic chemical reaction releasing thermal energy. The oxidiser used is usually air consisting of approximately 21% oxygen and 79% nitrogen by volume. Nitrogen is assumed to be an inert material in the combustion process but at high temperatures small amounts of nitrogen may react to form NOx in small quantities which are important in pollution analysis.

For a given fuel, it is important to know the quantity of oxygen or air that is required for complete combustion. The fuel to air ratio provides this relation and is given by Equation 1.6

$$\phi = \frac{\left(\frac{m_f}{m_o}\right)}{\left(\frac{m_f}{m_o}\right)_{stoich}} \tag{1.6}$$

where $m_f$ is the mass of fuel and $m_o$ is the mass of oxidiser. If $\phi < 1$, the mixture is lean in fuel. If $\phi > 1$, the mixture is rich in fuel. Combustion with a lean fuel mixture results in excess oxidiser remaining at the end of the combustion process. Combustion with a rich fuel mixture results in incomplete combustion due to the oxidiser being the limiting reactant.

The combustion reaction can either occur in self-ignition method or by forced ignition. In self-ignition, a reactive mixture is heated until the temperature reaches a critical point that spontaneously ignites the mixture. In the forced ignition method, a small quantity of combustible mixture is heated by an external source and the heat released during the combustion of this portion results in propagation of a flame (Kirk-Othmer, 2001). Combustion can occur either in a flame or non-flame mode. This is illustrated in Figure 1.3.



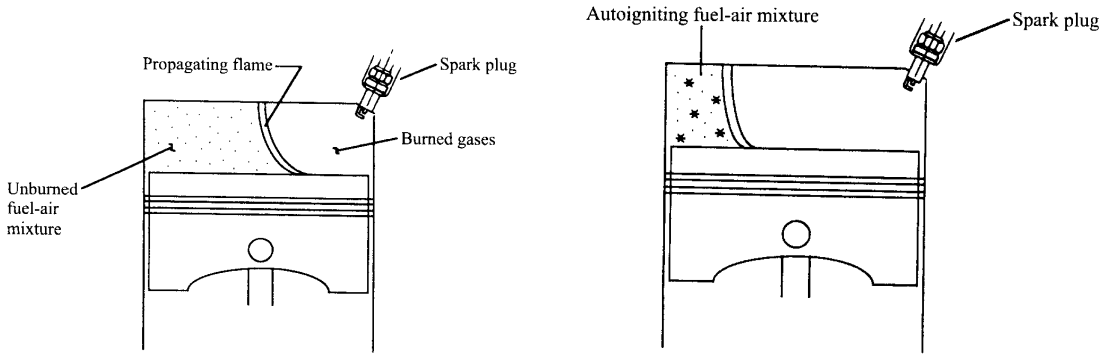


**(a)** Flame **(b)** Non-flame

**Figure 1.3:** Combustion modes (Turns, 2000)

When the reactants are combusted, a wave propagates through the unburned mixture of air and fuel. A thin reaction zone is commonly called the flame. Behind the flame are combustion products and ahead of the flame is unreacted fuel (Figure 1.3a). When the unreacted fuel starts to auto-ignite, the flame is disrupted resulting in non-flame combustion (Figure 1.3b).

The flame mode can be subdivided into premixed and non-premixed (diffusion) flames. These two flames relate to the mixed nature of the reactants. In a diffusion flame, reactants are initially separated and the reaction occurs only at the interface between the fuel and the oxidiser. A premixed flame however has a predefined fuel-air mixture that is either spark ignited or compression ignited (Turns, 2000).

Now that the flame modes have been understood, the kinetic steps for a combustion process is further explained. The combustion steps form the basis of most chemical kinetic mechanisms.

The ignition process is very sensitive to the gas temperature, pressure and surfaces the gas is in contact with. At ambient temperatures the reaction rate and heat released from the reaction of fuel with oxidant is very low. The slow oxidation region can be seen in Figure 1.4.

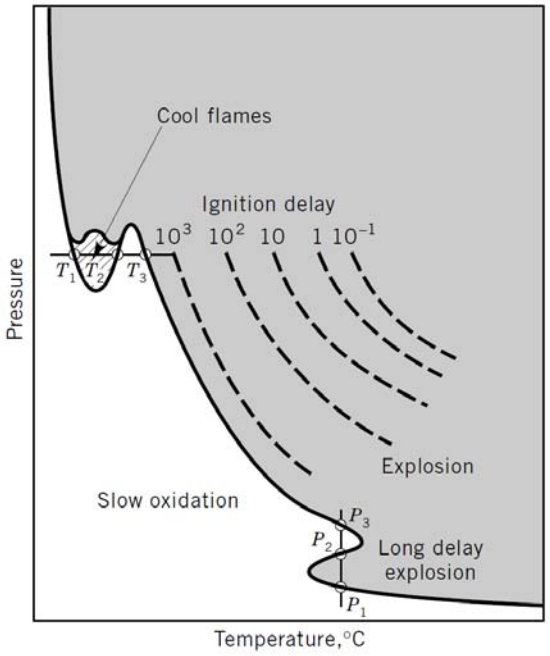


**Figure 1.4:** Pressure and temperature variations in explosive hydrocarbon mixtures (Kirk-Othmer, 2001)

The slow oxidation step generates free radicals ($OH$, $H$, $O$, $HO_2$, hydrocarbons) and other intermediate species ($CO$, $H_2$, and partial oxidation and decomposition products of hydrocarbons, if present) (Kirk-Othmer, 2001). The temperature may or may not rise at this point since the energy is essentially being stored in the free radicals. This behaviour

is termed cool flame behaviour. The cool flame can be seen on the homogeneous charge compression ignition (HCCI) pressure trace shown in Figure 1.5. The pressure does not rise as the temperature rises. This behaviour can also be seen as the temperature rises from $T_1$ to $T_3$ in Figure 1.4.

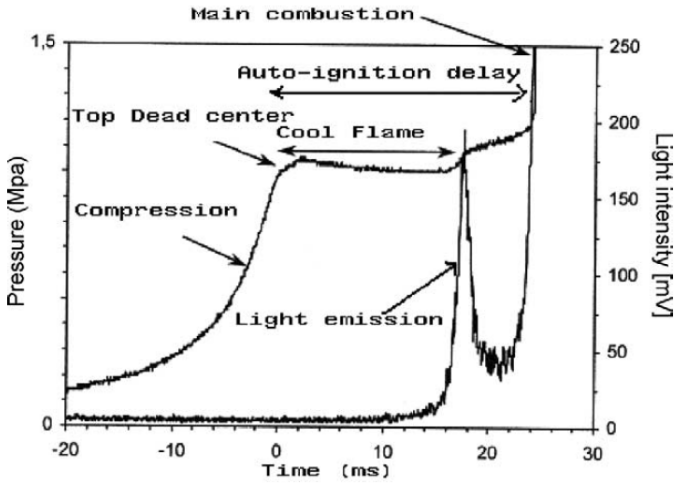


**Figure 1.5:** Cool flame in a HCCI (Machrafi et al., 2005)

The heat generated from the reaction has to be greater than the heat being dissipated through surfaces in contact with the reactive mixture for autoignition to occur. In an adiabatic system, autoignition is guaranteed. If there is a slight temperature rise as a result of the slow oxidation reactions, the cool flame behaviour is disrupted. The intermediates and fuel then reacts with the radicals. The intermediates and fuel become consumed in these reactions to form stable species by three-body recombination reactions in which most of the heat release occurs (Kirk-Othmer, 2001).

An example of such a reaction, where $M$ is any atom or molecule in the gas, is represented by

$$H + OH + M \rightarrow H_2O + M \tag{1.7}$$

(Kirk-Othmer, 2001). The temperature then reaches a critical point (ignition temperature) where the energy released is greater than the critical energy of ignition. This is indicated by the solid line between the slow oxidation and explosion zone shown in Figure 1.4. At this point, the reaction rate increases rapidly causing a large temperature rise. The fuel is either completely combusted or partially combusted depending on the fuel to oxidant ratio of the reactive mixture.

The time taken for the ignition to occur is termed the ignition time delay. One such method to quantify the ignition time delay is presented in section 1.6. In order to understand the chemistry involved in the cool flame and autoignition of fuels, chemical kinetic mechanisms have been developed for simulation purposes.

## 1.6 Rapid Compression Machine

The Rapid Compression Machine (RCM) is able to simulate a single compression event. The compression event is able to measure the ignition time delay as explained before. It is this simplified compression event that allows for the simulation of adiabatic compression and ignition. The RCM is recognised as a useful research tool that can offer advantages over the direct use of fired or motored engines, since they provide a better control of experimental parameters such as air-fuel ratio, initial temperature and initial pressure (Chen and Karim, 1998). An experimental setup of the RCM is presented in Figure 1.6.

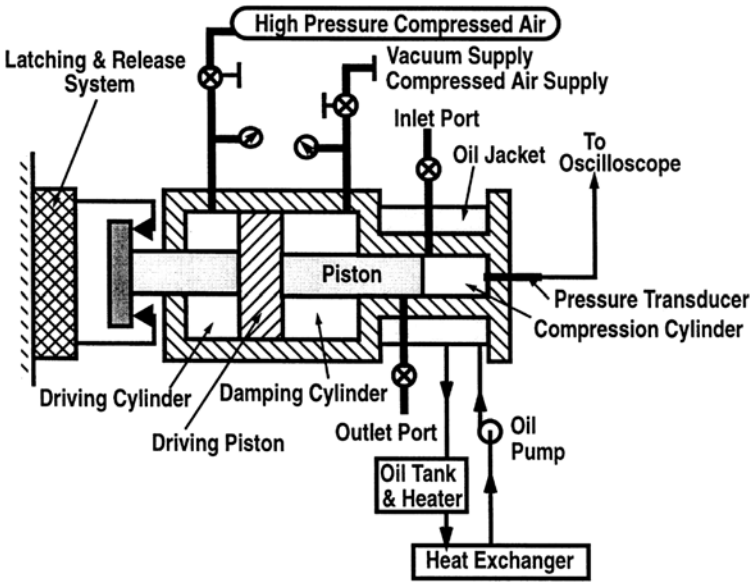


**Figure 1.6:** Schematic diagram of the rapid compression–expansion machine and peripheral equipment (Chen and Karim, 1998)

The RCM is operated as follows. Enclosed gases in the reaction chamber are compressed to high pressure and temperature in a few milliseconds and the reaction is allowed to proceed in a constant volume, constant mass chamber (Mittal, 2006). The piston has to achieve high velocities in order to avoid significant heat loss and also reactions from happening before reaching its end position. A pneumatically driven piston is able to reach the required piston velocity. It is this rapid compression that results in the reactive mixture being auto-ignited. The peripheral equipment allows for the determination of the pressure, temperature, velocity distribution and constituent composition at the start of compression precisely (Chen and Karim, 1998).

The temperature can not be directly measured within the compression chamber due to the mechanical limitations of temperature measuring equipment. Thus, the primary experimental data obtained from the RCM consist of the pressure trace of a given reacting mixture. A typical pressure trace of a reacting mixture is shown in Figure 1.7.

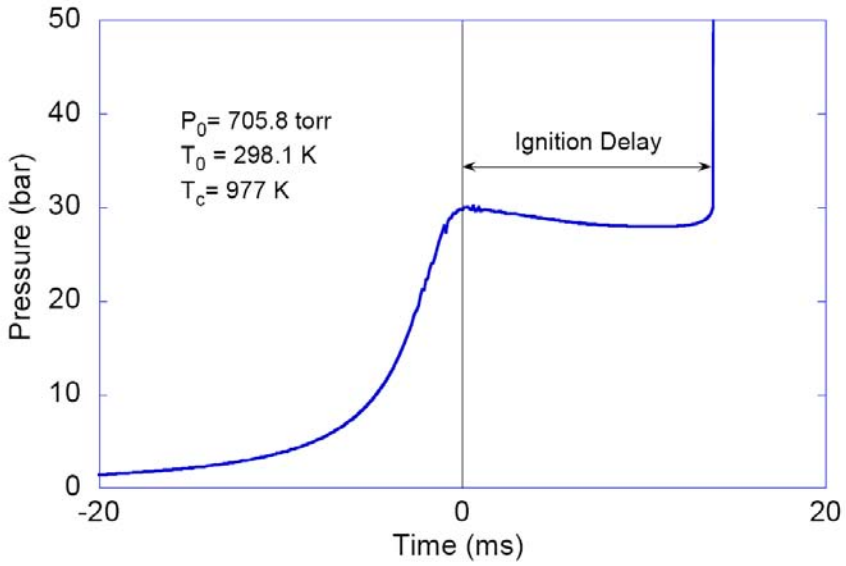


**Figure 1.7:** Typical Pressure trace during ignition of a reactive mixture in an Rapid Compression Machine (Mittal, 2006)

Looking at Figure 1.7, it can be seen that before autoignition takes place, there is a rapid rise in pressure due to compression. A gradual decrease in pressure is seen due to heat loss from the constant-volume chamber. When autoignition occurs, the pressure inside the RCM rises rapidly. The time period between the compression stroke and autoignition is the measured ignition delay.

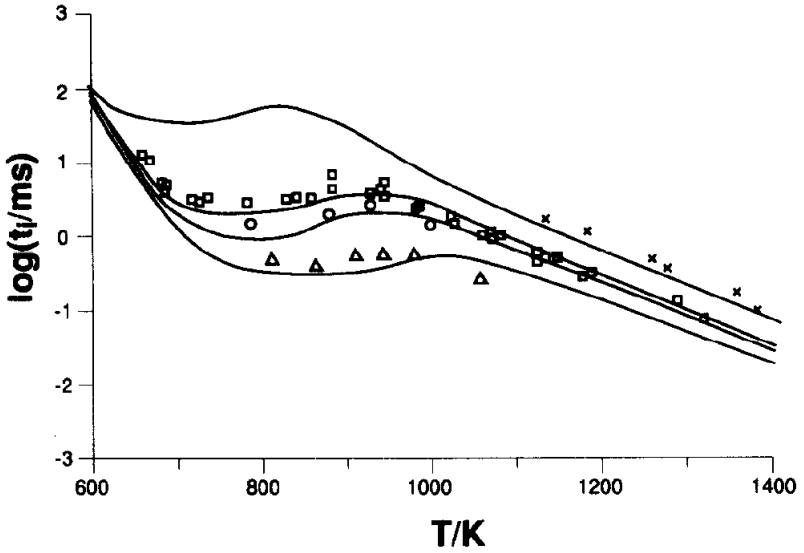


**Figure 1.8:** The experimentally-measured and numerically-predicted dependence of ignition delay during the oxidation of stoichiometric mixtures of n-heptane in air (Griffiths, 1994)

It is counter intuitive that the ignition time delay would increase with an increase

in temperature. This phenomenon is called the negative temperature coefficient region (NTC). Figure 1.8 shows the NTC for n-heptane. The increase of ignition delay time in the NTC region is associated with a lengthening of the duration of the second stage of reactions as explained in section 1.5 (Griffiths, 1994). Using the RCM ignition time delay data, a chemical kinetic mechanism for n-heptane can be proposed and modelled comparing it to the experimental ignition time delay. In this way, the kinetic mechanisms are usually validated.

## 1.7 Concluding Remarks

A preliminary investigation into the simulation of a combustion event revealed that the kinetics of combustion are very complex. Coupling the complex kinetics to the existing methods for hydrodynamic investigation (computational fluid dynamics) renders the task of simulating a combustion event computationally expensive. These challenges have provoked research over decades to reduced the complexity of the kinetic mechanisms and to ease the evaluation of the hydrodynamics. The current study will investigate these aspects in order to develop a faster solving combustion model.

# Chapter 2

# Literature Review

The task of reducing the computational demand associated with combustion modelling focuses on two key elements, the kinetic mechanisms and evaluation of the hydrodynamics. Over the past decades, strides have been made to alleviate the computational demand in these key areas. This section puts into context the advancements made in combustion simulation and highlights aspects of combustion modelling that can be further improved.



## 2.1 Chemical Kinetics

The chemical reactions that occur in chemically reacting flow systems can be divided into two categories, fast chemistry and finite rate chemistry. The fast chemistry approximation assumes that the chemical reaction is instantaneous. For the assumption of fast chemistry to hold, the system must be mixing controlled (Kee, 2003).

If the chemistry is kinetically limited, finite rate chemistry provides a good representation of the process. The finite rate chemistry can be further subdivided into detailed reaction mechanisms and reduced mechanisms.

There exists two levels at which analysis of finite rate chemistry can be conducted, namely detailed reaction mechanisms and reduced mechanisms. In the detailed reaction mechanisms, the chemistry is described by a collection of elementary reactions explained on a molecular level. Reduced mechanisms on the other hand use a subset of the detailed mechanism to describe the chemistry (Kee, 2003). A more detailed description of the two methods are described in sections 2.1.1 and 2.1.2. Both approaches assign an Arrhenius expression to describe the rate constant of each reaction as a function of temperature. A modified three parameter Arrhenius model is given by equation 2.1

$$k_{f,i} = A_i T^{\beta_i} exp\left(\frac{-E_i}{RT}\right) \tag{2.1}$$

where the pre-exponential factor is given by $A_i$, the temperature exponent $\beta_i$ $[-]$, and the activation energy $E_i$ $\left[\frac{kJ}{mol}\right]$. This modified Arrhenius expression is able to describe the

reaction rate over a wide range of temperatures.

### 2.1.1 Detailed Mechanisms

As mentioned previously, the detailed reaction mechanism approximates the chemistry of combustion by modelling the kinetics as a collection of elementary reactions on a molecular level. The task of writing a detailed chemical kinetic mechanism for the oxidation and combustion of hydrocarbons requires hundreds of elementary reactions to be considered. Attempts have been made to auto generate these mechanisms using an algorithm (Warnatz and Deutschmann, 2005, Battin-Leclerc et al., 2000). The coupling of the sub-mechanism from MOLEC and the handwritten $C_0$-$C_4$ sub mechanism for a branched paraffin fuel, i.e. iso-octane, produces a kinetic model for this fuel comprising of 3361 elementary reactions and among 950 species (Warnatz and Deutschmann, 2005).

Figure 2.1 shows a simplified scheme of the main reactions that govern the oxidation of alkanes. Chain carriers are mainly $\bullet OH$ radicals. Branching reactions are responsible for the multiplication of chain carriers and for an exponential acceleration of reaction rates, leading in some conditions to spontaneous autoignition or to cool flames as explained in section 1.5.

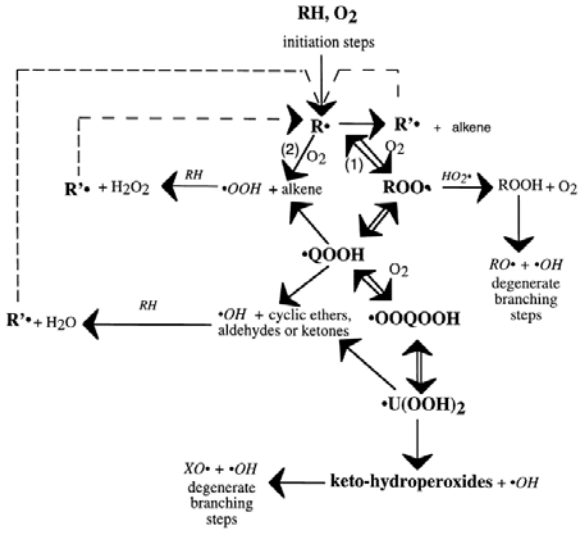


**Figure 2.1:** Simplified scheme for the primary mechanism of oxidation of alkanes (Broken lines represent metathesis with the initial alkane RH) (Battin-Leclerc et al., 2000)

Detailed kinetic models can also be used to describe gas phase reactions and that allow for the formation, growth, and oxidation of combustion particles ( Singha et al., 2005, Grosschmidt et al., 2007, Zucca et al., 2006, ). The uncombusted carbon particles are termed, Soot particles.

For a detailed reaction mechanism, the set of ordinary differential equation used to calculating the concentration of each species in the system is typically given by Equation 2.2

$$\frac{\partial Ct(i)}{\partial t} = \sum_{j=1}^{R} \left[ k_{j+} \prod_{products} Ct_p - k_{j-} \prod_{reactants} Ct_r \right] \tag{2.2}$$

where $R$ is the number of reactions in which the species $i$ is present, $k_{j+}$ and $k_{j-}$ are the forward and backward kinetic constants respectively, and $Ct_P$ (product) and $Ct_R$ (reagent) are the concentration of each species in the reaction (Duran et al., 2004). The detailed mechanism models the kinetics as a combination of aromatic and aliphatic hydrocarbon reactions where the aliphatic hydrocarbon reactions are modelled as combination of initiation, propagation, oxidation and pyrolysis reactions. The aromatic hydrocarbon reactions are modelled using initiation reactions as well as oxidation and pyrolysis reactions (Duran et al., 2004).

Mechanisms developed in this manner (Curran et al., 2002, Duran et al., 2004) correlate extremely well to experimental data and exhibit the phenomena of self ignition, cool flame, and NTC behaviour which have been discussed in the preceding sections. However, the number of species involved, both in the reaction base, in the primary and in the secondary mechanism, remain much too high to be introduced in computational fluid dynamics (CFD) codes for turbulent combustion (Battin-Leclerc et al., 2000). Using a reduced kinetic model for incorporation into a CFD package decreases the high computational demand. The theory of CFD is explained in section 2.2.

Due to the high computational demand of detailed mechanisms, a slightly reduced chemical kinetic model for the combustion of iso-octane and n-heptane has been proposed by Tanaka et al.. The reduced model includes 32 species and 55 reactions and a schematic diagram of the model is shown Figure 2.2.

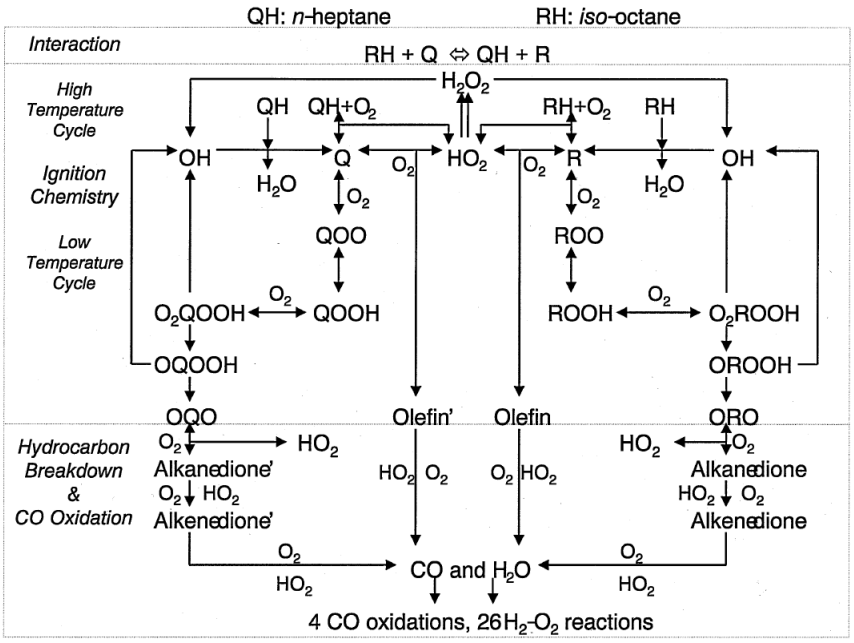


**Figure 2.2:** Reduced-chemistry for oxidation of n-heptane and iso-octane mixtures (Tanaka et al., 2003)

The results showed the well-known two-stage ignition characteristics of heavy hydrocarbons, which involve low and high temperature cycles followed by a branched chain explosion (Tanaka et al., 2003). The model proposed by Tanaka et al. also correlated well to the pressure profiles obtained in the RCM experiments. The skeletal mechanisms is the first step towards investigating which chemical pathways to include in a reduced mechanism. However, skeletal mechanisms are not simplified enough to be incorporated into a CFD package.

### 2.1.2 Reduced Reaction Mechanism

The main objective in proposing a reduced kinetic model is to simplify the chemistry but at the same time maintain the key features of the detailed chemical kinetic models. The reduction process involves a two-stage procedure. First, a skeletal mechanism is established by removing all redundant species and reactions. Second, the skeletal mechanism is further reduced by order-of-magnitude approximations, resulting in the analytically reduced mechanism (Kee, 2003).

A semi-reduced (70 species, 210 reactions) and a skeletal (27 species, 29 reactions) chemical reaction mechanism for iso-octane was constructed from a semi-detailed iso-octane mechanism (84 species, 412 reactions) by Machrafi et al.. The semi-reduced and the skeletal chemical reaction mechanisms successfully predicted the ignition times obtained with the detailed Chalmers iso-octane mechanism for temperatures below 700 K. The reduced mechanisms are also in good agreement with the complete Nancy iso-octane

mechanism, but at inlet temperatures lower than 600 K. For HCCI purposes the reduced mechanism of 29 reactions can be perfectly used for future aerodynamics applications in CFD codes (Machrafi et al., 2005).

The arrival of a five step kinetic model has been summarised by Griffiths and is presented here. Muller et al. discuss a reduced kinetic model to represent the oxidation of n-heptane over the temperature range 700-1500 K. The mechanism derived is presented in Table 2.1.

| Step | Reaction | $-\triangle H(kJ/mol)$ | $Z(s^{-1})$ | $E/RT$ |
|---|---|---|---|---|
| 1 | $F \rightarrow X$ | $-709.9$ | $2 \times 10^{10}$ | 21650 |
| 2 | $X + 11O_2 \rightarrow P$ | 5213 | $2 \times 10^{6}$ | 7220 |
| 3 | $F + 2O_2 \rightarrow I$ | 53.9 | $2 \times 10^{12}$ | 21650 |
| 4 | $I \rightarrow F + 2O_2$ | $-53.9$ | $4 \times 10^{22}$ | 37285 |
| 5 | $I + 9O_2 \rightarrow P$ | 4449.2 | $5 \times 10^{7}$ | 13230 |

**Table 2.1:** Five step model (Griffiths, 1994)

The mechanism emulated the oxidation of $n - C_7H_{16}$ (F), yielding the intermediates $3C_2H_4 + CH_3 + H$ (X) at high temperatures and the free radical $OC_7H_{13}O_2H$ (I) at low temperatures. The final products (P) were deemed to be $7CO_2 + 8H_2O$.

The ignition delay obtained from the model was validated against experimental data obtained in a shock tube. The model failed to predict the ignition delays throughout the entire temperature range. The first variation was derived with detailed representations of the alkylperoxy isomerisation and oxidation steps, with the specific purpose of demonstrating the essential features that pertain to hydrocarbon oxidation (Griffiths, 1994). This expanded mechanism is shown in Table 2.2.

| Step | Reaction | $-\triangle H(kJ/mol)$ | $Z(s^{-1})$ | $E/RT$ |
|---|---|---|---|---|
| 1 | $F \rightarrow X$ | $-709.9$ | $2 \times 10^{10}$ | 21650 |
| 2 | $X + 11O_2 \rightarrow P$ | 5213 | $2 \times 10^{6}$ | 7220 |
| 3 | $F + 2O_2 \rightarrow 2RO_2$ | $-194$ | $5 \times 10^{7}$ | 20000 |
| 4 | $RO_2 \rightarrow QO_2H$ | $-31.4$ | $1 \times 10^{11}$ | 11000 |
| 5 | $QO_2H + O_2 \rightarrow O_2QO_2H$ | 130 | $5 \times 10^{6}$ | 3000 |
| 6 | $O_2QO_2H \rightarrow QO_2H + O_2$ | $-130$ | $1 \times 10^{11}$ | 12000 |
| 7 | $O_2QO_2H \rightarrow P + 2OH$ | 111 | $5 \times 10^{10}$ | 12000 |
| 8 | $F + OH \rightarrow RO_2 + P$ | 100 | $1 \times 10^{6}$ | 1500 |
| 9 | $QO_2H \rightarrow I$ | 96 | $1 \times 10^{11}$ | 8400 |
| 10 | $I + 9O_2 \rightarrow P$ | 4449.2 | $5 \times 10^{7}$ | 13230 |

**Table 2.2:** Reduced model showing alkylperoxy isomerisation and oxidation steps (Griffiths, 1994)

An abbreviated form of the model shown in Table 2.2 has also been developed in order to minimise the number of species, but to retain these essential features. This model is shown in Table 2.3 and is applicable for iso-octane.

| Step | Reaction | $-\triangle H(kJ/mol)$ | $Z(s^{-1})$ | $E/RT$ |
|---|---|---|---|---|
| 1 | $F \rightarrow X$ | $-709.9$ | $2 \times 10^{10}$ | 21650 |
| 2 | $X + 12.5O_2 \rightarrow P$ | 4709.0 | $2 \times 10^{6}$ | 7220 |
| 3 | $F + 2O_2 \rightarrow I$ | 53.9 | $3 \times 10^{12}$ | 21650 |
| 4 | $I \rightarrow F + 2O_2$ | $-53.9$ | $4 \times 10^{22}$ | 37285 |
| 5 | $I \rightarrow 2Y$ | $-60$ | $6 \times 10^{7}$ | 5000 |
| 6 | $Y + 0.5F + 11.5O_2 \rightarrow P$ | 3913.1 | $1 \times 10^{9}$ | 16500 |

**Table 2.3:** Six step model (Griffiths, 1994)

Species $Y$ represents a propagating species that is generated in the chain-branching process. In a kinetic sense, $Y$ might be regarded to be the $OH$ free radical, but the need to retain element and enthalpy balances requires that it is a 'lumped' representation for all of the intermediate products formed at this stage of the process (Griffiths, 1994). The reduced model presented by Griffiths maintains key combustion features and is simple enough to be incorporated into a computational fluid dynamic code.

A study done by Owston et al. compared a global mechanism to a reduced chemical mechanism. It was found that the global reaction mechanism failed to show the large heat release spike at the combustion wall as compared to using a more detailed chemical kinetics approach. However, the spike in the heat release rate at the walls when using a detailed chemical kinetics approach is due to the reduced reaction mechanism accounting for radical recombination and chain carrying reactions. The absence of these radicals results reduces the heat release rates for the global reaction mechanism (Owston et al., 2007). The comparison shows that the representation of flame dynamics requires a fairly detailed chemistry model although it is computationally demanding. Simple models may not represent the essential physics of the process so care has to be taken to calibrate the reduced model to a valid reference point i.e experimental data.

## 2.2 Computational Fluid Dynamics

Computational fluid dynamics (CFD) is a subset of fluid dynamics that uses numerical methods to solve problems that involve fluid flow. A complete CFD analysis consists of the following steps:

1. Pre-processing
2. Solver
3. Post-processing

In the pre-processing step, the geometry of the flow region (i.e., the computational domain) is created (Tu et al., 2008). The domain is then subdivided into smaller, non-overlapping sub-domains in order to solve the flow physics within the domain geometry that has been created; this results in the generation of a mesh (or grid) of cells (Tu et al., 2008).

The mesh is the domain over which the governing equations are solved. The Navier-Stokes (N-S) equations are the fundamental basis for CFD. These Navier-stokes equations are nonlinear partial differential equations that conserve mass, energy and momentum.

Before the system of equations can be solved, they are discretized over the cells. Three discretization methods that allow for the numerical solution of the N-S equations are namely the finite difference (FD), finite volume (FV) and finite element (FE) methods. All methods yield the same solution if the grid is adequately fine (Ranade, 2002).

However, some methods are more suitable to particular classes of problems than others (Ranade, 2002). Many well-established commercial codes adopt the finite volume method as their standard numerical solution techniques due to the speed of the discretization (Mattiussi, 2002). Once the equations are discretized, initial and boundary conditions are needed before proceeding to the solver step. During the solver step numerical methods are used to solve the equations (Tu et al., 2008). The results are then viewed in the post-processing step.



### 2.2.1 Laminar Navier-Stokes Equations

As mentioned before, the Navier-stokes equations are nonlinear partial differential equations that conserve mass, energy and momentum. The principle of conservation of mass states that mass is neither created nor destroyed. The mass continuity equation for each species in the domain is presented in Equation 2.3.

$$\frac{\partial (\rho m_i)}{\partial t} + \nabla \cdot (\rho v m_i) = -\nabla \cdot (j_i) + r_i \tag{2.3}$$

where $t$ is time, $\rho$ is fluid density, $m_i$ is the mass fraction of species $i$ and $v$ is fluid velocity (Ranade, 2002). Equation 2.3 states that the accumulation of a species in the

control volume equals the transport via bulk flow and diffusion plus any generation of that component. The bulk flow consists of convection (second term left-hand side of Equation 2.3) and diffusive fluxes, $j_i$ . The diffusive flux is composed of diffusion due to concentration gradients (chemical potential gradients), diffusion due to thermal effects and diffusion due to pressure and external forces, Equation 2.4,

$$j_k = -\rho D_{im} \nabla m_i - D_{iT} \frac{\nabla T}{T} \tag{2.4}$$

where $D_{im}$ is the diffusion coefficient for species $i$ in the mixture and $D_{iT}$ is the thermal mass diffusion coefficient for species $i$ (Ranade, 2002). In many cases the contribution of thermal diffusion is very small compared to the diffusive flux due to concentration gradients (Ranade, 2002). Thus the simplified species balance is given by Equation 2.5.

$$\frac{\partial (\rho m_i)}{\partial t} + \nabla \cdot (\rho v m_i) = \nabla \cdot (\rho D_{im} \nabla m_i) + r_i \tag{2.5}$$

Equation 2.5 can be coupled with the momentum and energy balance to solve for individual species mass concentrations in the domain. The chemical source term of species ($r_i$) is modelled using chemical kinetics of combustion which are explained in section 2.1.

The principle of conservation of momentum states that the rate of change of momentum has to be equal to the force (Newton's 2nd Law). The conservation equations for momentum and energy are derived in Bird et al. 2002. The $x$-momentum, $y$-momentum and $z$-momentum for the system is given by Equation 2.6, Equation 2.7, Equation 2.8.

$$\frac{\partial \rho v_x}{\partial t} = -\left( \frac{\partial \rho v_x v_x}{\partial x} + \frac{\partial \rho v_y v_x}{\partial y} + \frac{\partial \rho v_z v_x}{\partial z} \right) + \rho g_x \tag{2.6}$$

$$\frac{\partial \rho v_y}{\partial t} = -\left( \frac{\partial \rho v_x v_y}{\partial x} + \frac{\partial \rho v_y v_y}{\partial y} + \frac{\partial \rho v_z v_y}{\partial z} \right) + \rho g_y \tag{2.7}$$

$$\frac{\partial \rho v_z}{\partial t} = -\left( \frac{\partial \rho v_x v_z}{\partial x} + \frac{\partial \rho v_y v_z}{\partial y} + \frac{\partial \rho v_z v_z}{\partial z} \right) + \rho g_z \tag{2.8}$$

By writing the three momentum balances in vector-tensor notation, the total change of momentum per unit volume is given by Equation 2.9.

$$\frac{\partial \rho \boldsymbol{v}}{\partial t} = \underbrace{-\left[\nabla \cdot \rho \boldsymbol{v}\boldsymbol{v}\right]}_{Term\,1} \underbrace{-\nabla p - \nabla \cdot \tau}_{Term\,2} + \underbrace{\rho \boldsymbol{g}}_{Term\,3} \tag{2.9}$$

(Bird et al., 2002).

The physical interpretation of the various terms in the overall momentum balance equations is similar to conservation balances previously presented. Equation 2.9 states that the total change of momentum in a control volume is dependent on the rate of momentum addition by convection (Term 1), rate of momentum addition by molecular

transport (Term 2) and external forces on the fluid (Term 3).

In order to use these general momentum conservation equations to calculate the velocity field, it is necessary to express viscous stress terms in terms of the velocity field (Ranade, 2002). By relating the stress tensor to the strain-rate tensor, it is possible to describe the stress state in terms of the velocity field and the fluid viscosity (Kee, 2003). For one dimensional flow, this relation is given by Equation 2.10. For a three dimensional system, the relations become more complex.

$$\tau_{yx} = -\mu \frac{dv_x}{dy} \tag{2.10}$$

When deriving an energy balance on the control volume, the principle of conservation of energy states that energy can not be created or destroyed but merely converted from one form to another. The shell balance for mass and momentum can be extended to the conservation of energy in the same way as the previous balances. A more detailed and lengthy derivation is presented in Bird et al. 2002. For chemically reacting flow, the derivations are the same except that the heat flux now includes a species diffusive flux term is given by Equation 2.11

$$J = -\lambda \nabla T + \sum_{i=1}^{n} h_i \, j_i \tag{2.11}$$

where the heat flux is modelled using Fourier's Law. The energy balance in terms of temperature for chemically reacting flow has been derived by Peters 2000 and is given by Equation 2.12.

$$\rho c_p \frac{\partial T}{\partial t} + \underbrace{\rho c_p \boldsymbol{v} \cdot \nabla T}_{Term\,1} = \underbrace{\frac{\partial P}{\partial t}}_{Term\,2} + \underbrace{\nabla \cdot (\lambda \nabla T)}_{Term\,3} - \underbrace{\sum_{i=1}^{n} c_{pi} \, j_i \cdot \nabla T}_{Term\,4} - \underbrace{\sum_{i=1}^{n} h_i r_i}_{Term\,5} + \underbrace{q_r}_{Term\,6} \tag{2.12}$$

Equation 2.12 states that the change in temperature with time in the control volume is dependant on enthalpy due to convection (Term 1), pressure effects (Term 2), change in the enthalpy due to conduction (Term 3), diffusive mass fluxes (Term 4), chemical reaction (Term 5) and external heat source (Term 6). The laminar equations presented above forms the basis for turbulent combustion modelling.

### 2.2.2 Turbulent Flow Modelling

The preceding derivations are based on laminar flow conditions. Turbulent flow conditions are more frequently encountered in engineering applications such as combustion. The formation of turbulence results when instabilities in a flow are not sufficiently damped by viscous action and the fluid velocity at each point in the flow exhibits random fluctuations

(Turns, 2000). As the Reynolds number increases and the flow becomes more turbulent, the requirements on resolution become more and more stringent (Ranade, 2002). The number of grid points and the smallness of the time steps required to resolve all the relevant time and space scales of turbulent motion become to large for modern day computing (Ranade, 2002).

Due to the complex mathematical description for turbulent fluid flow, the current solution strategies are only able to provide approximations even for simple geometries. These errors are inherent in the modelling process since the complex turbulent flow is simplified in order to aid computer simulation. The formation of turbulence also breaks the fluid into many smaller fluid elements of varying size and length scales. These fluid elements are typically referred to as an eddy. In an eddy cascade, large Eddy's break up and give energy to smaller Eddy's and smaller Eddy's break up eventually dissipating the energy. In fully developed turbulent flow many eddies exist over a wide range of length scales. It is this wide range that makes turbulent flow difficult to simulate. The length scales are presented in Table 2.4 in descending order.

| | Name of Length Scale | Description |
|---|---|---|
| L | Characteristic width of flow or macro scale | Large length scale for largest eddy |
| $l_0$ | Integral scale or turbulent macro scale | Represents the mean size of large eddies |
| $l_\lambda$ | Taylor micro scale | Length scale related to the mean rate of strain |
| $l_K$ | Kolmogorov micro scale | Scale at which molecular effects are significant |

**Table 2.4:** Turbulence length scales

One approximation in turbulence modelling is to decomposed state variables ($\alpha$) into a mean ($\overline{\alpha}$) and a fluctuating component ($\alpha'$) as follows

$$\alpha = \overline{\alpha} + \alpha' \tag{2.13}$$

The fluctuation is then the difference between the mean value and the instantaneous value as shown in Figure 2.3.

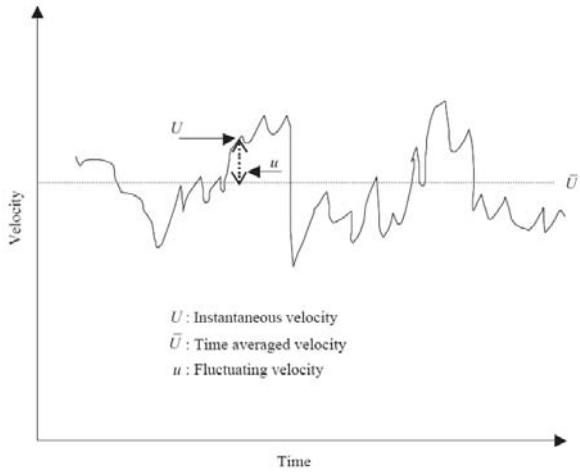


**Figure 2.3:** Typical point velocity behaviour in turbulent flows (Ranade, 2002)

The mean values are obtained by time-averaging of the variables over a large time interval as shown in Equation 2.4.

$$\tilde{p} \equiv \frac{1}{\triangle t} \int_{t1}^{t2} p(t)dt \tag{2.14}$$

(Turns, 2000). The resulting equations are called the Reynolds-Averaged-Navier-Stokes (RANS) equations. As an example, the averaged the continuity equation is presented:

$$\frac{\partial \bar{\rho}}{\partial t} + \nabla \cdot \left( \overline{\rho v} + \overline{\rho' v'} \right) = 0 \tag{2.15}$$

(Veynante and Vervisch, 2002). This procedure produces an extra term (Reynolds stresses $\overline{\rho' v'}$) that needs to be approximated (closure problem). One closure technique is to Favre average (mass weighted) the equations (Veynante and Vervisch, 2002). This method reduces the extra term to be independent of density (Reynolds stresses).

Other turbulent models have been developed that are able to simulate the Reynolds stresses by making them a function of dependent variables. The most widely used turbulence model is the $\kappa$-$\varepsilon$ model. Using the gradient transport assumption, the Reynolds stresses can be written as

$$\overline{\rho v' \alpha'} = -\bar{\rho} \nu_T \nabla \widetilde{\alpha} \tag{2.16}$$

where $\nu_T$ is the turbulent exchange coefficient and $\alpha$ being the state variables (Warnatz et al., 2006). The turbulent exchange coefficient can be calculated as follows

$$\nu_T = C_v \frac{\widetilde{\kappa}^2}{\widetilde{\varepsilon}} \tag{2.17}$$

The value of $C_v$ is 0.09. The two differential equations that govern the nature of the turbulent kinetic energy ($\widetilde{\kappa}$) and the dissipation of kinetic energy ($\widetilde{\varepsilon}$) are given as follows

$$\frac{\partial\left(\bar{\rho}\widetilde{\kappa}\right)}{\partial t}+\nabla\cdot\left(\bar{\rho}\boldsymbol{v}\widetilde{\kappa}\right)-\nabla\cdot\left(\bar{\rho}\nu_T\nabla\widetilde{\kappa}\right) = G_K-\bar{\rho}\widetilde{\varepsilon} \tag{2.18}$$

$$\frac{\partial\left(\bar{\rho}\widetilde{\varepsilon}\right)}{\partial t}+\nabla\cdot\left(\bar{\rho}\boldsymbol{v}\widetilde{\varepsilon}\right)-\nabla\cdot\left(\bar{\rho}\nu_T\nabla\widetilde{\varepsilon}\right) = \left(C_1G_K-C_2\bar{\rho}\widetilde{\varepsilon}\right)\frac{\widetilde{\varepsilon}}{\widetilde{\kappa}} \tag{2.19}$$

where $C_1$ and $C_2$ are empirically determined constants that are dependent on the system. The term $G_K$ is a complex function of the stress tensor and is presented as follows

$$G_K=-\overline{\rho\boldsymbol{v'}\otimes\boldsymbol{v'}}:\nabla\widetilde{\boldsymbol{v}} \tag{2.20}$$

An alternative to time-averaging is the direct numerical simulation (DNS). The complete time history of the flow profile is broken down to the Kolmogorov scale (Turns, 2000). This method is impractical in engineering applications but provide valuable information regarding turbulent flow fields. A more common engineering closure application is the use of the Large-eddy simulation (LES). The LES is a mixture between DNS and RANS. The flow is resolved to small length scales but not as low as Kolmogorov. LES is widely studied in terms of non-reactive flow but its applicability to combustion modelling is still at an early stage (Veynante and Vervisch, 2002). In LES, the relevant quantities are filtered in a spectral space (greater than a given cut-off frequency) or in physical space (weighted averaging). A graphical representation of the various methods are shown in Figure 2.4.

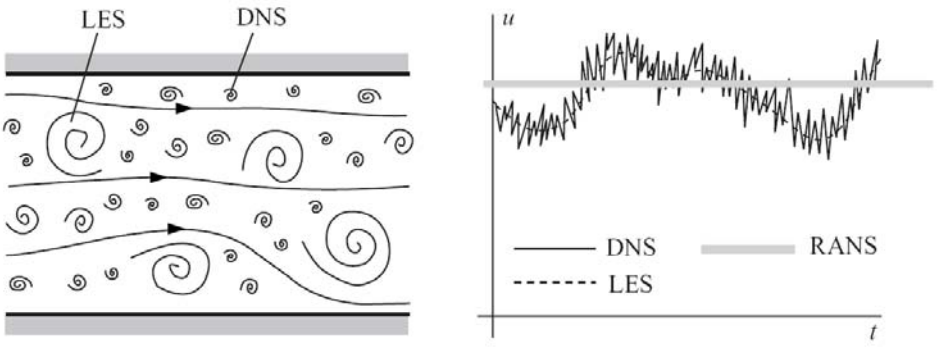


**Figure 2.4:** Schematic representation of scales in turbulent flows and their relationship with modelling approaches (Ranade, 2002)

The methods presented above for the evaluation of turbulent combustion variables is computationally expensive and only provide approximations even for simple geometries. Thus, an alternative approach to combustion modelling is needed to obtain fast solving models.

## 2.3 Critical Evaluation of Literature

Modelling chemically reacting fluid flow for combustion devices, such as engines, gas turbines and industrial furnaces requires that the conservation equations be solved in a three dimensional space including turbulence models and models that govern the kinetics of combustion. The full elementary kinetics mechanism of combustion is far to complex to be incorporated into CFD. Thus reduced models have been developed for such a purpose. These reduced mechanisms simplify the chemistry to increase the computational speed but maintain the salient features of the full elementary kinetics mechanism. These reduced mechanisms combined with CFD produces results that are comparable with experimental data but the computational demand is still too high. Dividing the flow regime into compartments provides an alternative to solving the hydrodynamics of the system. This is one option to ease the computational demand. Compartment modelling is described in section 2.4.

## 2.4 Compartment Modelling

As was discussed in the preceding sections, the simulation of industrial combustion equipment requires that the hydrodynamics be solved along with the kinetics of combustion. Compartment models have been used to understand the hydrodynamics in these imperfectly mixed reactive systems. Ideal reactor types are used as a compartmental unit. One method to establish a network of these ideal reactors is to use the residence time distribution (RTD). These concepts are discussed below.

### 2.4.1 Idealised Compartments

There are three ideal reactors namely used in proposing a chemical reactor network mainly

1. Batch Reactor
2. Plug Flow Reactor (PFR)
3. Continuous Stirred Tank Reactor (CSTR)

These reactors can be easily simulated and combined with reduced kinetic mechanisms. Each ideal reactor type is on the extremes of mixing characteristics. The batch reactor models chemical reaction without any fluid flow. The PFR models chemical reaction with fluid flowing only in the primary flow direction with strong mixing in a cross stream direction. The CSTR models chemical reaction in a completely mixed state. The CSTR may be used to model turbulence due to the assumption of complete mixing. Even for systems with highly complex fluid dynamics, where the flow cannot adequately be approximated by a single chemical reactor, a network of ideal reactors may form the basis of a useful approximation (Kee, 2003). Using these ideal reactor types in this network, the chemically reacting flow can be modelled using low dimensional representations. The RTD is one method for obtaining the reactor network.

The RTD measurements have to be interpreted taking into consideration the physical information about the process itself. A new algorithm for the automatic generation of compartment models based simultaneously both on RTD curves and physical description of the studied processes without mathematical fitting of the RTD curves was proposed by Claudel et al.. Using the RTD curves as a basis, a list of rules were fused together that leads to the selection of the most appropriate model reactor network model. A detailed review done by Claudel et al. of more than 120 publications dealing with RTD measurements shows that around 40 different compartment models allow to treat the major industrial situations. The review of literature also revealed that the models defined in the articles have at most five elementary reactors and three branches in parallel. Typical examples of models are given in Figure 2.5.

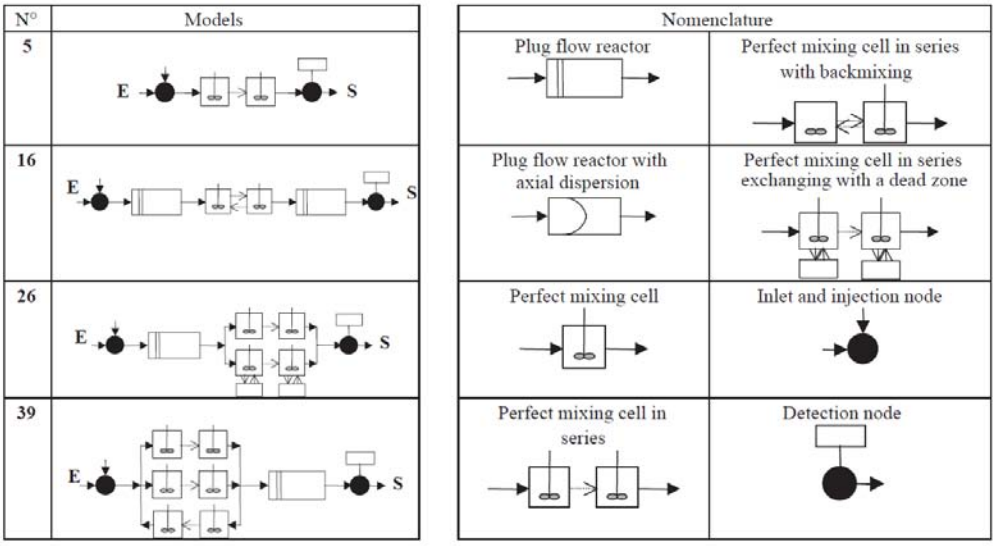


**Figure 2.5:** Examples of models chosen from literature (Claudel et al., 2003)



### 2.4.2 Reactor Network

Even with the RTD, the choice of the appropriate network to simulate the hydrodynamics may be troublesome when the considered reactor geometry is complex. An example of an imperfectly mixed reactor being modelled as a combination of ideal reactors was taken from Kee, 2003. Figure 2.6 shows a schematic of a confined, swirling, pulverised-coal flame.

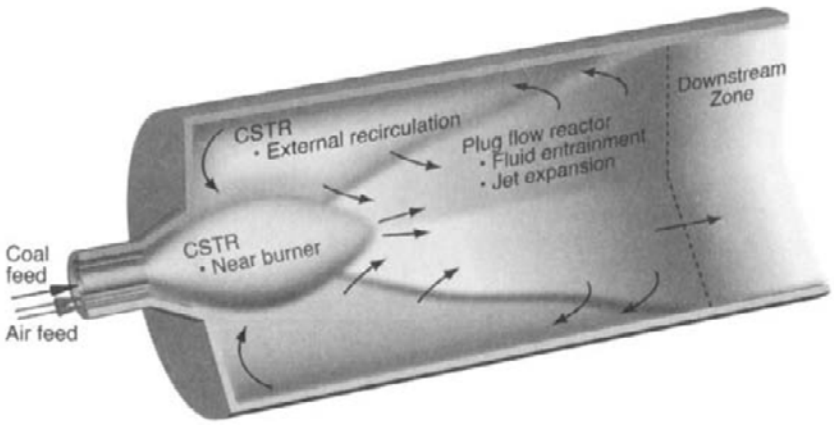


**Figure 2.6:** Schematic of a confined, swirling, pulverised-coal flame (Kee, 2003)

This reactor can be approximated by a network of ideal chemical reactors by observing the flow fields. Characteristic zones are identified in the flow fields where the ideal reactor types exist. A single converged CFD simulation can be used to propose a reactor network by looking at the flow fields. There exists four zones

1. Near burner
2. Jet expansion
3. External recirculation
4. Downstream

The near burner zone has a high degree of mixing and may be modelled as a CSTR. The jet expansion zone, which has a high axial velocity with some entrained fluid from the external recirculation entering the zone, may be described in terms of a non-ideal PFR. The external-recirculation zone, which is a highly dispersed region, is modelled as a single CSTR. The characteristics of the downstream zone depend on the geometry of the furnace.

A study done by Falcitelli et al. used 3D fields from a two glass melting furnace CFD simulation to propose an equivalent simplified flow model without using RTD. The study modelled methane combustion in a furnace. The furnaces were experimentally characterised, then CFD simulations were performed. The CFD simulations were done on a fine grid using the major species since the minor species have a negligible influence on the flow field and heat exchange. The effect of fuel oxidation on the flow field was observed. A reactor network was then extracted from the CFD flow fields. The proposed reactor network for the furnace is shown in Figure 2.7.

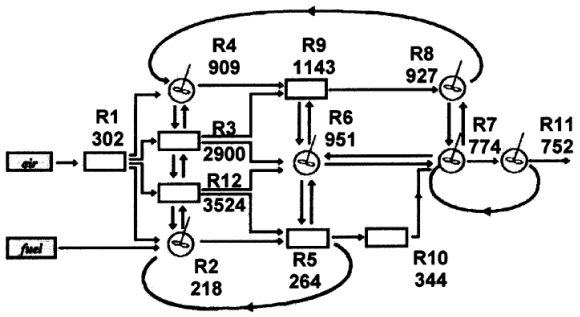


**Figure 2.7:** Reactor network produced by the procedure (Falcitelli et al., 2002b)

The proposed network for the furnace consisted of a 12 reactor network. A complex kinetic mechanism was then implemented on the network of chemical reactors. The results obtained were in very good agreement between measured and predicted NOx concentration in the exhaust (Falcitelli et al., 2002b).

In terms of computational demand, a 1000 fold increase in computational speed was achieved by proposing a compartment model for low density polyethylene (LDPE) autoclave reactor (Wells and Ray, 2005). Wells and Ray used a commercial finite volume CFD package (Fluent8 version 6.0.2) to simulate the CFD. The converged CFD solution was then used to propose a network of CSTR as shown in Figure 2.8.

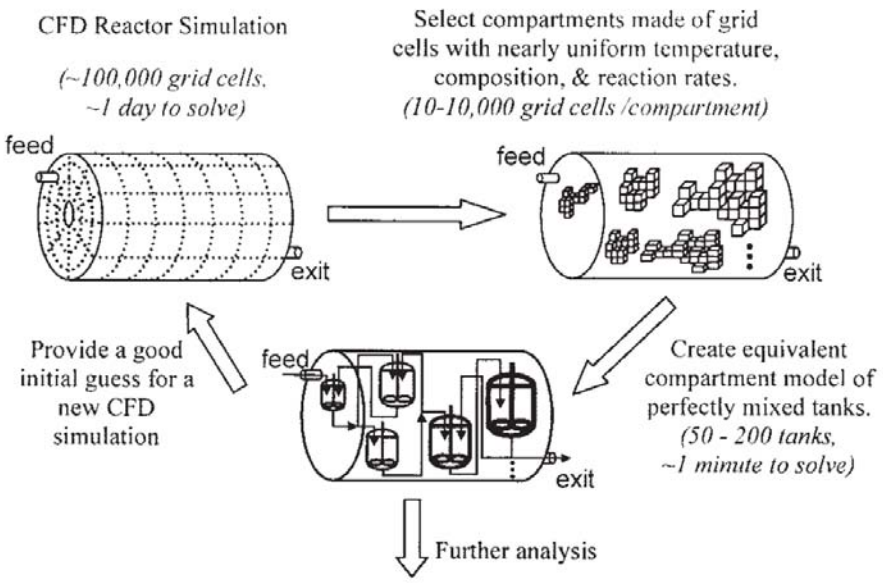


**Figure 2.8:** Procedure for selecting and using a compartment model (Wells and Ray, 2005)

The network consisted of 100 interconnected, perfectly mixed tanks that could accurately capture the spatial variations in temperature, conversion, and live chain concentrations found using complex CFD models. The results obtained from compartment models showed that they capture the accuracy and detail of CFD simulations over a wide range of LDPE reactor operation. The limitations on using the compartmental model lie in the reliability of the CFD simulation and the detailed kinetic scheme used.

# Chapter 3

# Thesis Objectives

In order for optimisation studies to be carried out on combustion equipment, fast solving models are needed. However, the lack of fast solving models hampers these investigations. In this study a compartment approach is investigated in developing a fast and accurate simulation that can be used for more extensive optimisation. The compartmentalisation of a real reactor is constructed from a network of ideal reactors.

The ideal reactors vary in function from perfectly mixed to plug flow behaviour. Each reactor will need to be modelled from fundamental mass and energy balance equations to gain a full understanding of factors influencing its operation. The level of kinetics used in each reactor will need to be sufficient enough to describe the major characteristics of combustion but remain computationally inexpensive. The reduced kinetic model developed by Schrieber et al. (1994) satisfies the criterion and will be used in this study. The dynamics of combustion using a reduced model is important in terms of steady state analysis, fuel and oxygen consumption and product formation pathways. Very little attention has been paid to this area in almost all previous combustion models and is not well understood. This study will also investigate the dynamics behind combustion and possibly explain some factors that influence the combustion process. The model proposed by Schrieber et al. (1994) uses pseudo species to reduce the amount of intermediates present in the mechanism. These pseudo species have no physical or thermodynamic properties which are essential in ideal reactor models. Approximations can be made with regard to some properties whereas other properties may need regression. The regression will be conducted against suitable combustion data. Once confidence is gained in the physical and thermodynamic properties, the ideal reactor models can be simulated to form the nodes of the compartmentalisation network.

The network for compartmentalisation is proposed as an equivalent to the CFD hydrodynamics. The methodology available in literature has been modified to make the network proposed in the current study more predictive. The network parameters are also correlated to the input Reynolds number thus expanding the predictive ability of the network. A simplistic and a more complex geometry is investigated for compartmentalisation.

# Part II

# Model Development

# Chapter 4

# Kinetic Model

Many studies have done a detailed modelling of primary reference fuel oxidation with varying success (Callahan et al., 1996, Curran et al., 2002). Such models involve thousands of elementary reactions, hundreds of species and reaction pathways that usually include a large number of intermediate species and free radical molecules (Griffiths, 1994). Although integrating a chemical kinetic mechanism at this level of detail into the fluid flow to model the combustion event is the most rigorous way of simulating combustion, the computational expense makes such an approach unfeasible since such simulations would take on the order of months to converge (Law, 2007). One way to ease the computational demand is to simplify the combustion kinetics by making use of reduced kinetics mechanisms. The reduced kinetic mechanism retains the most important features of the detailed mechanism but uses a smaller set of intermediates species and lumped species in the mechanism.



## 4.1 Reduced Mechanism

The reduced kinetic model used in this work was adapted from that described in Schrieber et al. (1994). The five step model is shown in Table 4.1 with the relevant kinetic parameters.

**Table 4.1:** Five step reduced mechanism for iso-octane (Schrieber et al., 1994)

| Reaction | | $H^0_{300}(kJ/mol)$ | A $(mol.m^3s)$ | E/R$(K)$ |
|---|---|---|---|---|
| 1 | $F \rightarrow X$ | 709.9 | $5.0 \times 10^8$ | 18050 |
| 2 | $X + 12.5O_2 \rightarrow P$ | $-4709.9$ | $7.0 \times 10^6$ | 7200 |
| $3^+$ | $F + 2O_2 \rightarrow I$ | $-53.9$ | $3.5 \times 10^9$ | 19500 |
| $3^-$ | $I \rightarrow F + 2O_2$ | 53.9 | $6.0 \times 10^{27}$ | 37500 |
| 4 | $I \rightarrow 2Y$ | $-60.0$ | $6.0 \times 10^7$ | 5000 |
| 5 | $Y + 0.5F + 11.5O_2 \rightarrow P$ | $-3913.1$ | $1.0 \times 10^9$ | 16500 |

The rate constant for the five step scheme is given by $k_i = A_i exp[-\frac{E}{RT}]$.

During the slow oxidation step, free radicals (OH, H, O, HO2, hydrocarbons) and other intermediate species (CO, H2, and partial oxidation and decomposition products of hydrocarbons, if present) are present (Kirk-Othmer, 2001). The temperature may or may not rise at this stage since the energy is essentially being stored in the free radicals. This behaviour is termed cool flame behaviour governed by low temperature kinetics. In the reduced model presented, when the first two reactions dominate, high temperature fuel oxidation occurs whereas the remaining reactions dominate on the low temperature pathway.

The simplified mechanism emulates the oxidation of $C_8H_{18}$ $(F)$ to yield intermediates $3C_2H_4 + CH_3 + H$ $(X)$ at high temperatures and the free radical $OC_7H_{13}O_2H + H_2O$ $(I)$ and $OH$ $(Y)$ at low temperatures (Griffiths, 1994). The lumped species, $X$, $I$, $Y$ are also termed pseudo species. The final products $(P)$ are approximated as $7CO_2 + 8H_2O$. The rate expressions that govern the reactions presented in Table 4.1 are given in Equations 4.1 to 4.6.

$$R_1 = k_1[F]\left(\frac{p}{p_o}\right)^{0.5} \tag{4.1}$$

$$R_2 = k_2[X][O_2][M] \tag{4.2}$$

$$R_{3^+} = k_{3^+}[F][O_2][M]\left(\frac{p}{p_o}\right)^{-2.2} C_{3^+} \tag{4.3}$$

$$R_{3^-} = k_{3^-}[I]\left(\frac{p}{p_o}\right)^{-3.5} \tag{4.4}$$

$$R_4 = k_4[I]C_4 \tag{4.5}$$

$$R_5 = k_5[O_2][Y] \tag{4.6}$$

An Arrhenius expression is assumed for the temperature dependence of the kinetic rate constant $(k_i)$ with the parameters given in Table 4.1, the term $\frac{p}{p_o}$ accounts for the changing pressure during the combustion event, the constants $C_{3^+}$ and $C_4$ are parametrised in terms of the octane number as follows $C_{3^+} = \left[\frac{110-ON}{10}\right]$, $C_4 = \left[\frac{110-ON}{10}\right]^{0.5}$, $M$ is the third body interaction and can be considered to be equivalent to $\frac{p}{RT}$ i.e. the total gas phase concentration.

## 4.2 Reaction Pathways

The reduced kinetics were modelled in a batch reactor to further explain the kinetic pathways and kinetic features of the mechanism. The results are presented in Figure 4.1. The system of equations that govern the batch reactor are explained in Chapter 5. The work done by Schrieber et al. (1994) assumes a constant heat capacity of 36 $\frac{J}{mol.K}$ for all species in the system and is used in this example.

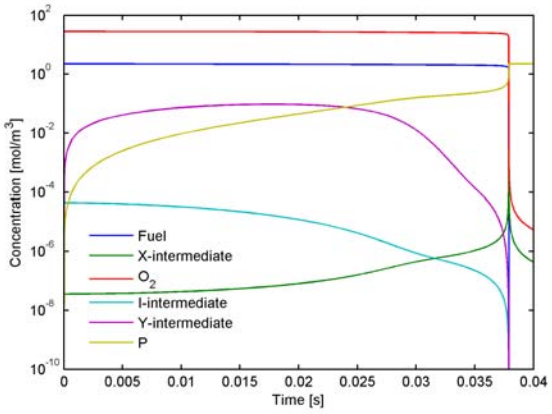


**(a)** Species concentrations

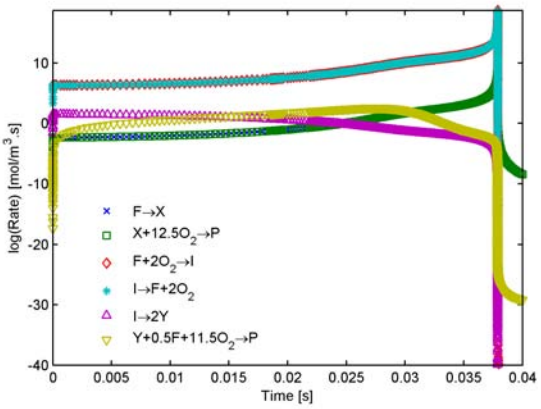


**(b)** Reaction rates

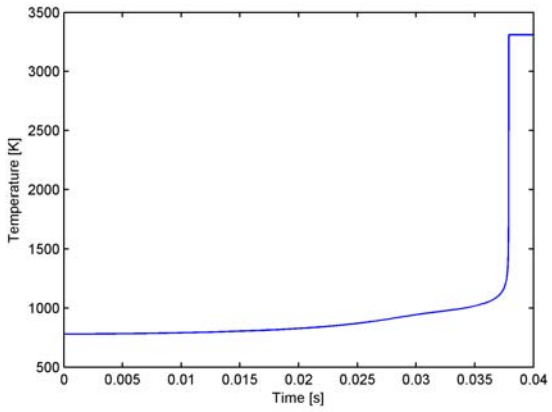


**(c)** Temperature profile

**Figure 4.1:** Iso-octane reduced kinetic scheme in a batch reactor. Molar composition: $iC_8H_{18}/O_2/N_2 = 1/12.5/47$. Initial conditions: $P_0 = 8.85$ bar; $T_0 = 780$ K, $V = 500 \times 10^{-6}$ m$^3$

There exist two reaction pathways during the combustion event.

**Pathway** 1 - Low temperature

With reference to Table 4.1, a closer look at the reaction rates (Figure 4.1b) and concentration profiles (Figure 4.1a) reveals that when the temperature is low, reactions 4 and 5 are dominant with reaction 4 having a slightly higher reaction rate than reaction 5. This results in the concentration of the low temperature intermediate ($Y$) increasing until a certain critical value. At the critical concentration, $Y$-intermediate is consumed along with some fuel and oxidant. Reaction 4 kinetic rate is driven by the concentration of the free radical ($I$). The net production of free radicals are produced by the competition between the formation reaction $3^+$ and the consumption reaction $3^-$. The net result is an increase in thermal energy and hence system temperature. When the temperature rises above a critical value, the high temperature reactions begin to dominate.

**Pathway** 2 - High temperature

With reference to Table 4.1, a closer look at the reaction rates (Figure 4.1b) and concentration profiles (Figure 4.1a) reveal that when the temperature is high, reactions 1 and 2 are dominant. The fuel is converted to the high temperature intermediate ($X$) by reaction 1 followed by the competing reaction 2 which converts the fuel to product ($P$). There is again an effective heat release that is much larger than that by the low temperature pathway. The temperature profile in the batch reactor (Figure 4.1c) shows the characteristics of two stage ignition as a result of the low and high temperature pathways.

The reduced model was simulated in a constant volume batch reactor for a range of initial temperatures and pressures while maintaining the same system geometry and volume. The resulting ignition time delay surface shown in Figure 4.2.



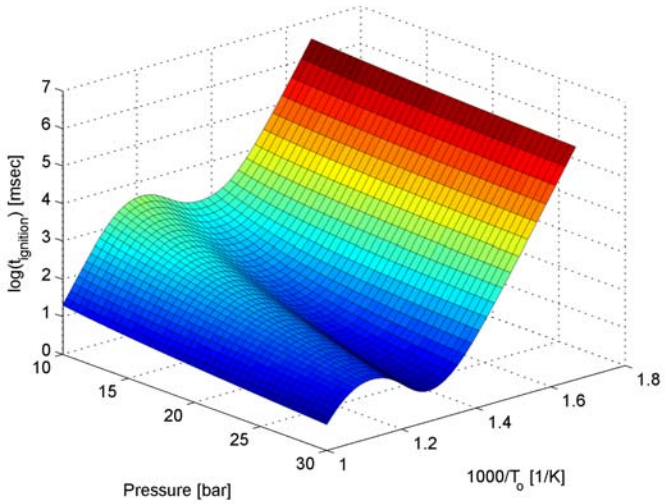


**Figure 4.2:** Ignition time delay at different compressed gas temperatures and pressures for iso-octane autoignition

Figure 4.2 shows that there is an increase in ignition delay time with an increase in initial temperature. This counter-intuitive phenomenon is called the negative temperature

coefficient region (NTC). The increase of ignition delay in the NTC region is associated with a lengthening of the duration of the second stage of reactions (Griffiths, 1994). The second stage of reactions causes the energy to be stored in the free radicals, a phenomenon termed cool flame behaviour (Kirk-Othmer, 2001).

## 4.3 Conclusion

A detailed chemical kinetic mechanism developed by Curran et al. (2002) to study the oxidation of iso-octane in a jet-stirred reactor, flow reactors, shock tubes and in a motored engine also exhibits phenomena of self ignition, cool flame, and NTC behaviour. As such, the reduced model maintains the essential features of the detailed chemical mechanism with far fewer elementary reactions and computational resources needed. Thus, the reduce model is deemed a suitable alternative to the full kinetic mechanism for incorporation into a chemical reactor network. The thermodynamic properties of the pseudo species will need to be investigated before the reduced model can be applied to flow reactors.

# Chapter 5

# Batch Reactor

The model equations for the batch reactor are derived from fundamentals such that it can easily be extend to other reactor types of interest to the study. For the current study, the energy balance for the batch reactor model is rigorously developed accounting for adiabatic expansion in the system during combustion. Furthermore, the experimental data available in Schrieber et al. (1994) was obtained from a batch reactor model and is used as a basis for kinetic validation and regression of the pseudo species heat capacities. Regressing is a novel approach in attempting to quantify the thermodynamic properties of pseudo species. The regression methodology is also explained in this section.



## 5.1 System Geometry

The batch reactor system geometry is shown in Figure 5.1.

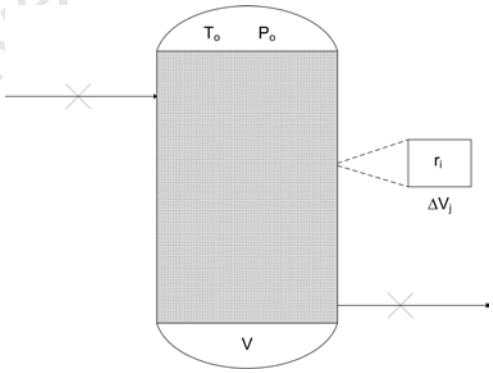


**Figure 5.1:** Batch reactor system

The systems initial conditions ($t_o$) are specified by initial temperature ($T_o$) and pressure ($P_o$). The volume ($V$ ) remains constant with time and there is no flow in to or out of the reaction vessel.

## 5.2 Mole Balance

The general mole balance in a chemically reacting system is given by Equation 5.1

$$F_{in,i} - F_{out,i} + G_i = \frac{\partial N_i}{\partial t} \tag{5.1}$$

where $F_{in,i}, F_{out,i}$ are the number of moles of the $i^{th}$ species entering or leaving the system $\left[\frac{mol}{s}\right]$, $G_i$ is the generation term $\left[\frac{mol}{s}\right]$, $N_i$ is the number of moles of the $i^{th}$ species in system $[mol]$. From Figure 5.1 the total generation within the control volume ($V$ ) is obtained by the summation of the rate of generation in each sub volume ($\triangle V_j$ ). The expression for $G_i$ is given by Equation 5.2.

$$G_i = \sum_{i=1}^{m} \triangle G_{i,j} = \sum_{i=1}^{m} r_{i,j} \triangle V_j = \int^{V} r_i dV \tag{5.2}$$

The generation term can now be substituted into Equation 5.1 to give the mole balance in its integral form given by Equation 5.3.

$$F_{in,i} - F_{out,i} + \int^{V} r_i dV = \frac{\partial N_i}{\partial t} \tag{5.3}$$

Applying the conditions of a well mixed batch reactor, yields an ordinary differential equation (ODE's) that governs the change in moles or concentration at any time within the reactor, Equations 5.4 - 5.5,

$$\frac{\partial N_i}{\partial t} = r_{net} V \tag{5.4}$$

$$\frac{\partial C_i}{\partial t} = r_{net} \tag{5.5}$$

where $r_{net}$ is the species net rate. The net rate is given by Equation 5.6.

$$r_{net,i} = \sum_{j=1}^{n_{rxn}} r_{i,j} \tag{5.6}$$

where $r_{i,j}$ is the reaction rate of the $i^{th}$ species in the $j^{th}$ reaction $\left[\frac{mol}{m^3 s}\right]$. The above equations are constructed for each species in the system including the intermediates. The species are related to each other through the net rate as explained in Chapter 4.

## 5.3 Energy Balance

Since the reactor is clearly non-isothermal, the energy balance must be solved simultaneously with the material balance. The energy balance equation for the system at any time

is given by Equation 5.7

$$\frac{\partial E_{sys}}{\partial t} = \sum_{i=1}^{n} F_{in,i} H_{in,i} - \sum_{i=1}^{n} F_{out,i} H_{out,i} + \dot{Q} - \dot{W}_{shaft} \tag{5.7}$$

where $H_i$ is the enthalpy of the $i^{th}$ species $\left[\frac{J}{mol}\right]$, $F_{in,i}, F_{out,i}$ is the flow of the $i^{th}$ species in or out of the reactor $\left[\frac{mol}{s}\right]$, $\dot{Q}$ is the external energy contribution $\left[\frac{J}{s}\right]$, $\dot{W}_{shaft}$ is the shaft work done on the system $\left[\frac{J}{s}\right]$. The summation is taken to account for the enthalpy flow of all the species entering the reactor.

It can be seen from Figure 5.1 that there is no inflow or outflow from the control volume ($F_{in,i} = F_{out,i} = 0$) and the reactor is assumed adiabatic with no shaft work ($\dot{Q} = \dot{W}_{shaft} = 0$). This yields the following ODE that governs the energy conservation in a constant volume batch reactor given by Equation 5.8.

$$\frac{\partial E_{sys}}{\partial t} = 0 \tag{5.8}$$

However, the energy change of the system ($E_{sys}$) consists of changes among the electrical, kinetic, internal and potential forms. The assumption is made that the system's energy is mainly internal energy since in chemically reacting systems the internal energy is far greater than the other contributions. The systems energy is given by Equation 5.9

$$E_{sys} = \sum_{i=1}^{n} E_i N_i = \sum_{i=1}^{n} U_i N_i = \sum_{i=1}^{n} N_i (H_i - P\hat{V}_i) = \sum_{i=1}^{n} N_i H_i - PV \tag{5.9}$$

where the summation of the species molar volume ($\hat{V}_i$) and number of moles ($N_i$) is the total volume ($V$) of the system. The pressure in the system is changing with time and needs to be taken into account. The change in systems energy with time in the batch reactor is therefore given by Equation 5.10.

$$\frac{\partial E_{sys}}{\partial t} = -\frac{\partial P}{\partial t} + \sum_{i=1}^{n} C_i \frac{\partial H_i}{\partial t} + \sum_{i=1}^{n} H_i \frac{\partial C_i}{\partial t} = 0 \tag{5.10}$$

Equation 5.10 explicitly contains the rate of change of pressure term ($\frac{\partial P}{\partial t}$) so it is easy to incorporate adiabatic expansion into the model.

In Equation 5.10 the change in concentration with time is described by the mole balance presented in Section 5.2. This relation can be directly substituted into Equation 5.10. Finally, heat capacity is defined such that Equation 5.11 can be use to convert the energy balance to the thermal form

$$\frac{\partial H_i}{\partial t} = Cp_i \frac{\partial T}{\partial t} \tag{5.11}$$

where $Cp_i$ is the heat capacity of the $i^{th}$ species $\left[\frac{J}{mol.K}\right]$. The pressure can be related to the temperature by the ideal gas law or an equation of state. The ideal gas law assumption is only valid when the pressure within the vessel does not exceed 15 bar. When the pressure does exceed this value, the appropriate equation of state should be used to relate the pressure to the temperature. When the ideal gas law is appropriate, the change in pressure as a function of time is given by Equation 5.12

$$\frac{\partial P}{\partial t} = TR_{gas}\sum_{i=1}^{n}\frac{\partial C_i}{\partial t} + \sum_{i=1}^{n}C_i R_{gas}\frac{\partial T}{\partial t} \tag{5.12}$$

where $R_{gas}$ is the ideal gas constant $\left[\frac{J}{mol.K}\right]$. When these relations are substituted into Equation 5.10, the balance that describes the rate of change in temperature with time inside the batch reactor is given by Equation 5.13.

$$\frac{\partial T}{\partial t} = \frac{-\sum_{i=1}^{n}H_i r_i + TR_{gas}\sum_{i=1}^{n}\frac{\partial C_i}{\partial t}}{-\sum_{i=1}^{n}C_i R_{gas} + \sum_{i=1}^{n}C_i Cp_i} \tag{5.13}$$

The batch reactor energy balance is now only a function of concentration and can easily be coupled to the mole balance equations for all the species. The work done by Schrieber et al. (1994) assumes a constant heat capacity of 36 $\frac{J}{mol.K}$ for all species in the system. This assumption was made since the experimental conditions contained large amounts of nitrogen and oxygen. This limits the models applicability to flow situations where the thermodynamic properties are needed.

## 5.4 Batch Reactor Algorithm

The algorithm used to simulated the reduced kinetic model in a batch reactor is shown in Figure 5.2.

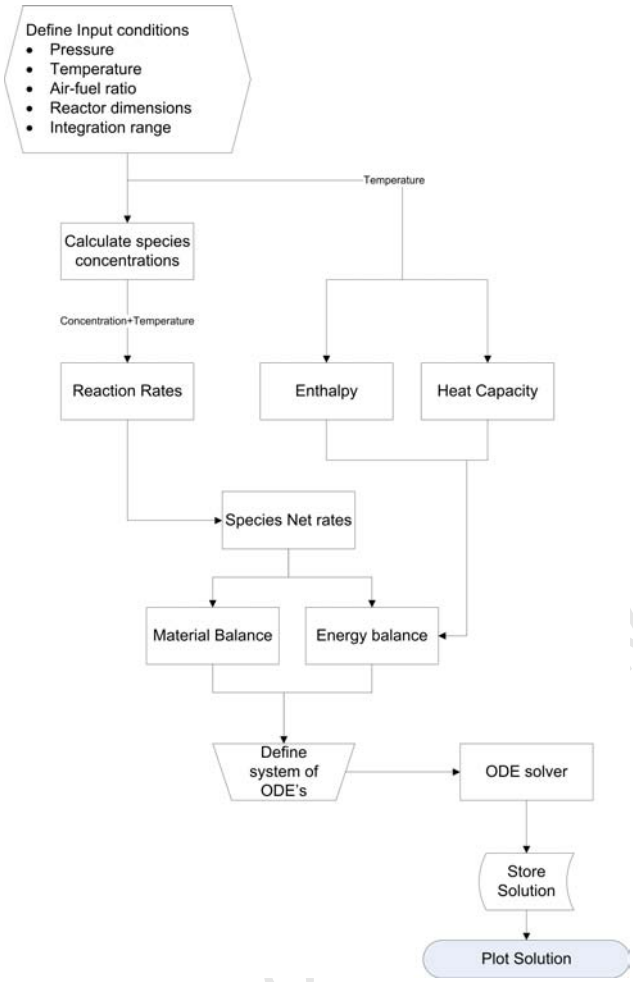


**Figure 5.2:** Batch reactor algorithm

The reaction rate is calculated using the kinetic expressions given in Chapter 4. The system of ODEs are solved using the second order (Wolfbrandt's formula) Rosenbrock formula. Very large gradient changes in the solution surface are common when solving combustion problems making application of numerically robust software particularly important (Shampine and Reichelt, 1997). It is appropriate to form a new Jacobian during the iteration procedure since the system of ODEs for combustion is a stiff set of equations thus the second order (Wolfbrandt's formula) Rosenbrock formula is the suitable choice of solver.

## 5.5 Regression of Heat Capacities

For the purpose of simulating a chemical reactor network, the thermal characteristics of all species are required. This poses a challenge when using a reduced kinetic scheme since the thermodynamic properties of the pseudo species are not known. In this section, the heat of formation and heat capacity of these lumped species are regressed against experimental data. The model originally proposed Griffiths (1994) by was validated with

experimental data by Schrieber et al. (1994) and is used as the basis for the regression of the species enthalpies. The properties of the well-defined species (fuel, nitrogen and oxygen) are already known and can be obtained from various sources.

### 5.5.1 Proposed Model

The enthalpy of each pseudo species in the system is assumed to follow the same relation as normal species (see Equation 5.14).

$$H(T) = H^0_{300K} + \int_{T_{ref}}^{T} Cp\, dT \tag{5.14}$$

where $H^0_{300K}$ is the standard heat of formation and $Cp$ is the heat capacity of the species $\left[\frac{J}{mol}\right]$. This implies there exists $N \times 2$ parameters that need to be optimised where $N$ is 4, the number of pseudo species. For the pseudo species that are low in concentration ($X$, $I$ and $Y$), the heat of formation can be estimated using applying Hess's Law to the heats of reaction given in Table 4.1. This reduces the total number of unknown parameters by 3 to 5. The parameters that need to be regressed are, $H^0_{300K,P}$, $Cp_X$, $Cp_I$, $Cp_Y$, $Cp_P$.

The regression model assumes that the heat capacity is a temperature constant. The species concentration and the systems temperature profile is used to obtain the mean squared error (MSE). The objective function to be minimised is the MSE between the current enthalpy model and the data provided by Schrieber et al. (1994). The MSE is given by Equation 5.15

$$MSE_{cp} = \sum_{j=1}^{n}\sum_{i=1}^{t_{end}} \left[\frac{C^{model}_{i,j} - C^{exp}_{i,j}}{C^{exp}_{i,j} + f}\right]^2 \tag{5.15}$$

where $C^{exp}_{i,j}$ is the concentration of the $j^{th}$ species at the $i^{th}$ time predicted by Schrieber et al. (1994) $\left[\frac{mol}{m^3}\right]$, $f$ a dimensionless scale factor, $C^{model}_{i,j}$ is the concentration of the $j^{th}$ species at the $i^{th}$ time predicted by current enthalpy model $\left[\frac{mol}{m^3}\right]$. The MSE needs to be weighted as to compensate for order of magnitude problems with the pseudo-species, thus a scale factor is introduced.

### 5.5.2 Algorithm

The algorithm used to optimise the parameters ($H^0_{300K,P}$, $Cp_X$, $Cp_I$, $Cp_Y$, $Cp_P$) are shown in Figure 5.3.


**Figure 5.3:** Regression algorithm

The batch reactor is solved using the parameters given in Schrieber et al. (1994) and the proposed parameters separately. The initial guess for the parameter values are explained in Section 5.5.3. The MSE (Equation 5.15 ) is calculated using both sets of data. If the residual does not satisfy a given tolerance, a line search algorithm is used to obtain the next set of input parameters that minimise the MSE. The system of ODEs for combustion are solved using the second order Rosenbrock formula.

### 5.5.3 Initial Parameter Selection

Since the optimisation over a space may in principle contain many local minima, a good initial guess for the parameters is essential. The MSE was sampled over a range to obtain the effect of the different parameters on the objective function. This is termed the boot strap method. The parameter range was chosen to be a arbitrary heat capacity range of $[100, 1000]$ $\frac{J}{mol.K}$ and $[-3.5, -4.5] \times 10^6$ $\frac{J}{mol}$ for the product heat of formation. The resulting surface for the MSE at various planes in the $5D$ space is shown in Figure 5.4 and 5.5.

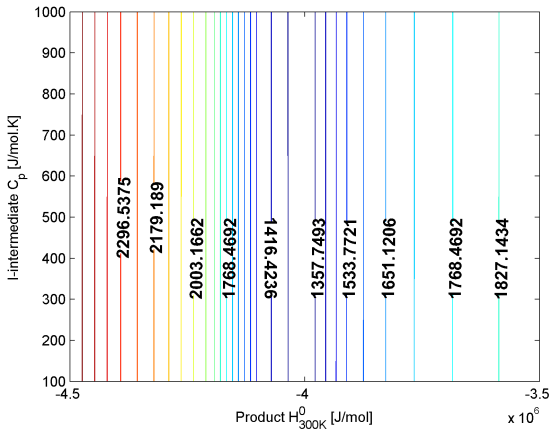


**(a)** $Cp_j = 100\frac{J}{mol.K}$, $j \neq I$

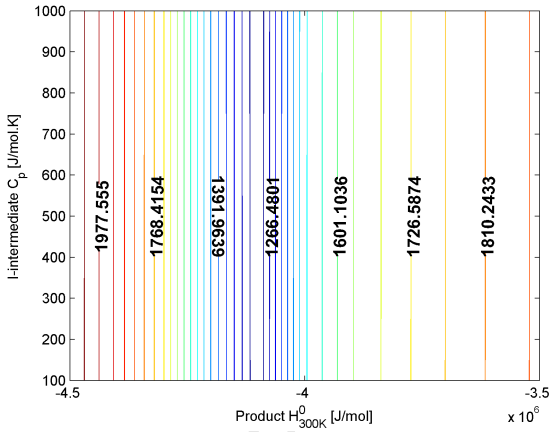


**(b)** $Cp_j = 500\frac{J}{mol.K}$, $j \neq I$

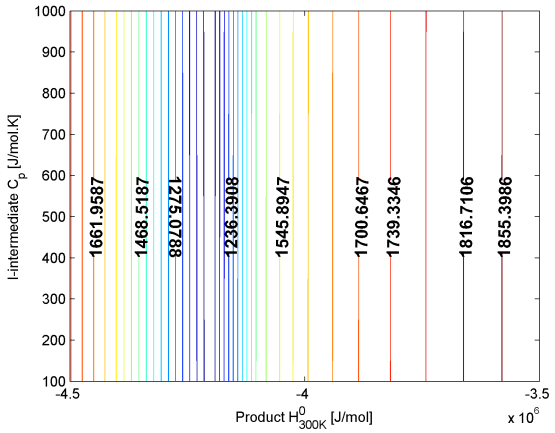


**(c)** $Cp_j = 1000\frac{J}{mol.K}$, $j \neq I$

**Figure 5.4:** $Cp_I|H^0_{product}$ plane with varying intermediate heat capacities. The contour indicates the magnitude of the MSE

Figure 5.4 shows the MSE in $Cp_I|H^0_{product}$ plane keeping the other parameters heat capacities fixed at values in the range $[100, 1000]$ $\frac{J}{mol.K}$. Figure 5.4 shows that the MSE in $Cp_I|H^0_{product}$ plane the is not affected by the heat capacity of the $I$ intermediate but

shifts with respect to other species heat capacities. Similar trends are noticed for the $X$ intermediates heat capacity in the $Cp_X|H^0_{product}$ plane. This is most likely due to the small concentrations of these species in the system. On the other hand, much greater sensitivity is observed in the $Cp_Y|H^0_{product}$ plane shown in Figure 5.5.

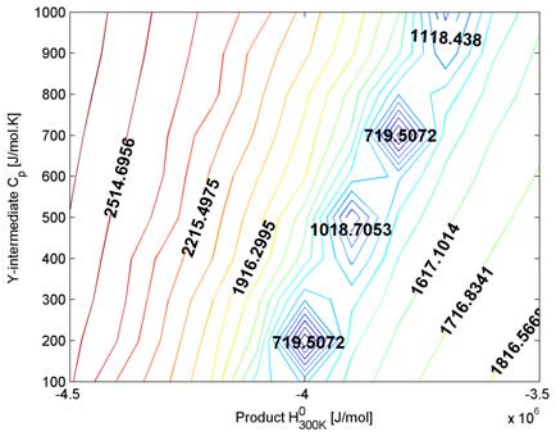


**(a)** $Cp_j = 100\frac{J}{mol.K}$, $j \neq Y$

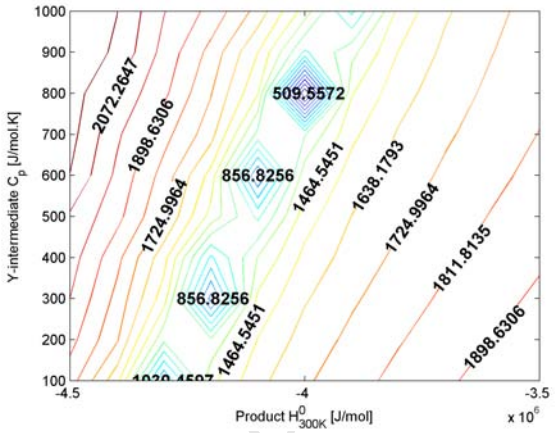


**(b)** $Cp_j = 500\frac{J}{mol.K}$, $j \neq Y$

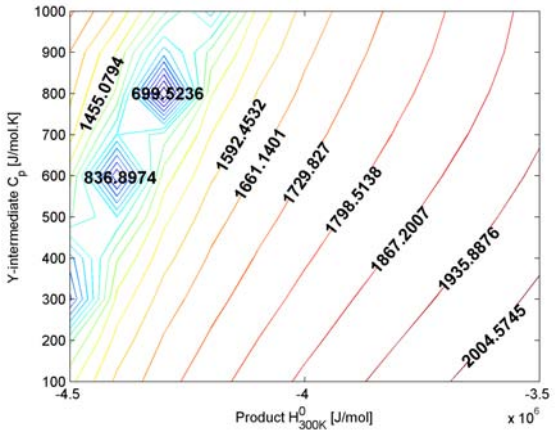


**(c)** $Cp_j = 1000\frac{J}{mol.K}$, $j \neq Y$

**Figure 5.5:** $Cp_Y|H^0_{product}$ plane with varying intermediate heat capacities. The contour indicates the magnitude of the MSE

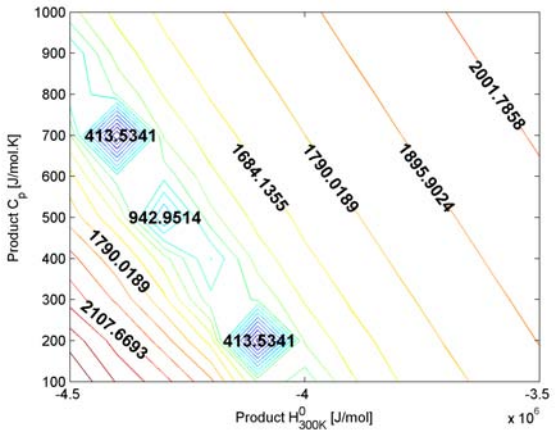


**(a)** $Cp_j = 100\frac{J}{mol.K}$, $j \neq P$

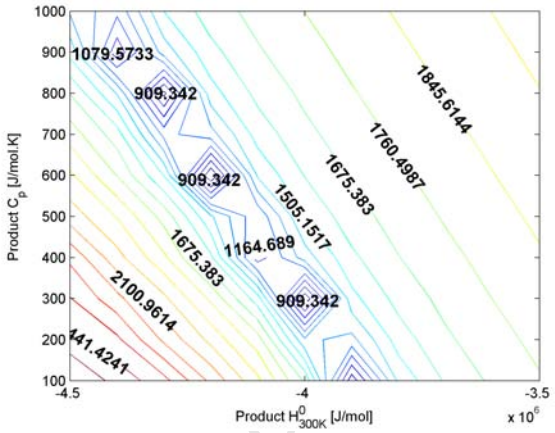


**(b)** $Cp_j = 500\frac{J}{mol.K}$, $j \neq P$

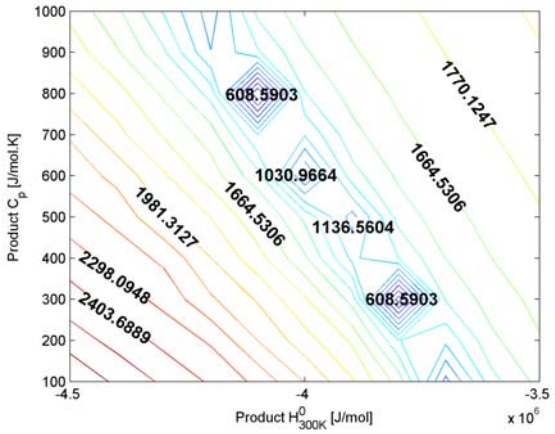


**(c)** $Cp_j = 1000\frac{J}{mol.K}$, $j \neq P$

**Figure 5.6:** $Cp_P|H^0_{product}$ plane with varying intermediate heat capacities. The contour indicates the magnitude of the MSE

Figure 5.5 shows that there exist multiple local minima in a banded configuration. Similar trends are observed in the $Cp_P|H^0_{product}$ (Figure 5.6). This would make obtaining the global minimum searches extremely difficult since most search algorithms, i.e. SIM-

PLEX, Levenberg-Marquardt, Conjugate gradient, would fall into these local minima. It can be seen from Figure 5.5 that when the heat capacity of intermediate species is increased, the band of minima is shifted indicating that the MSE does indeed depend on the heat capacities of the intermediate species.

### 5.5.4 Optimisation

A Line Search is a method of finding a minimum of a function along a given line. This is done by first calculating the search direction $s$ in which to move along. The second step is to calculate how far along the line to move. This is given by the step length $\lambda$. This step is taken by each variable $i$ in the equation. Mathematically this is given in Equation 5.16.

$$x_i^{new} = x_i^{old} + \lambda s_i \tag{5.16}$$

The search direction is a vector with the dimensions $N \times 1$ where, for the present application, $N$ is the number of variables, $H^0_{300K,P}$, $Cp_X$, $Cp_I$, $Cp_Y$, $Cp_P$.

Due to the dimensions of the MSE, the evaluation of the gradient during the optimisation procedure is the factor that has the most computational demand. The optimisation algorithm used is a combination of the non gradient based SIMPLEX method and Levenberg-Marquardt method. The simplex method is initially used to obtain the region of the minimum with further refinement being done by the line search method.

The parameter values that give the lowest Mean Squared Error (MSE) between the experimental data by Schrieber et al. (1994) and the model results using the regressed parameters are indicated in Table 5.1 with the MSE given in Figure 5.7.

| Parameter | $H^0_{300K}$ (J/mol) | $Cp$ (J/mol.K) |
|---|---|---|
| X-intermediate | 501150 | 617 |
| I-intermediate | −154850 | 404 |
| Y-intermediate | −107425 | 417 |
| Product | $-4.28 \times 10^6$ | 415 |

**Table 5.1:** Regressed parameter values

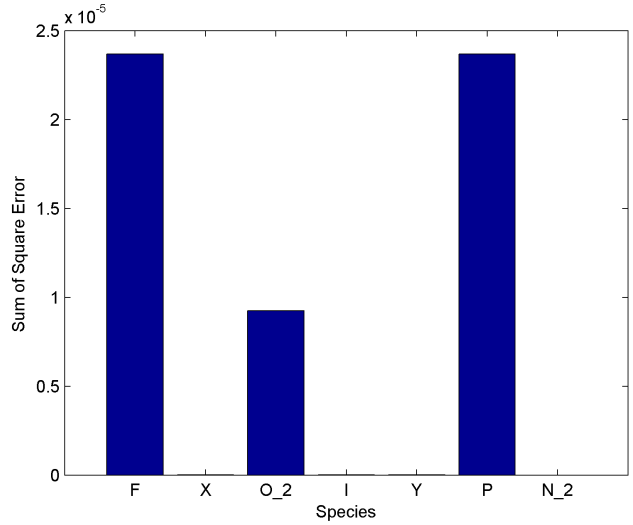


**(a)** Sum of Square Errors

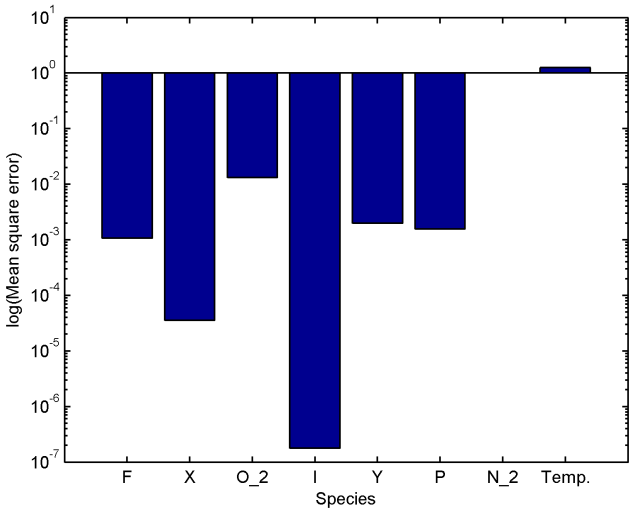


**(b)** Mean Squared Error

**Figure 5.7:** Error for individual species and temperature profile

The regression resulted in a reasonably low sum of square errors and MSE as shown in Figure 5.7 which indicates that the regressed parameters give a good fit to the experimental data by Schrieber et al. (1994). Due to the good fits achieved, the parameters given in Table 5.1 is used to predict the enthalpy of the lumped species in the ideal compartment reactor models.

## 5.6 Conclusion

All the species in the system are now fully defined in terms of thermodynamic properties. The plug flow reactor and the continuous stirred tank reactor models are identified as suitable idealised compartments, since each represents the opposite extremum in terms

of the hydrodynamics. Before the network can be proposed, the model development of these idealised sub-models must be fully investigated.

# Chapter 6

# Idealised Compartments

The plug flow reactor and the continuous stirred tank reactor models were identified as suitable idealised compartments. The batch reactor model presented in the previous section was used for kinetic validation and regression of the pseudo species heat capacities. The optimised pseudo species heat capacities is used in the enthalpy calculation in the idealised compartments. Including the energy balance for each idealised compartment at this development stage allows the network to be a more predictive model as apposed to earlier works done by Falcitelli et al. (2002b) who only considered integration of the material balance.



## 6.1 Plug Flow Reactor

The ideal PFR has different hydrodynamic characteristics from the other reactor types presented in this study. n an ideal plug flow reactor (PFR), the fluid flows in discrete plugs with no axial dispersion effects. In the current study, the model equations for the PFR are presented here taking into consideration the effect of combustion kinetics on the fluid velocity.

### 6.1.1 System Geometry

The geometry for the PFR system investigated in this study is shown in Figure 6.1.

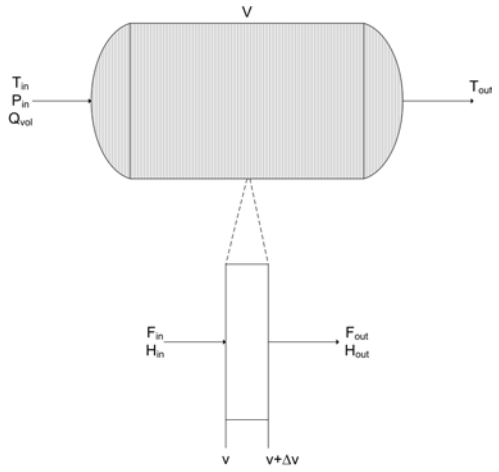


**Figure 6.1:** Plug flow reactor system

The temperature, pressure and volumetric flow rate of the feed is specified as inlet conditions to the reactor. For a PFR operating at steady state, the initial conditions are specified in the spatial domain $V_o$. The species mole balance and system energy balance is done on the differential element shown in Figure 6.1.

### 6.1.2 Mole Balance

The general unsteady state PFR mole balance is given by Equation 6.1

$$\frac{\partial C_i}{\partial t} = -\frac{\partial F_i}{\partial V} + r_{net,i} \tag{6.1}$$

where $r_{net,i}$ is the net rate of the $i^{th}$ species given by the reduced scheme $\left[\frac{mol}{m^3 s}\right]$. The flow rate can be related to the concentration through the velocity ($V_z$), PFR cross sectional area ($A$) and dispersion of the species ($D_{coeff}$). The relation is given by Equation 6.2.

$$F_i = C_i A V_z - A D_{coeff,i} \frac{\partial C_i}{\partial V} \tag{6.2}$$

An ideal PFR has no axial dispersion effects so the second term in Equation 6.2 can be neglected. To obtain $\frac{\partial F_i}{\partial V}$, the cross sectional area of the PFR remains constant but the velocity changes. The velocity can be related to the pressure by application of the equation of state (ideal gas law assumed since the pressure is below 15 bar), Equation 6.3,

$$V_z = \frac{MassFlow}{\rho A} = \frac{C_{total}\overline{MW}}{\left[\frac{P\overline{MW}}{R_{gas}T}\right] A} \tag{6.3}$$

where $R_{gas}$ is the kinetic gas constant $\left[\frac{J}{mol.K}\right]$, $P$ is the pressure in the reactor $[Pa]$, $A$

is the cross sectional area of the reactor $[m^2]$, $\overline{MW}$ is the average molecular mass of the mixture $\left[\frac{g}{mol}\right]$. The molecular masses of the pseudo species are not known so the molecular weight of the mixture is assumed to be that of nitrogen since the reacting mixture consists mostly of nitrogen.

The underlying assumption is that the pressure within each differential volume remains constant. The mole balance in terms of concentration gradients is given by Equation 6.4.

$$\frac{\partial C_i}{\partial t} = -AV_z\frac{\partial C_i}{\partial V} + r_{net,i} \tag{6.4}$$

When the system reaches steady state, the time derivatives are zero and the steady state mole balance is given by Equation 6.5.

$$\frac{\partial C_i}{\partial V} = \frac{r_{net,i}}{AV_z} \tag{6.5}$$

The net rate of the species has to be used in the mole balance, Equation 6.5. Equation 6.5 differs from the conventional PFR model since the velocity ($V_z$) is related to the combustion kinetics through the equation of state. Thus, thermal feedback ($T$) from the kinetics is inherently incorporated into the velocity. The above equations are constructed for each species in the system including the intermediates. The species are related to each other through the kinetic source term as explained in Chapter 4.

### 6.1.3 Energy Balance

The reactor is non isothermal, making it necessary to solve the energy balance to predict the system temperature. When the PFR is assumed to be adiabatic, the steady state energy balance is given by Equation 6.6.

$$-\frac{\partial\sum_{i=1}^{n}F_iH_i}{\partial V} = 0 \tag{6.6}$$

Applying the chain rule to the right hand side of the Equation 6.6, Equation 6.7 is obtained.

$$-\sum_{i=1}^{n}H_i\frac{\partial F_i}{\partial V} - \sum_{i=1}^{n}F_i\frac{\partial H_i}{\partial V} = 0 \tag{6.7}$$

Equation 5.11 is used to convert the energy balance to the thermal form. The steady state mole balance is substituted for the expression $\frac{\partial F_i}{\partial V}$. This yields the steady state ODE that describes the temperature change along the length of the PFR, Equation 6.8.

$$\frac{\partial T}{\partial V} = \frac{-\sum_{i=1}^{n} H_i r_{net,i}}{AV_z \sum_{i=1}^{n} C_i Cp_i} \tag{6.8}$$

The heat capacities and enthalpies of the species in Equation 6.8 are calculated using the optimised parameters in Table 5.1. Equation 6.8 differs from the conventional PFR model since the velocity ($V_z$) is related to the combustion kinetics through the equation of state. The PFR energy balance is now only a function of concentration and can easily be coupled to the mole balance equations for all the species. The mole balance equations are solved together with the energy balance equation. The expressions for $r_{net}$ for each species was presented in Chapter 4.

### 6.1.4 Simulation algorithms

The algorithm to simulated the reduced kinetic model in a PFR is shown in Figure 6.2.

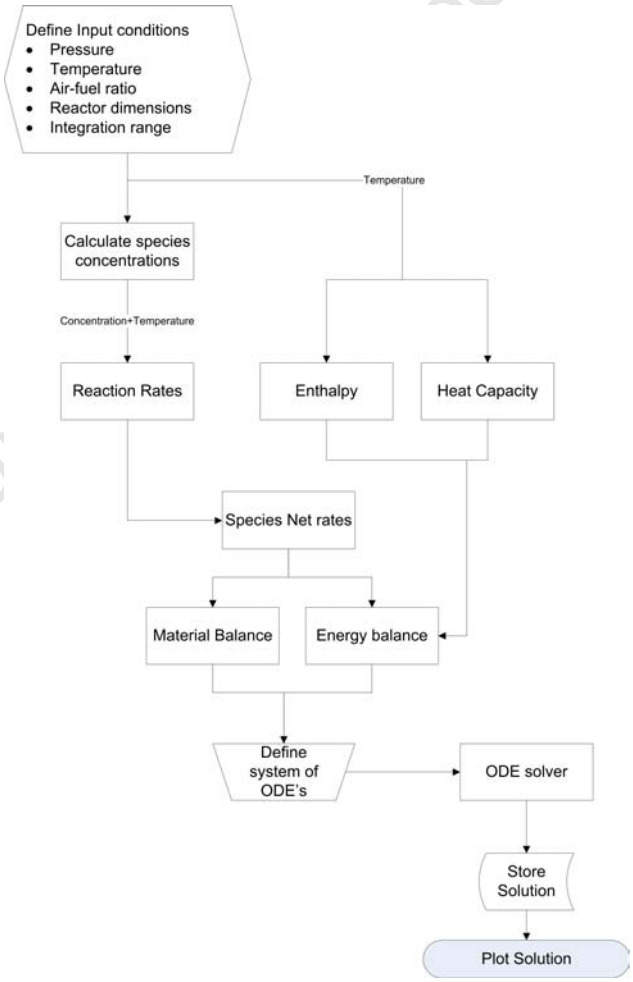


**Figure 6.2:** Plug flow reactor algorithm

The calculation of the reaction rates is done using the kinetic expressions given in Chapter 4. The second order Rosenbrock formula is used in the ODE solver block. The algorithm varies from the batch reactor algorithm since the heat capacities and enthalpies of the species are now calculated using the optimised parameters in Table 5.1.

## 6.2 Continuous Stirred Tank Reactor

The ideal continuous stirred tank reactor (CSTR) represents the opposite extrema to the PFR in terms of the hydrodynamics. The ideal CSTR assumes that fluid in the system is completely mixed. In the current study, the model equations for the CSTR are presented here taking into consideration the effect of combustion kinetics on the system pressure. The standard CSTR model is then extended to the Tanks-In-Series model since it provides added flexibility when designing the network of reactors.

### 6.2.1 System Geometry

The CSTR system geometry is shown in Figure 6.3.

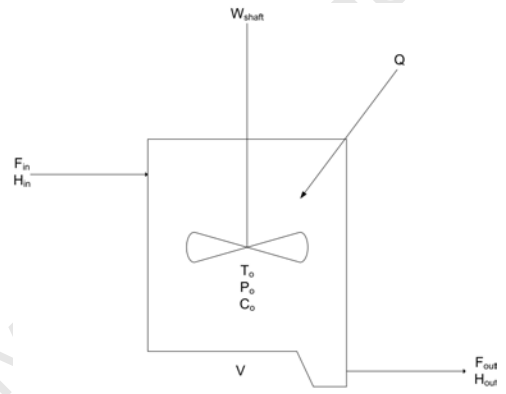


**Figure 6.3:** Continuous stirred tank reactor system

The system's initial conditions ($t_o$) are specified by initial temperature ($T_o$) and pressure ($P_o$)(scalar) fields. The reaction volume ($V$ ) is obviously a time constant (non-piston systems). The volumetric flow rate is also specified as inlet condition to the reactor. The vessel is considered to be well mixed.

### 6.2.2 Mole Balance

The mole balance equation for a CSTR is given by Equation 6.9

$$F_{in,i} - F_{out,i} + \int^{v} r_{net,i} dV = \frac{dN_i}{dt} \tag{6.9}$$

where $F_{in,i}, F_{out,i}$ are the flow rates of the $i^{th}$ species entering or leaving of the system $\left[\frac{mol}{s}\right]$, $\int^v r_{net,i}dV$ is the generation term $\left[\frac{mol}{s}\right]$, $N_i$ is the number of moles of the $i^{th}$ species in system$[mol]$. In a CSTR, the reacting mixture is assumed to be completely mixed with no spatial variation in the reaction rate thus the generation term can be simplified, Equation 6.10.

$$\int^v r_{net,i}dV = r_{net,i}V \tag{6.10}$$

Equation 6.10 is substituted into Equation 6.9 to yield the mole balance for a steady state CSTR, Equation 6.11

$$\frac{dC_i}{dt} = r_{net,i} + (C_{in,i} - C_i)\frac{Q_{vol}}{V} \tag{6.11}$$

where $r_{net,i}$ is the net rate of the $i^{th}$ species $\left[\frac{mol}{m^3 s}\right]$, $C_{i,in}$ is the concentration of the $i^{th}$ species entering the reactor $\left[\frac{mol}{m^3}\right]$, $Q_{vol}$ is the volumetric flow rate into the reactor $\left[\frac{m^3}{s}\right]$, $V$ is the volume of the reactor $[m^3]$. The above equations are constructed for each species in the system including the intermediates. The species are related to each other through the kinetic source term as explained in Chapter 4.

### 6.2.3 Energy Balance

The reactor is non isothermal so the energy balance is considered. The energy balance for a CSTR is given by Equation 6.12

$$\dot{Q} + \dot{W}_s + \sum_{i=1}^{n} F_{in,i}H_{in,i} - \sum_{i=1}^{n} F_{out,i}H_{out,i} = \frac{\partial \hat{E}_{sys}}{\partial t} \tag{6.12}$$

where $H_i$ is the enthalpy of the $i^{th}$ species $\left[\frac{J}{mol}\right]$, $F_{in,i}, F_{out,i}$ is the flow of the $i^{th}$ species in or out of the reactor $\left[\frac{mol}{s}\right]$, $\dot{Q}$ is the external energy contribution $\left[\frac{J}{s}\right]$, $\dot{W}_{shaft}$ is the shaft work done on the system $\left[\frac{J}{s}\right]$. The vessel is considered to be adiabatic ($\dot{Q} = 0$) with no shaft work ($\dot{W}_s = 0$) being done on the system. Substituting the relation for the systems energy change with time (Section 5.3) into the Equation 6.12 yields Equation 6.13.

$$\sum_{i=1}^{n} F_{in,i}H_{in,i} - \sum_{i=1}^{n} F_{out,i}H_{out,i} = \sum_{i=1}^{n} N_i\frac{\partial H_i}{\partial t} + \sum_{i=1}^{n} H_i\frac{\partial N_i}{\partial t} - V\frac{\partial P}{\partial t} \tag{6.13}$$

Assuming an ideal gas relation for the pressure gradient and substitution of the mole balance (Equation 6.11) into Equation 6.13 yields Equation 6.14

$$V\frac{\partial P}{\partial t} = VTR_{gas}\sum_{i=1}^{n} r_{net,i} + Q_{vol}TR_{gas}\left[\sum_{i=1}^{n} C_{in,i} - \sum_{i=1}^{n} C_{out,i}\right] - V\sum_{i=1}^{n} C_{out,i}R_{gas}\frac{\partial T}{\partial t} \tag{6.14}$$

where $R_{gas}$ is the kinetic gas constant $\left[\frac{J}{mol.K}\right]$, $T$ is the temperature in the reactor $[K]$. Equation 6.14 inherently captures the change in system pressure due to the effects of combustion. The thermodynamic relation between the temperature gradient and the species heat capacity is substituted into the Equation 6.13 along with the pressure relation (Equation 6.14) and mole balance (Equation 6.11) to yield Equation 6.15

$$\frac{dT}{dt} = \frac{\sum_{i=1}^{n} F_{i,0} Cp_i (T - T_0) - \sum_{i=1}^{n} H_i r_{net,i} V + VTR_{gas} \sum_{i=1}^{n} r_{net,i} - Q_{vol} TR_{gas} (\sum_{i=1}^{n} C_{i0} - \sum_{i=1}^{n} C_i)}{\sum_{i=1}^{n} \frac{C_i}{V} Cp_i + V \sum_{i=1}^{n} C_i R_{gas}} \tag{6.15}$$

where $F_{i,in}$ is the flow rate of the $i^{th}$ species into the reactor $\left[\frac{mol}{s}\right]$, $T_{in}$ is the temperature of the fluid entering the reactor $[K]$. Equation 6.15 varies from the conventional CSTR energy balance since it takes into consideration the pressure changes in the reactor by coupling it to the ideal gas equation. This allows the pressure correction terms in the kinetic scheme to be accounted for correctly. The CSTR energy balance is a function of concentration and can easily be coupled to the mole balance equations for all the species. The mole balance equations are solved together with the energy balance equation by using the expressions for $r_{net}$ presented in Chapter 4.

### 6.2.4 Tanks-In-Series

The mole balance and energy balance for the ideal CSTR can now be extended to two or more tanks connected in series. A schematic is shown in Figure 6.4.

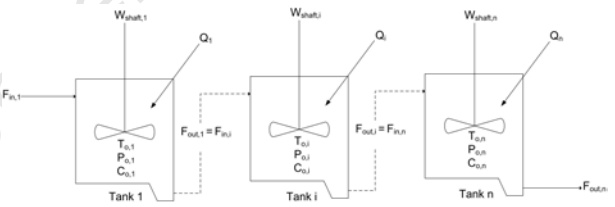


**Figure 6.4:** Tanks-In-Series system

The exit from the Tank 1 is the inlet to Tank $i$. The resulting system of ODEs that govern this relationship is given by Equation 6.16 and 6.17

$$\frac{dC_{i,j}}{dt} = r_{net,i,j} + (C_{i,j-1} - C_{i,j}) \frac{Q_j}{V_j} \tag{6.16}$$

$$\frac{dT_j}{dt} = \frac{\sum_{i=1}^{n} F_{i,j-1} Cp_{i,j}(T_j - T_{j-1}) - \sum_{i=1}^{n} H_{i,j} r_{net,i,j} V_j + V_j T_j R_{gas} \sum_{i=1}^{n} r_{net,i,j} - Q_j T_j R_{gas}(\sum_{i=1}^{n} C_{i,j-1} - \sum_{i=1}^{n} C_{i,j})}{\sum_{i=1}^{n} \frac{C_{i,j}}{V_j} Cp_{i,j} + V_j \sum_{i=1}^{n} C_{i,j} R_{gas}} \tag{6.17}$$

where $r_{net,i,j}$ is the net rate of species $i$ in tank $j$ $\left[\frac{mol}{m^3 s}\right]$, subscript $j$ represents the current tank, subscript $j-1$ represents the previous tank. The TIS model equations simplifies the coding procedure needed to simulate $n$ tanks in series.

### 6.2.5 Simulation Algorithm

The algorithm simulate a CSTR is shown in Figure 6.5.

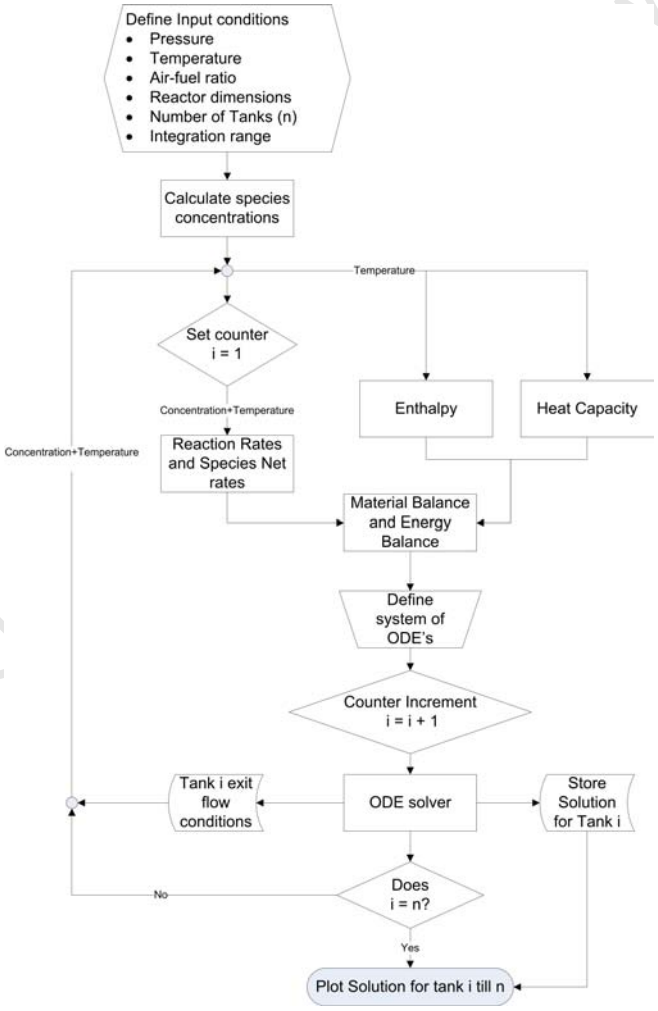


**Figure 6.5:** Continuous stirred tank reactor algorithm

The calculation of the reaction rates is done using the kinetic expressions given in Chapter 4. The second order Rosenbrock formula is used in the ODE solver block. The

algorithm is the same as the PFR algorithm which uses the optimised parameters in Table 5.1. When more than 1 Tank is selected, the output from Tank 1 is used as the inlet to Tank 2 with the solution of Tank 1 being stored for evaluation purposes.

## 6.3 Conclusion

The two opposite extrema in terms of the hydrodynamics, PFR and CSTR models, have now been developed. In principle, it is possible that a network of these reactors will be sufficient to model any imperfectly mixed system. These sub-models can now be applied to a chemical reactor network (CRN).

# Chapter 7

# Computational Fluid Dynamics

Compartmentalisation methodology proposes a chemical reactor network to serve as a surrogate for the computationally expensive CFD simulations. In order to develop the CRN, detailed flow field information obtained from CFD simulations is used as a basis and thus described in this section.

Computational Fluid Dynamics (CFD) simulations are required to obtain velocity vector, composition and temperature scalar fields within the domain. These vector fields give an insight into the hydrodynamics of the real system. The CFD simulations were performed using the commercial software package ANSYS CFX 11.0. The ANSYS CFX software was used to solves the Navier Stokes (NS) equations in the well established form presented in Chapter 2 and Bird et al. (2002). The geometry, boundary conditions and particular models adopted for turbulence and combustion chemistry in the ANSYS package are described in this section. For the current study, two geometries are proposed and simulated after which it was investigated whether compartmentalisation using the sub-models presented in the previous chapters is feasible.



## 7.1 Geometry

As mentioned, two geometries were investigated in this study, a simplified tubular reactor and an industrial furnace. The surface and volume meshes were generated using the advancing front algorithm in the ANSYS CFX-meshing tool. The mesh consists of automatically generated tetrahedral elements, with a finer face spacing being enforced on the inlet boundary. This is done so that the flame propagation can be accurately captured since the thermal and flow gradients are highest in this region. The CFD simulations were performed over a wide range of inlet velocities to ascertain the effect on the proposed network.

### 7.1.1 Double Inlet Reactor

The geometry of the double inlet reactor and the corresponding parameters are shown in Figure 7.1 and Table 7.1 respectively.

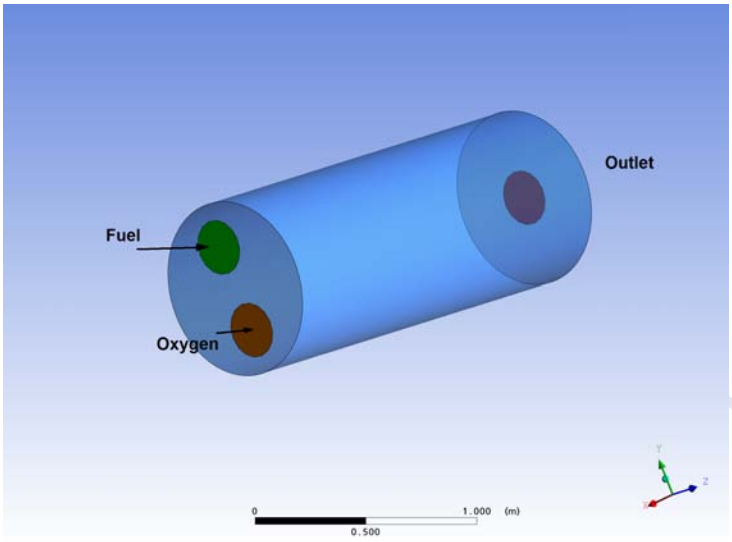


**Figure 7.1:** Reactor schematic. The fuel and oxygen inlet is indicated in green brown respectively. The outlet is indicated in red

**Table 7.1:** Double inlet reactor parameters and boundary conditions

| Parameter | Value |
|---|---|
| Inlet/Outlet radius, Shell Radius, Length | 0.125 m, 0.4 m, 2 m |
| Inlet - Temperature, Velocity Range | 780 K, 1-100 m/s |
| Fuel Inlet Mass Composition (Fuel, Oxygen, Inert) | 1, 0, 0 |
| Oxygen Inlet Mass Composition (Fuel, Oxygen, Inert) | 0, 0.232, 0.768 |

The double inlet reactor is fed with a stream of pure iso-octane and pure air at the conditions described in Table 7.1. A no-slip boundary condition is enforced on the walls of the reactor in addition to imposing the adiabatic mode of operation. The turbulent length scale at the inlet boundary is auto computed within the simulation. A zero pressure gradient boundary condition is set at the outlet of the reactor since it is essentially a free boundary condition.

The surface and volume mesh was generated using the advancing front algorithm (Zienkiewicz and Taylor, 2000) where the mesh is automatically generated to consist of tetrahedral elements.

In this study, the double inlet reactor was simulated at various inlet velocities. The velocity range for the double inlet reactor is shown in Table 7.1.

The initial simulations showed that at a mesh resolution of 3.5 million cells and higher took $\sim$ 2 CPU hours to complete which is a relatively low computational demand for a

CFD simulation. The solution does not vary with a mesh resolution above 3.5 million cells. Thus, it was deemed unnecessary to ascertain a lower mesh resolution at which point the solution becomes mesh independent. The mesh resolution of 3.5 million cells was used to test the influence of the inlet velocity on the reactor network.

### 7.1.2 Furnace

The furnace presented by Falcitelli et al. (2002b) is adopted for the more advanced geometry since Falcitelli et al. (2002b) showed that a CRN can be synthesised from such a geometry. In their work, Falcitelli et al. (2002b) investigated methane combustion whereas this study focuses on iso-octane combustion. The furnace is fed with a stoichiometric mixture of iso-octane and air at the conditions described in Table 7.2. The geometry of the furnace is shown in Figure 7.2.

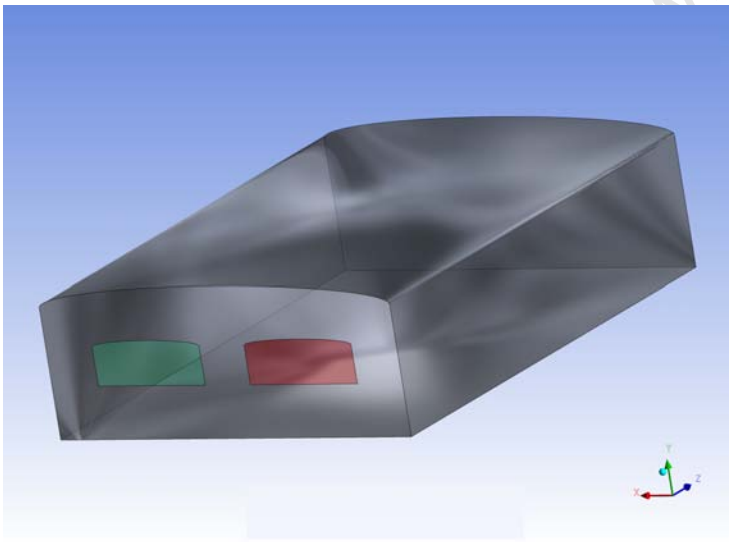

**Figure 7.2:** Furnace schematic (Falcitelli et al., 2002b). The inlet is indicated in green and the exit is indicated in red

**Table 7.2:** Furnace parameters and boundary conditions

| Parameter | Value |
|---|---|
| L, W, H | 8.4 m, 5.9 m, 2.3 m |
| Inlet temperature | 780 K |
| Inlet velocity | 26 - 350 m/s |
| Inlet mass fraction (Fuel, Oxygen, Inert) | 0.0623, 0.2185, 0.7192 |

The same boundary conditions are used for the furnace simulation and the double inlet reactor geometry. The furnace was also simulated at various inlet velocities. Initial simulations showed that for a grid size of 3.5 million elements, it took $\sim$ 25 CPU hours to complete due to the complex flow patterns within the domain. In order to minimised

the computational demand, the point at which the furnace simulation becomes mesh independent has to be calculated. It is assumed for a grid size of 3.5 million elements is the benchmark solution.

CFD simulations were performed on successively finer mesh resolutions up until the benchmark solution. The absolute error between the current mesh resolution and the benchmark solution is shown in Figure 7.3.

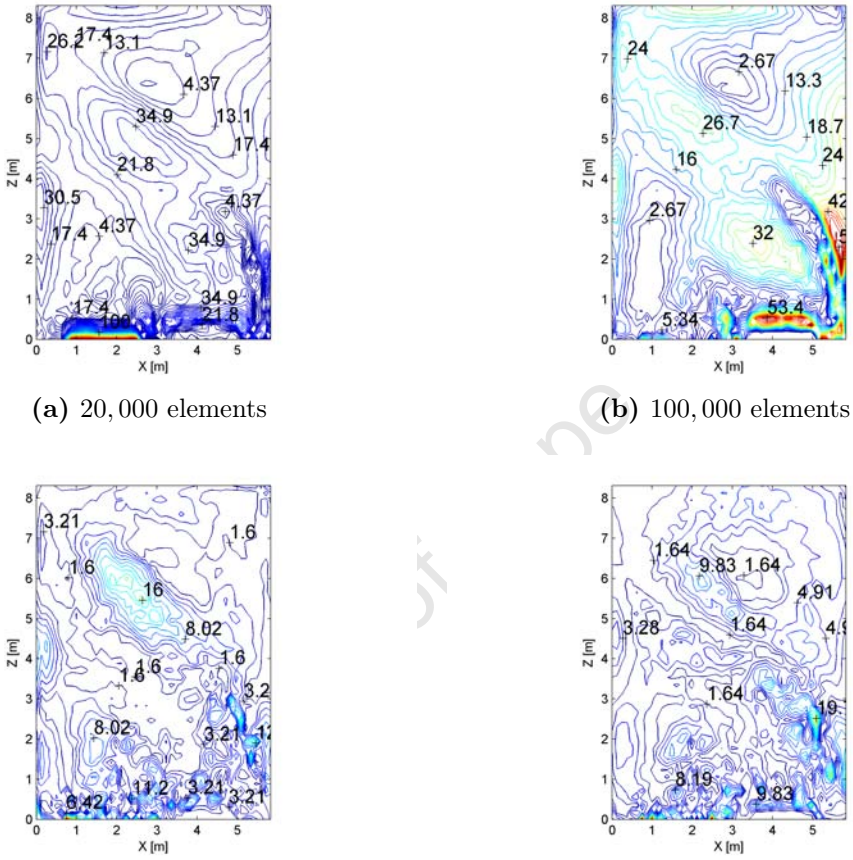


**(a)** 20,000 elements **(b)** 100,000 elements

**(c)** 700,000 elements **(d)** 2 million elements

**Figure 7.3:** Absolute error between the current solution and the benchmark solution of 3.5 million elements. The magnitude of the contour indicates the absolute error. The comparison of velocity vector fields were performed at the $y = 1.15$ plane.

Figure 7.3 shows that initially a high absolute error exists at the inlet. As the mesh is refined, the highest absolute error appears at the outlet with further refinement reducing this error. Below a mesh resolution of 700,000 elements the recirculation zones now becomes important when assessing the error between the current mesh resolution and the benchmark solution of 3.5 million elements.

A more rigorous comparison of the error for each mesh selection was performed through the root mean squared error (RMSE). The velocity fields were interpolated onto a reference grid having the resolution equivalent to the coarsest mesh within the plane. The velocity

fields are normalised using the standard deviation and mean of the finest mesh given by Equation 7.1

$$N_i = \frac{V_i - \mu}{\sigma} \tag{7.1}$$

where $N_i$ is the normalised data of the $i^{th}$ mesh resolution, $V_i$ is the velocity vector field of the $i^{th}$ mesh resolution, $\mu$ is the mean velocity using the finest mesh resolution and $\sigma$ is the standard deviation of the velocity using the finest mesh resolution. Figure 7.4 shows the RMSE for each simulation.

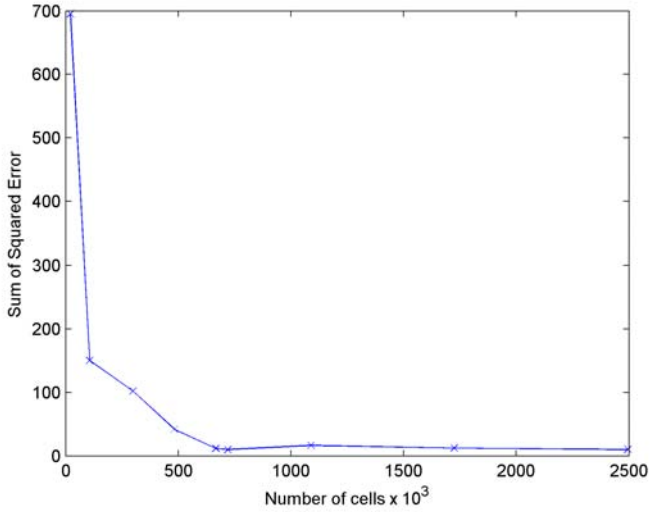


**(a)** Sum of Square Error

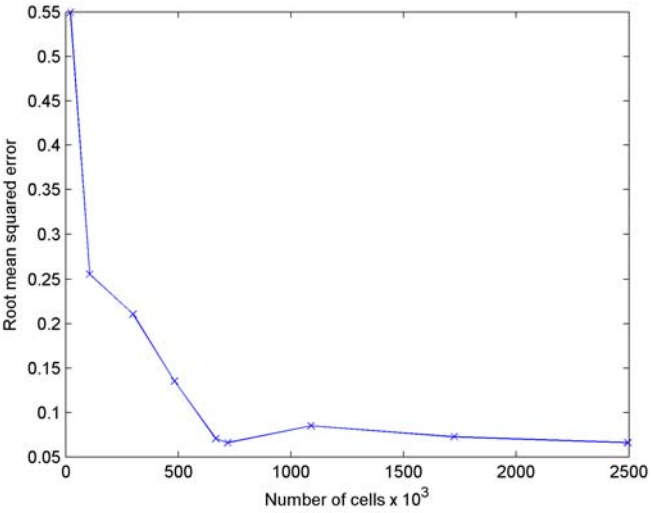


**(b)** Root Mean Squared Error

**Figure 7.4:** Comparison of various mesh resolutions on error

The RMSE begins to plateau around 700, 000 cells. There is a slight increase in the RMSE with an increase in the number of cells. This could be due to the slight shifting of the recirculation zone shown in Figure 7.3. Further refinement eliminates these artefact's.

The mesh resolution of 700,000 cells is used to test the effect of the inlet velocity on the reactor network. The study done by Falcitelli et al. (2002b) found that 13,104 cells was sufficient for validation purposes but did not conduct a mesh independent solution investigation.

## 7.2 Turbulence

For the closure of the system of partial differential equations for turbulent flows, the Boussinesq hypothesis is used. This means that the momentum transport can be modelled by a eddy viscosity. The turbulent eddies are visualised as molecules, colliding and exchanging momentum and obeying laws similar to the kinetic theory of gases (Ranade, 2002). The stresses due to turbulent motions (Reynolds stresses) are given in Equation 7.2

$$\tau_{ij} = \rho \upsilon_t \left( \frac{\partial u_i}{\partial x_j} + \frac{\partial u_j}{\partial x_i} \right) \tag{7.2}$$

where $\tau_{ij}$ are the turbulent Reynolds stresses, $\rho$ is the density $\left[\frac{kg}{m^3}\right]$, $\upsilon_t$ is the kinematic viscosity $[Pa.s]$, $u_i, u_j$ are the mean components of velocity $\left[\frac{m}{s}\right]$. The kinematic viscosity can be obtained from an appropriate turbulence model. The Shear Stress Transport (SST-model) which is a combination of $k-\omega$ and $k-\varepsilon$ turbulence models was used in the simulation since the $\kappa$-$\varepsilon$ model is not able to capture the proper behaviour of turbulent boundary layers up to separation (Menter et al., 2003). Away from the vessel surfaces, the $\kappa-\varepsilon$ model is applied whereas the $\kappa-\omega$ model is used on the boundaries. The eddy viscosity is then coupled to the turbulent flow equations.

## 7.3 Kinetics

The combined Eddy Dissipation/Finite Rate Chemistry combustion model is used for the CFD simulation. For the finite rate, the reduced model is simpler than the comprehensive kinetic model however it still contains 7 species which results in a large CFD equation set making the computation expensive. Hence when simulating the CFD flow fields, a further simplified reaction set is needed. For the purposes of the CFD simulation, the effect of fuel consumption can be approximated by a one-step global reaction to obtain the influence of fuel oxidation on the flow fields (Falcitelli et al., 2002b). This reduction to a one-step global reaction is in effect a local linearisation of the reaction rate rather than a 1st order kinetics approach.

The associated kinetic rate constant was regressed against the reduced kinetic model by Schrieber et al. (1994) to maintain the same features of the fuel consumption. There are two parameters that are regressed to represent the one-step global reaction is the

activation energy and pre-exponential factor. The objective function to be minimised for the regression is given in Equation 7.3

$$MSE_{rate} = \sum_{i=T_0}^{T} \left[ \frac{r_i^{model} - r_i^{exp}}{r_i^{exp}} \right]^2 \tag{7.3}$$

where $r_i^{model}$ is the rate predicted by the 1st order model $\left[\frac{mol}{m^3.s}\right]$, $r_i^{exp}$ is the rate predicted by the reduced mechanism $\left[\frac{mol}{m^3.s}\right]$. The simplex method is used to optimise the two kinetic parameters, activation energy and pre-exponential factor. The results are shown in Figure 7.5 and Figure 7.6.

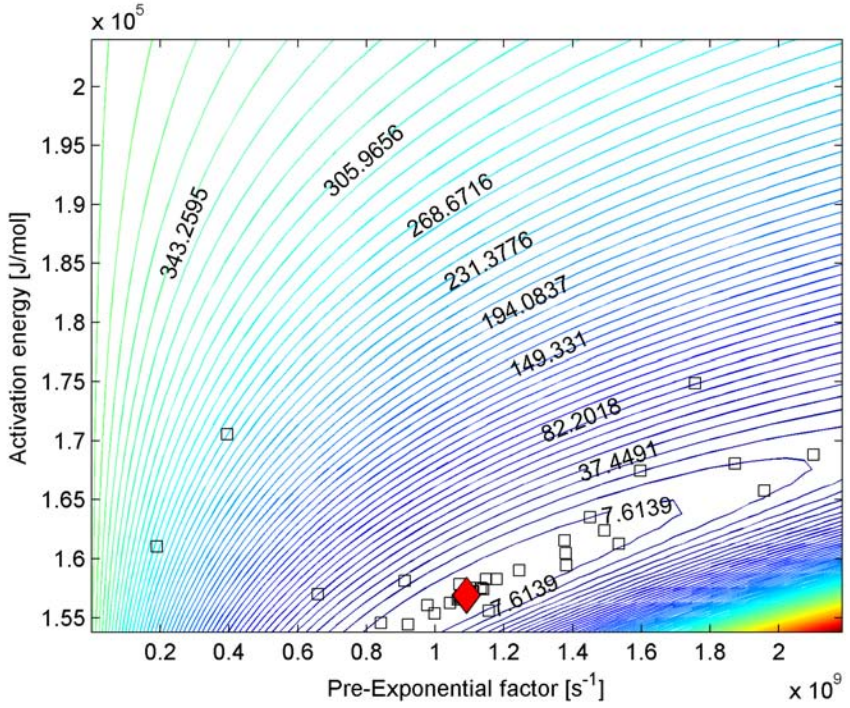


**Figure 7.5:** Sensitivity of the MSE with respect to the Arrhenius pre-exponential factor and Activation energy. The contour indicates the magnitude of the MSE. □ indicates the advancement taken by the optimisation algorithm towards the global minimum. The global minimum is indicated my the red ◊

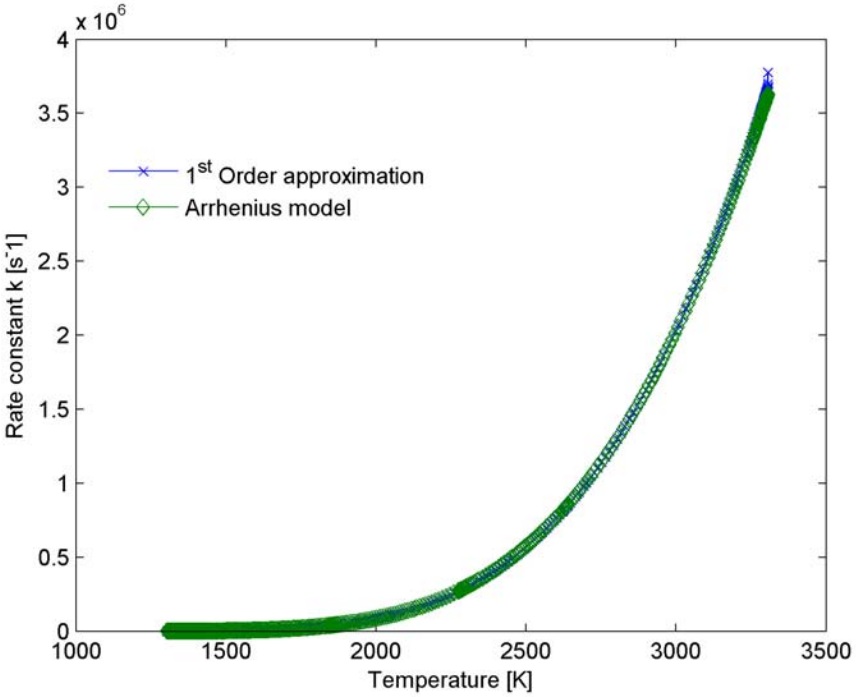


**Figure 7.6:** Kinetic fit of the reduced scheme to the $1^{st}$ order approximation

In Figure 7.5, it can be seen that taking an initial guess for the parameters below the minimum would see the optimisation algorithm converge faster than when taking an initial guess above the minimum since there exist a larger gradient below the minimum as apposed to above the minimum. Once in the region of the local minimum, the surface is fairly flat causing gradient based algorithms to be slow or even fail. The simplex method is thus best suited.

Figure 7.6 shows the closeness of the fit with the minimum MSE calculated as 0.0468. The resulting parameters are given in Equation 7.4.

$$r(C_8H_{18} + 12.5O_2 \rightarrow 8CO_2 + 9H_2O) = \\ 1.0919 \times 10^9 exp\left[\frac{-156920}{RT}\right] C_{C_8H_{18}} \tag{7.4}$$

The $Ea \approx 38\ \frac{kcal}{mol}$ correlates well with values presented in literature (Kahandawala et al., 2006). The $1^{st}$ order kinetic model is used to predict the finite rate of the reaction in the CFD simulation. In the present work the combined Eddy Dissipation/Finite Rate Chemistry combustion model is adopted.

The Eddy Dissipation combustion model (EDM) is based on the hypothesis that the chemical reaction is fast in comparison with the transport processes of the flow (Widenhorn et al., 2008). The EDM assumes that the energy cascade process also controls the chemical reaction. A more detailed explanation is available in Peters (2000). Equations 7.5 - 7.7 are used in the EDM

$$\overline{\omega_f} = -\overline{\rho} A \overline{Y_f} \frac{\varepsilon}{k} \tag{7.5}$$

$$\overline{\omega_{O_2}} = -\overline{\rho} \frac{A \overline{Y_{O_2}}}{\nu} \frac{\varepsilon}{k} \tag{7.6}$$

$$\overline{\omega_P} = \overline{\rho} \frac{A \cdot B}{(1+\nu)} \overline{Y_P} \frac{\varepsilon}{k} \tag{7.7}$$

where the values of $\kappa \left[\frac{m^2}{s^2}\right]$ and $\varepsilon \left[\frac{m^2}{s^2}\right]$ are obtained from the $\kappa$-$\varepsilon$ turbulence model, the parameters $A$ and $B$ must be regression for each flow regime of interest, $\overline{Y_f}, \overline{Y_{O_2}}, \overline{Y_P}$ is the mole fraction of fuel, oxygen and product respectively. The EDM takes assumes that one of the above reactions is rate limiting thus the minimum of the three rates is used to calculate the mean reaction rate.

The Finite Rate Chemistry combustion model is based on the assumption that the mixing is much faster than the kinetically controlled processes (Widenhorn et al., 2008).

The combined Eddy Dissipation/Finite Rate Chemistry combustion model calculates all the reaction rates , EDM and finite rate, separately taking the chemical source term as the minimum value of both models since one of the above reactions is rate limiting.

## 7.4 Conclusion

Both geometries under investigation have been fully defined in terms of the CFD boundary conditions and relevant kinetic parameters. The CFD vector fields can be simulated and used as the basis to conduct the hydrodynamic investigation to propose an equivalent chemical reactor network. The CFD simulations can also be performed at various inlet velocities to ascertain its effect on the proposed network.

# Chapter 8

# Compartment Model

The basis of this study is to propose a fast solving chemical reactor network that serves as an equivalent to the computationally expensive CFD simulations. The compartmentalisation is the methodology adopted in proposing the reactor network. The chemical reactor network (CRN) is proposed on the basis of the vector fields obtained from the CFD simulation. The CFD simulations were completed using the conditions explained in Chapter 7. This section describes how the network was developed for the two geometries introduced in the preceding section.



## 8.1 Methodology

Work done by Ponsich et al. (2009) described two CRN approaches that exist namely Dynamic and Static. In the Dynamic case, a signal is subjected to a variation in the input concentration of a tracer either in the form of a Dirac pulse or a step injection. The Residence Time Distributions (RTD) obtained from the perturbation is used to propose the CRN. The RTD obtained provides inference into the mixing characteristics within the domain but does not provide information on the spatial distribution inside the reactor unless the pulse is simulated to travel through the domain. This approach is computationally expensive since it involves solving the unsteady CFD equations coupled with turbulent chemically reacting flow.

The static approach uses the CFD steady state vector fields to propose a CRN. The static approach can give you the spatial distribution in the domain but solution convergence can be difficult unless the initial guess for the field is very good. The static approach is used for the present study due to the relatively low computational demand when compared to the dynamic case.

The methodology explained by Falcitelli et al. (2002a) uses the static case for the CRN selection and is given as follows:

1. The stoichiometric field within the domain is calculated and is defined as the ratio

of available to requested oxygen on a mass basis.

2. The selection of homogeneous zones is defined clustered zones in the plot of temperature versus stoichiometry for the domain.

3. The homogeneous zones are modelled as continuous stirred tank reactors (CSTR's) or plug flow reactors (PFR) on the basis of velocity vector fields in the zone. A CSTR is represented by velocity vectors that are randomly distributed and/or have recycling zones. A PFR is represented by velocity vectors in a one-directional flow.

4. The total reactor volume is divided into sub volumes using a fractional approach. The volume of each sub volume (ideal reactor) is taken as the sum of the cells volume belonging to that zone. The reactors are to be adiabatic and non-isothermal with the entrance temperature dictated by the adjoining reactors exit temperature.

5. The mass exchange between the reactors are computed by the flow volumes dictated by splitting and mixing of streams within the network. The stream split fractions are estimated from the mass flows between cells belonging to different reactors.

The work done by Falcitelli et al. (2002a) considered the reactors to be isothermal at the operative temperature computed from CFD temperature field by an enthalpy conserving expression. This restricted the predictive nature of their network. An improvement presented in this study is to allow the ideal reactors to operate at temperatures governed by the differential energy balance giving the current model a more predictive ability. This allows the ideal compartments to thermally interact since the exit temperature from the one compartment determines the inlet temperature to the other compartments. Claudel et al. (2003) showed that the compartment networks should have at most three branches in parallel as this would reduce network complexity and computational time. This was also considered when proposing a CRN for the current study.



## 8.2 Network Selection

The modified methodology for CRN selection as was explained by Falcitelli et al. (2002a) is now applied to the CFD vector fields. The CFD vector field for the two geometries is used as the basis for the CRN.

### 8.2.1 Double Inlet Reactor

The static CFD vector fields in the double inlet reactor are shown in Figure 8.3 and 8.4. Figure 8.3 and 8.4 combined with the stoichiometric field in the planes (Figure 8.2) shows that the reactor can be divided into four zones, two reacting zones and two mixing zones.

Figure 8.1 shows the stoichiometry as a function of temperature. It was assumed that the reactor operates at a high temperature and a low temperature region indicated in Figure 8.1. The volume of the each zone is calculated by summing the volume of all the cells belonging to a particular zone. The volume split between the four zones can be seen in Figure 8.3 with the volume percents given in Table 8.1.

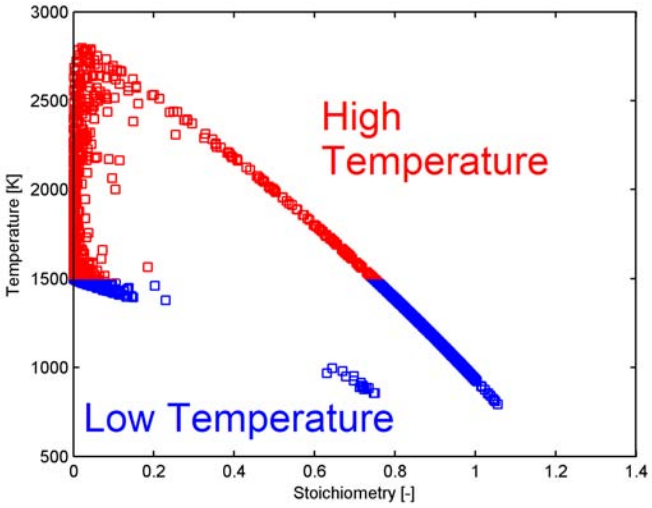


**Figure 8.1:** Stoichiometry VS temperature for the double inlet reactor

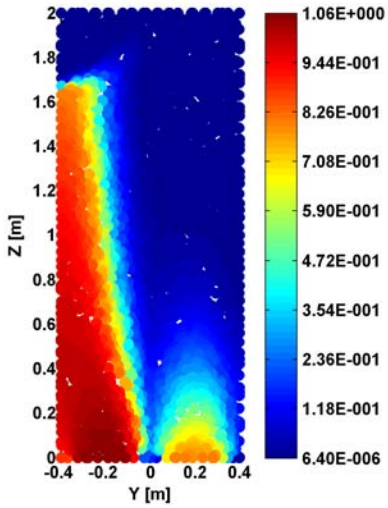


**(a)** Stoichiometry at the $x = 0$ plane. The magnitude of the stoichiometry is indicated by the colour bar

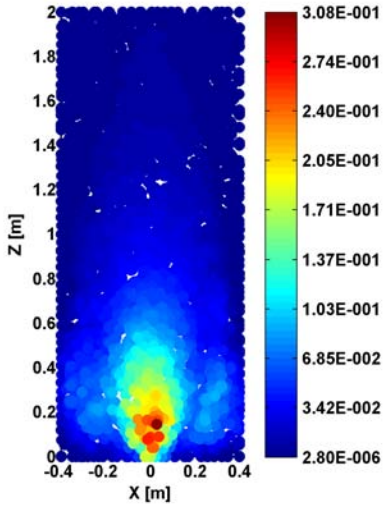


**(b)** Stoichiometry at the $y = 0$ plane. The magnitude of the stoichiometry is indicated by the colour bar

**Figure 8.2:** Stoichiometry at various planes in domain for the double inlet reactor. Inlet velocity = 1 m/s

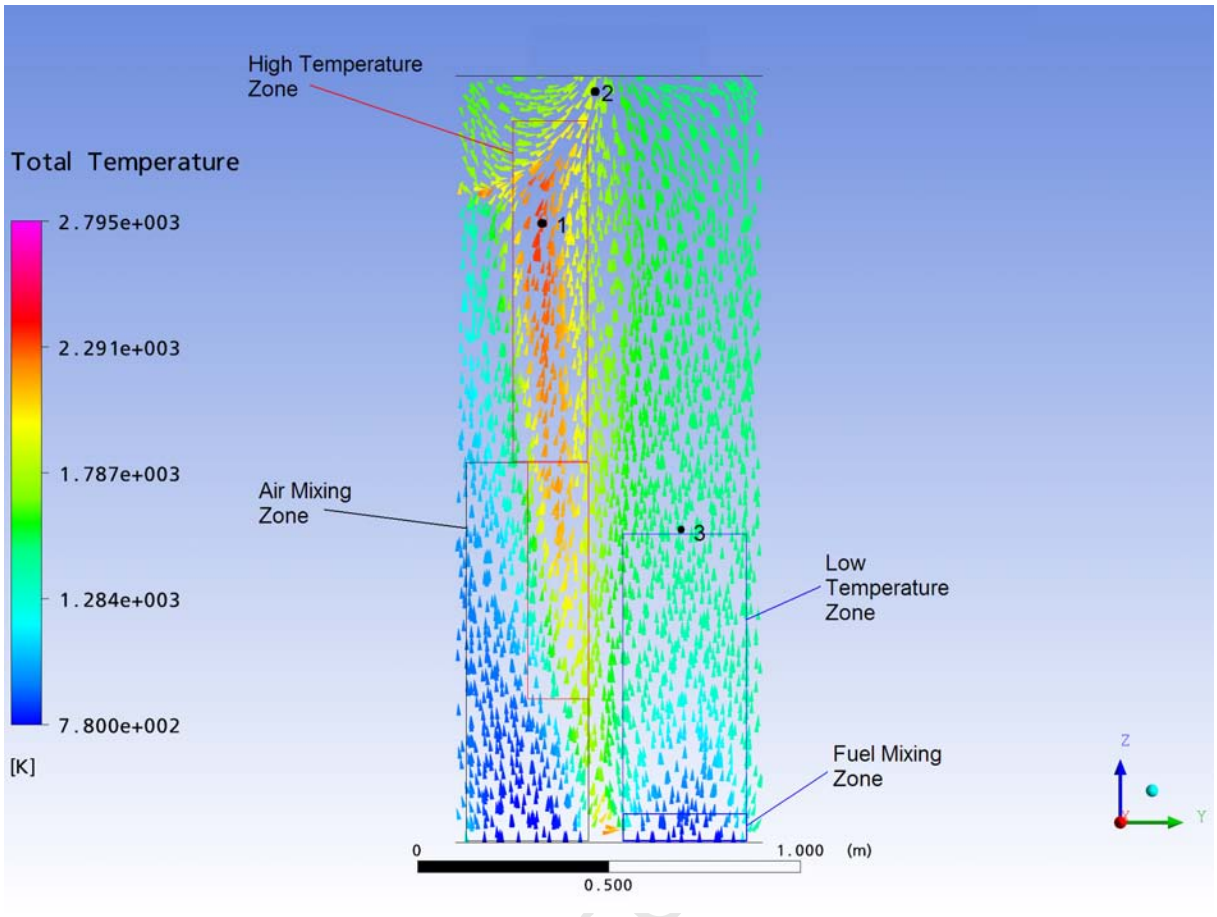


**Figure 8.3:** Velocity vector field at the $x = 0$ plane. The vectors are coloured temperature. The different zones are indicated by the rectangular regions. Data points 1, 2 and 3 indicate the comparison points between the CFD and compartment model. Inlet velocity $= 1$ m/s

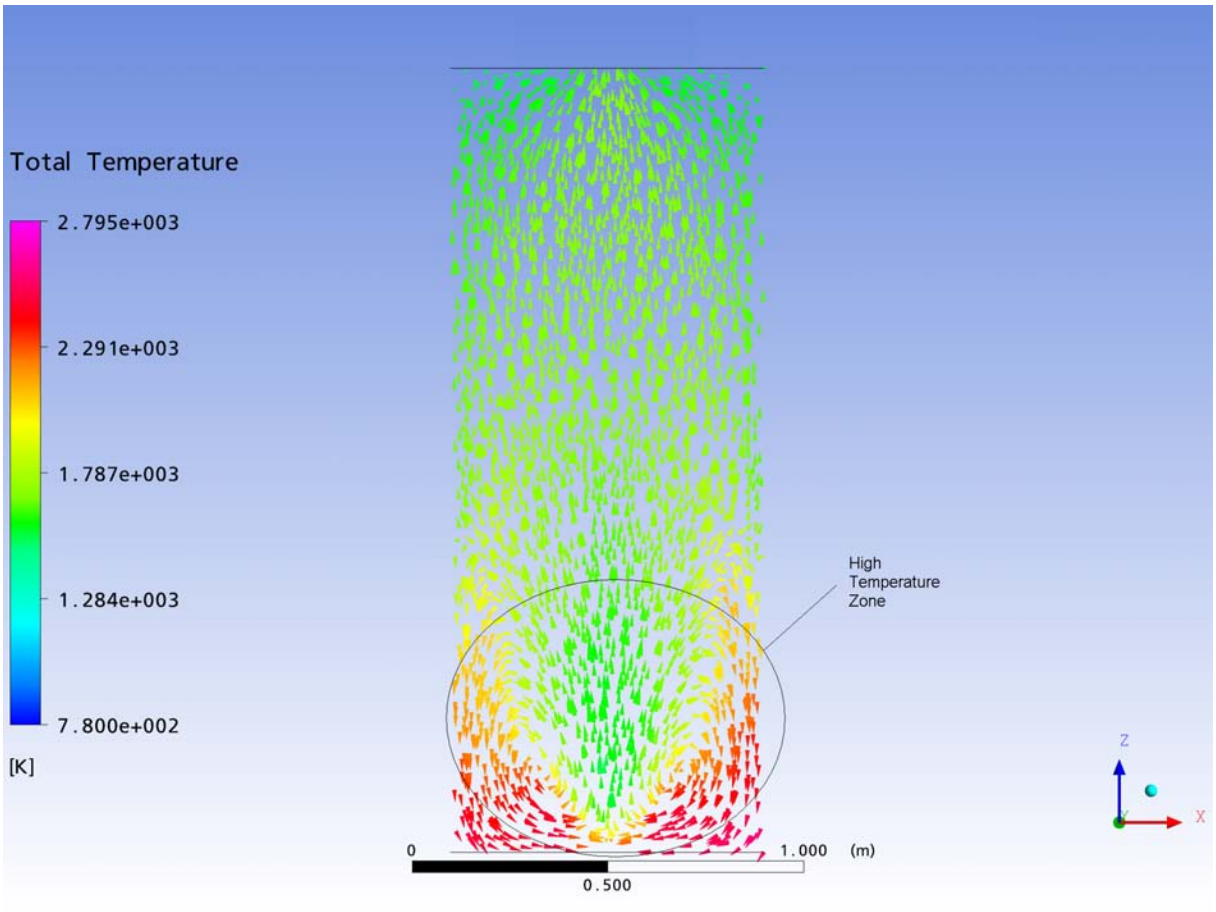


**Figure 8.4:** Velocity vector field at the $y = 0$ plane. The vectors are coloured by the magnitude of the temperature. Inlet velocity = 1 m/s

| Parameter | Percentage |
|---|---|
| High temperature zone | 45% |
| Low temperature zone | 35% |
| Air mixing zone | 15% |
| Fuel mixing zone | 5% |

**Table 8.1:** Volume percent between the zones for the double inlet reactor

For this particular choice of the number of zones, zone volume of each zone, and zone connectivity, the classification of each zone is required to synthesise a network. From Figure 8.3 and 8.4 it can be seen that the air and fuel mixing zones (indicated by the marked rectangular regions) are plug flow in nature due to the one directional flow pattern. The low temperature reaction zone is also plug flow in nature for this same reason. Conversely, the high temperature reactor comprises of two zones, one plug flow region and a larger CSTR region as seen in Figure8.3 and 8.4. The PFR zone has a small size contribution to the high temperature zone thus the high temperature zone is modelled solely as a CSTR.

The flow rates and flow splits between the zones are also of importance. It is assumed

that the fuel and air stream are split such that a portion of the each streams (fuel and oxygen) participates in the high temperature reactor region and the low temperature reactor region respectively. The magnitude and composition of the flow between the zones are calculated based on the split ratios ($\lambda$ , $\Omega$) given to the network. The reactor network proposed is thus given in Figure 8.5.

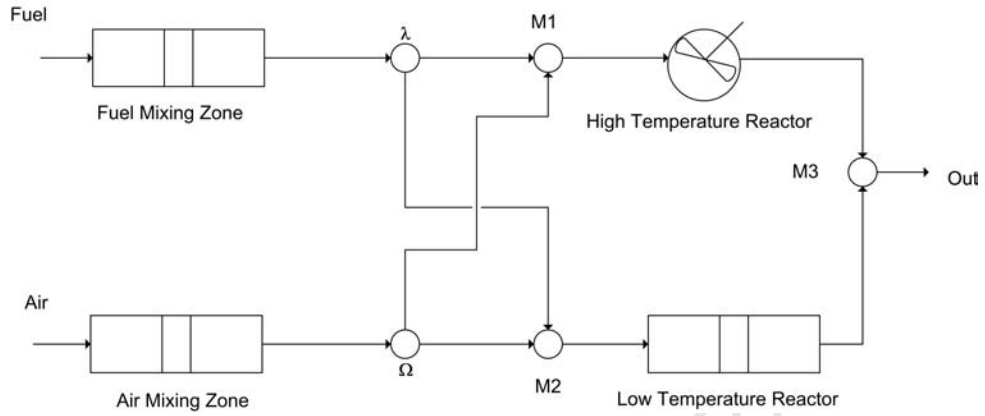


**Figure 8.5:** Proposed network based on the double inlet reactor flow fields

The network requires certain parameters be specified before it can be solved. These are:

1. $\lambda$ - Fraction of incoming fuel stream that is split to the low temperature reactor
2. $\Omega$ - Fraction of incoming air stream that is split to the low temperature reactor

Once the parameters are specified, the network was simulated on a personal computer with a Intel® Core 2 Duo$^{TM}$ processor. The CPU time demands for the plug flow reactor was 1.5 seconds, while for a perfectly stirred reactor it was 0.7 seconds. The total CPU time for the network is 5.1 seconds. This is a significant advantage of having a compartment model; it simulations so much faster than a CFD model and it makes real-time control feasible. The CRN also allows for a better understanding of the hydrodynamic structure of the fluid flowing inside the reactor.

### 8.2.2 Furnace

The static CFD vector fields in the furnace are shown in Figure 8.6 and 8.7. When combined with the stoichiometric field in the planes (Figure 8.9a and 8.9b) it is clear that the furnace can be divided into two zones. The larger of the two zones have different vector fields and thus have been further divided into two sub-zones. Figure 8.8 shows the stoichiometry as a function of temperature. The linear relation is similar to that seen in Figure 8.1 but the spread of data is not as significant. This is seen since most of the fuel and oxygen are consumed within the first zone of the domain. The volume of the each

zone is calculated by summing the volume of all the cells in the CFD mesh identified as belong to that particular zone. The volume split between the three zones (Z1, Z2, Z3) can be seen in Figure 8.6 with the volume percents given in Table 8.2.

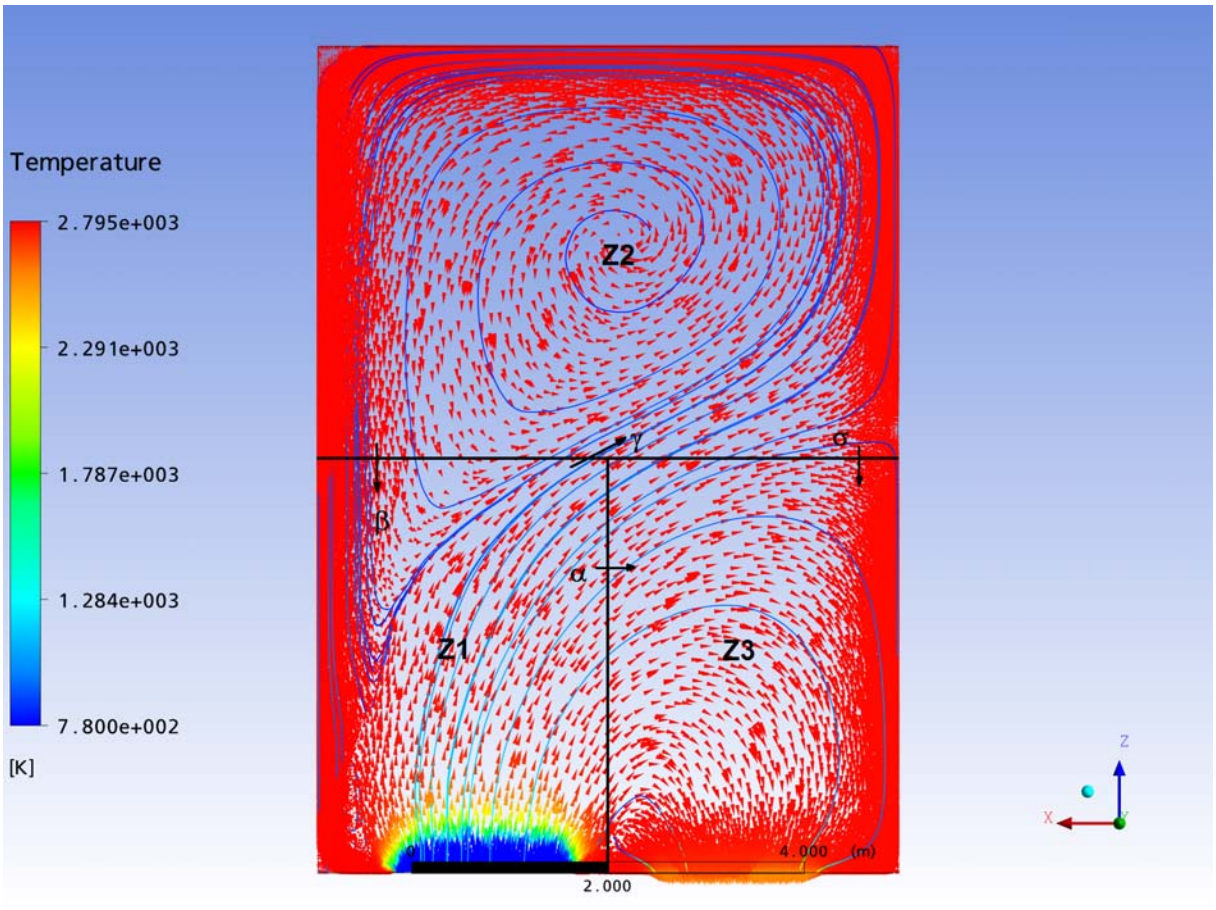


**Figure 8.6:** Velocity vector field at the $y = 1.15$ plane. The vectors are coloured by temperature. $Z1$, $Z2$, $Z3$ indicate the different zones present in the network. Greek symbols indicate the flow between the zones. . Inlet velocity = 126 m/s

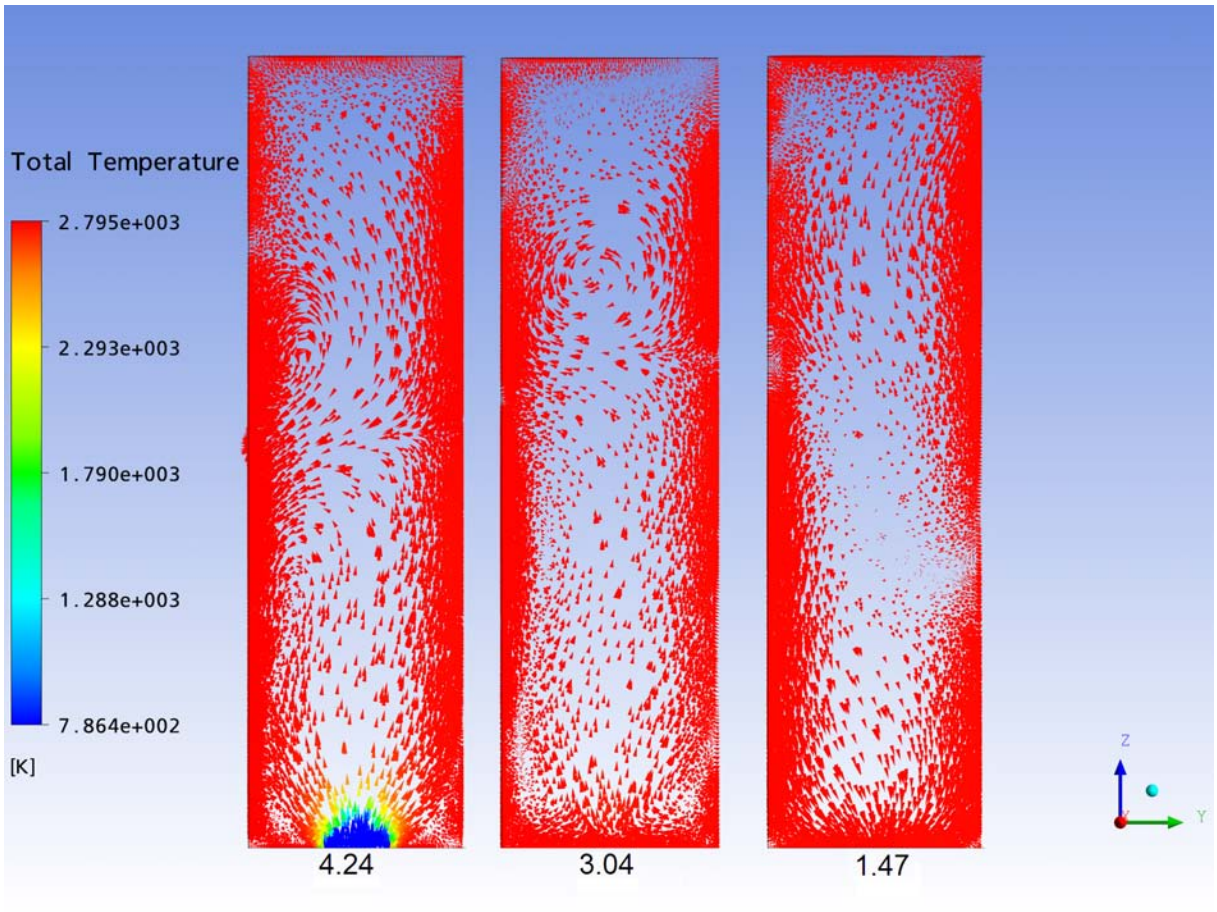


**Figure 8.7:** Velocity vector field at the various $x$ positions. The vectors are coloured by temperature. Vector fields from left to right: Inlet, Centre, Outlet . Inlet velocity = 126 m/s

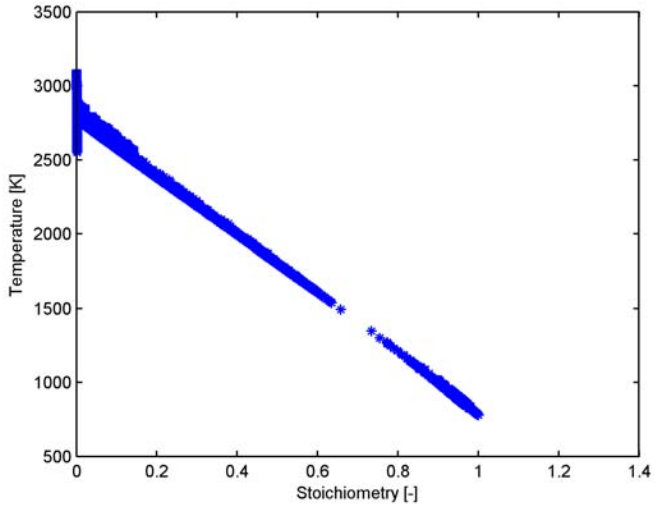


**Figure 8.8:** Stoichiometry VS temperature for the furnace

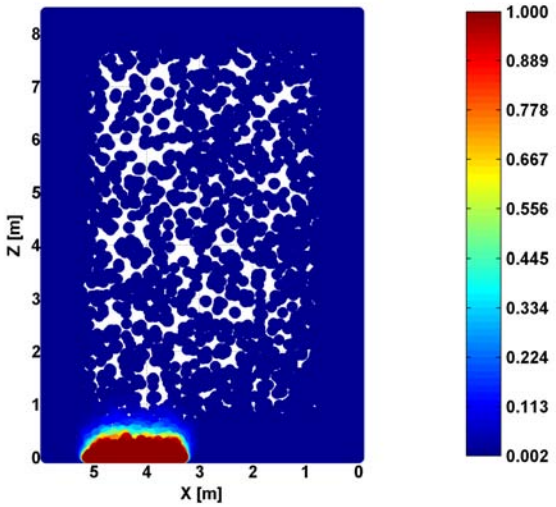


**(a)** $y = 1.15$ plane. The magnitude of the stoichiometry is indicated by the colour bar

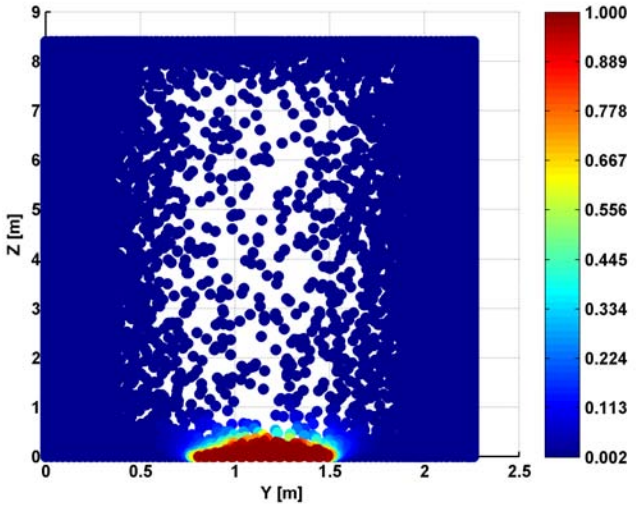


**(b)** $x = 4.24$ plane. The magnitude of the stoichiometry is indicated by the colour bar

**Figure 8.9:** Stoichiometry at various planes in domain for the furnace. Inlet velocity = 126 m/s

| Parameter | Percentage |
|---|---|
| Z1 | 20.8% |
| Z2 | 53.3% |
| Z3 | 25.8% |

**Table 8.2:** Volume percent between the zones for the furnace

Now that the number of zones and the volume of each zone has been specified, the classification of each zone is required to synthesise a network.

From Figure 8.6 and 8.7 it can be seen that Z2 and Z3 exhibit a high degree of mixing

with one recirculation region whereas Z1 has slightly one dimensional flow behaviour. It is proposed that Z1 be modelled as a plug flow reactor with a back mixing component since the vector fields indicate that the flow is not ideally plug flow. Zone 2 and 3 are proposed as CSTR models because of the high degree of mixing with recirculation in these zones.

The flow between the zones are also of importance and is given by $\alpha, \beta, \gamma, \sigma$ in Figure 8.6 and Figure 8.10. The magnitude and composition of the flow between the zones are calculated based on the split ratios ($\kappa_1$ , $\kappa_2$ ) given to the network. The proposed reactor network is given in Figure 8.10.

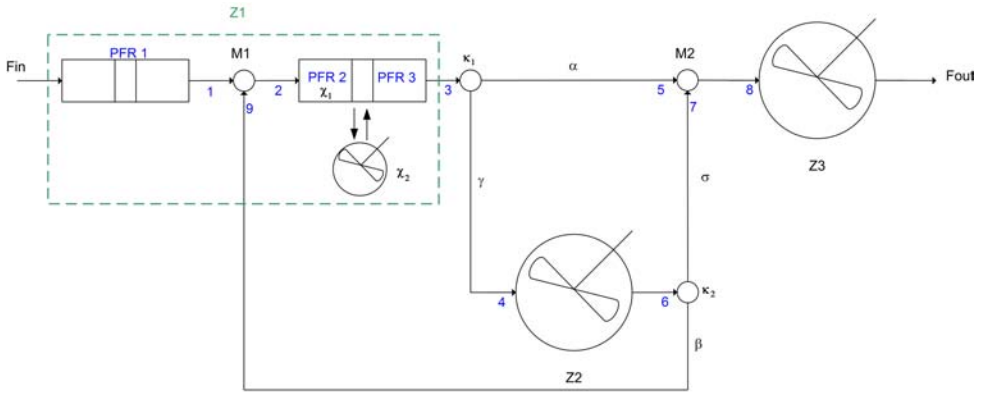


**Figure 8.10:** Proposed network based on the furnace flow fields

The network requires certain parameters to be specified before it can be solved. These are:

1. $\kappa_1$ - Fraction of incoming stream that is split to zone 2
2. $\kappa_2$ - Fraction of incoming stream that is split to zone 1
3. $\chi_1$- Fraction of Z1 that is dedicated to PFR 2
4. $\chi_2$- Fraction of PFR 2 that is back mixed

Once the parameters are specified, the network was simulated on a personal computer with a Intel® Core 2 Duo$^{TM}$ processor. The network is iterated 10 times such that the recycle stream (Stream 9 in Figure 8.10) is converged. The total CPU time for solving the network is 22 seconds. Again this is a significant advantage of having a compartment model. The CRN for the furnace has more complex hydrodynamics as compared to the two inlet reactor geometry but the CRN is still able to give a simplistic insight into the hydrodynamic structure of the fluid flowing inside the reactor.

## 8.3 Conclusion

The methodology available in literature for CRN development has been modified and applied to two geometries. Preliminary results show that the CRN is much faster and

more computationally efficient when compared to the CFD simulation. The current CRN is also more predictive in terms of temperature. The CRN was proposed with a reliance on certain parameters before it can be solved. The CRN can be related to the input velocity through these parameters. This is done by using regression and mathematically correlating the parameters. This would make the network more predictive and allow the model to get closer to industrial conditions.

# Part III

# Simulation Results and Discussion

# Chapter 9

# Idealised Reactor Simulations

The methodology available in literature for CRN development has already been discussed in the preceding chapters. The basis of the CRN is the ideal reactor compartments which require validation before they can be applied to the CRN. The kinetic model presented by Griffiths (1994) was parametrised and tuned against experimental batch reactor data by Schrieber et al. (1994). In this chapter, the kinetic model is validated using the tuned parameters given by Schrieber et al. (1994). The PFR and CSTR models which use the regressed thermodynamic properties for the pseudo species is also validated in this section.



## 9.1 Kinetic Validation

The reduced kinetic model was simulated in a constant volume batch reactor since corresponding experimental data could be used for the purpose of validation. The reduced kinetic model developed by Schrieber et al. (1994) assumes a constant heat capacity of 36 $\frac{J}{mol.K}$ for all species in the system. This heat capacity is used in the current batch reactor model with the results being compared to data given by Schrieber et al. (1994) for kinetic validation. The results of the batch reactor simulation are shown in Figure 9.1 and Figure 9.2.

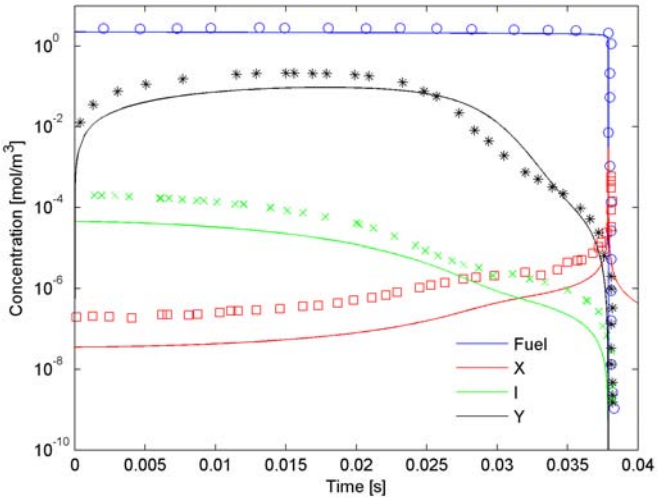


**(a)** Initial conditions: $P_0 = 8.85$ bar; $T_0 = 780$ K.

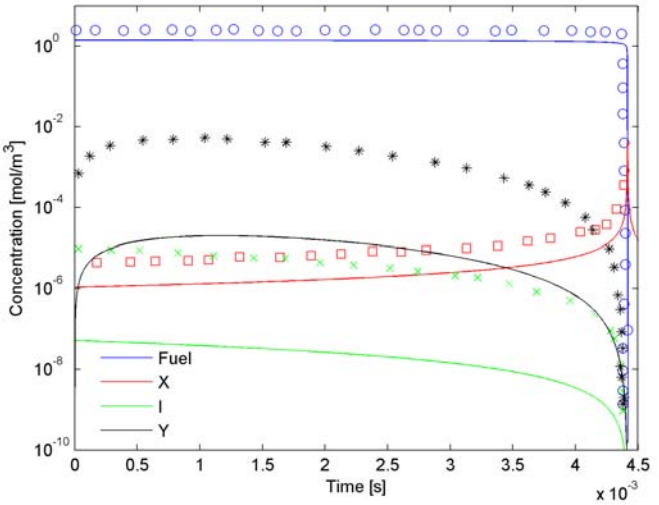


**(b)** Initial conditions: $P_0 = 7.1$ bar; $T_0 = 1000$ K.

**Figure 9.1:** Concentration profiles in a batch reactor at different input conditions. Molar composition: $iC_8H_{18}/O_2/N_2 = 1/12.5/47$. The symbols corresponds to data presented in Schrieber et al. (1994)

Comparison of the current batch model to the experimental data shows that the concentration profiles in Figure 9.1 corresponds well with the data provided in Schrieber et al. (1994). The current model has a slightly higher deviation from the data presented in Schrieber et al. (1994) at the initial temperature of 1000 K. This may suggest that the kinetic parameters tuned by Schrieber et al. (1994) may apply to certain ranges of initial temperature.

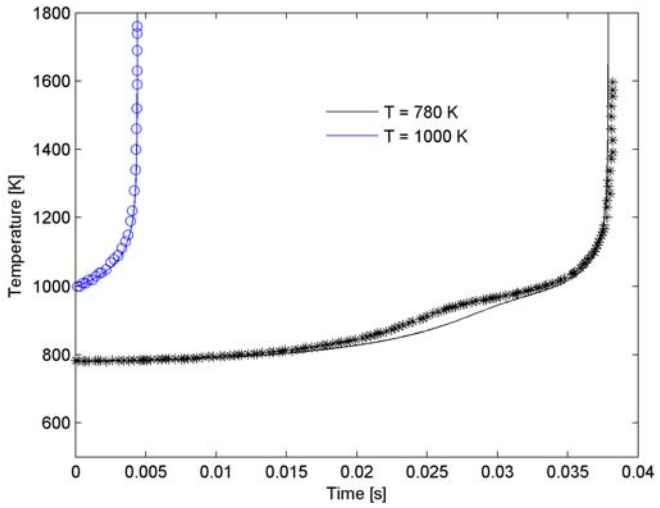


**Figure 9.2:** Temperature profiles in a batch reactor at different input conditions. Molar composition: $iC_8H_{18}/O_2/N_2 = 1/12.5/47$. The symbols corresponds to data presented in Schrieber et al. (1994)

The current models temperature profiles presented in Figure 9.2 corresponds well with the data presented by Schrieber et al. (1994). The second stage ignition is slightly underestimated at higher initial temperatures. However, the experimental ignition delay time and ignition time delay predicted by the current model is the same, suggesting that the kinetic parameters given in Table 4.1 is applicable over a wide initial temperature range. Figure 9.3 shows the ignition time delay for the current batch model and the data presented in Schrieber et al. (1994).

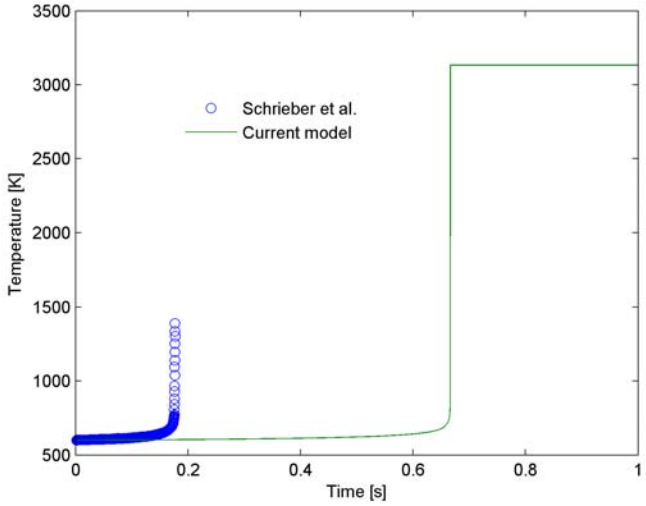


**Figure 9.3:** Temperature profiles in a batch reactor at $T_0 = 600K$. Molar composition: $iC_8H_{18}/O_2/N_2 = 1/12.5/47$.

The kinetic parameters given in Schrieber et al. (1994) does not correspond to the correct ignition time delay when the model is simulated at $T_0 = 600K$. The kinetic

parameters given in Table 4.1 thus does not apply at low initial temperatures. The low temperature parameters will need to be regressed against suitable experimental data. For the purposes of this study, initial temperatures above 780 K are used in conjunction with the kinetic parameters given in Table 4.1.

## 9.2 Plug Flow Reactor

The reduced model was simulated in a plug flow reactor using the heat capacities regressed for the lumped components given in Table 5.1 required for the calculation of the species enthalpies. The reduced model was validated in a PFR against a detailed kinetic mechanism developed by Curran et al. (2002) and is given in Figure 9.4.

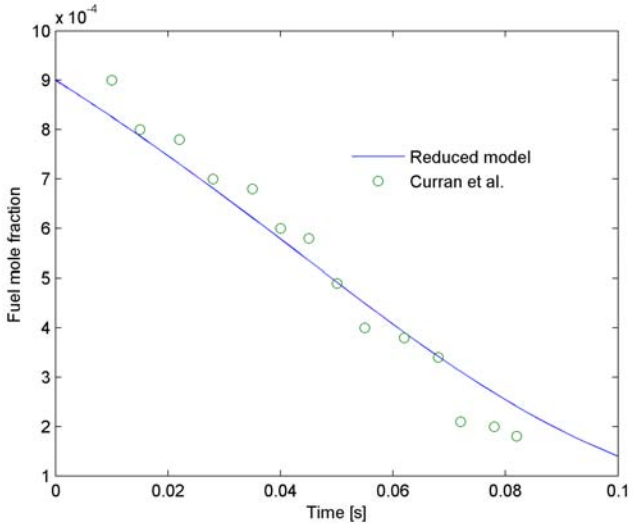


**Figure 9.4:** 0.09% iso-octane oxidation in a PFR, $\phi = 0.05$, $P = 6$ atm

The data provided in Curran et al. (2002) was simulated at an initial temperature of 945 K whereas the current model was simulated at an initial temperature of 1000 K to obtain the correct trends. The reduced model tends to over predict the fuel consumption at a lower initial temperature due to the lumped approach being too simplified to obtain the exact trends in fuel consumption. Using the initial temperature difference of 55 K, there is good agreement between the reduced model and detailed mechanism developed by Curran et al. (2002). Thus, it can be assumed the reduced mechanism is able to predict with some accuracy the same characteristics as the detailed mechanism using the regressed heat capacities and heats of formation.

The PFR was also simulated at the same initial conditions at which the batch reactor data was validated. The results are shown in Figure 9.5, Figure 9.6 and Figure 9.7. Iso-octane combustion in a PFR shows that there exists two pathways during the combustion event, namely high temperature and low temperature pathway.

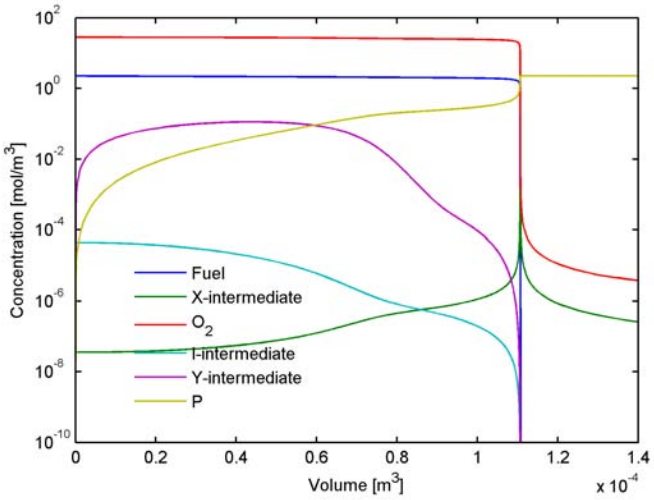


**Figure 9.5:** Concentration profiles in a plug flow reactor.
Molar composition: $iC_8H_{18}/O_2/N_2 = 1/12.5/47$. Initial conditions: $P_0 = 8.85$ bar; $T_0 = 780$ K; Radius = 0.08 m; Volumetric flow rate = $0.0021\frac{m^3}{s}$

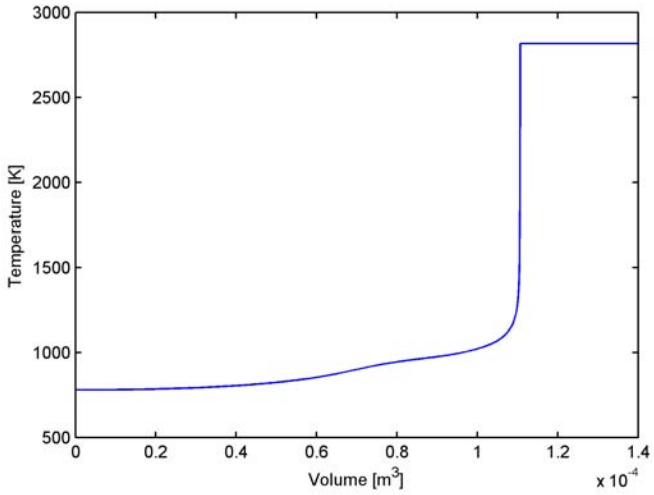


**Figure 9.6:** Temperature profile in a plug flow reactor. Molar composition: $iC_8H_{18}/O_2/N_2 = 1/12.5/47$. Initial conditions: $P_0 = 8.85$ bar; $T_0 = 780$ K; Radius = 0.08 m; Volumetric flow rate = $0.0021\frac{m^3}{s}$

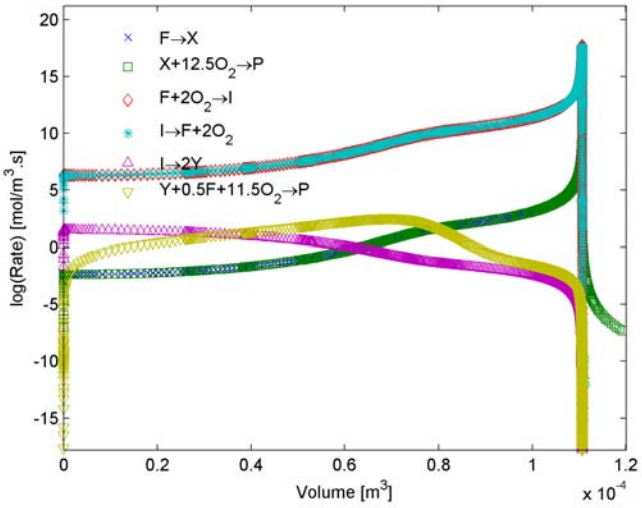


**Figure 9.7:** Reaction rates in a plug flow reactor. Molar composition: $iC_8H_{18}/O_2/N_2 = 1/12.5/47$. Initial conditions: $P_0 = 8.85$ bar; $T_0 = 780$ K; Radius = 0.08 m; Volumetric flow rate = $0.0021\frac{m^3}{s}$

When the temperature is low (Figure 9.6 and Figure 9.7), reactions 4 and 5 are dominant with reaction 4 having a slightly higher reaction rate. When the temperature is high, reactions 1 and 2 are dominant. A more detailed explanation of the reaction pathways is explained in Section 4.2. The variable for the batch model is time whereas the variable for the PFR is space. The space variable can be related to time by using the velocity making the batch model and PFR equivalent. Since the PFR is not time dependent, the point at which the fuel is completely combusted can not be termed the ignition time delay. Instead, the distance along the PFR at which the fuel is completely combusted can be thought of as the flame front (Turns, 2000). Generally speaking, the results shown in Figure 9.5, Figure 9.6 and Figure 9.7 still exhibit the phenomena of self ignition and cool flame behaviour when using the regressed thermodynamic parameters.



## 9.3 Continuous Stirred Tank Reactor

As in the case above, the reduced model was simulated in a continuous stirred tank reactor by using the regressed heat capacities for the lumped component given in Table 5.1 for the calculation of the species enthalpies. The results of the reactor simulation are shown in Figure 9.8, Figure 9.9 and Figure 9.10. The same two stage phenomenon is observed for iso-octane combustion in the CSTR. The same kinetic pathway as was described for the PFR occurs during a CSTR combustion event. A more detailed explanation of the reaction pathways is explained in Section 4.2.

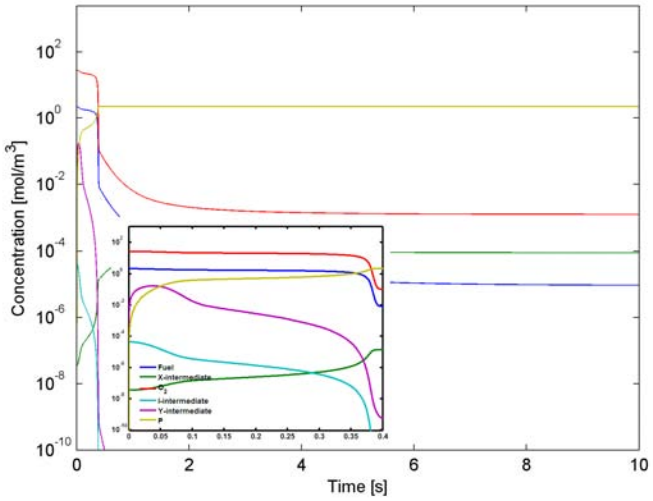


**Figure 9.8:** Concentration profiles in a continuous stirred tank reactor. Molar composition: $iC_8H_{18}/O_2/N_2 = 1/12.5/47$. Initial conditions: $P_0 = 8.85$ bar; $T_0 = 780$ K; Volume $= 0.5\ m^3$; Volumetric flow rate $= 1\frac{m^3}{s}$

Figure 9.8 shows the concentration profiles of the species in the reactor as a function of time. It can be seen that at steady state, the fuel is not completely combusted in the reactor. This is due to the influence of the flow terms in the model equations. Fresh fuel and oxygen are continuously entering the reactor, thus complete conversion of the fuel is not achieved.

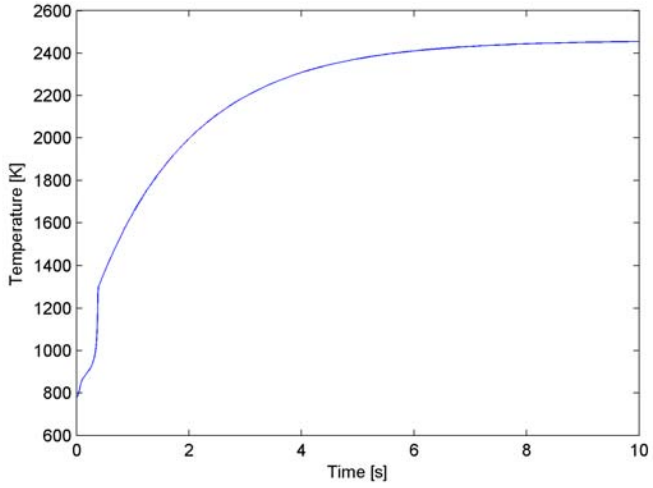


**Figure 9.9:** Temperature profile in a continuous stirred tank reactor. Molar composition: $iC_8H_{18}/O_2/N_2 = 1/12.5/47$. Initial conditions: $P_0 = 8.85$ bar; $T_0 = 780$ K; Volume $= 0.5$ $m^3$; Volumetric flow rate $= 1\frac{m^3}{s}$

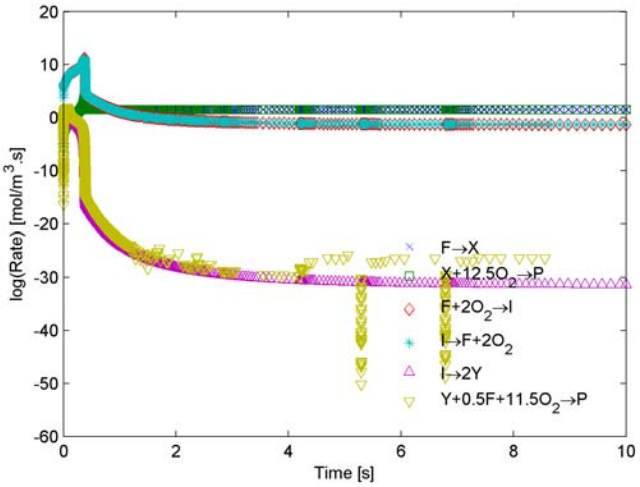


**Figure 9.10:** Reaction rate profiles in a continuous stirred tank reactor. Molar composition: $iC_8H_{18}/O_2/N_2 = 1/12.5/47$. Initial conditions: $P_0 = 8.85$ bar; $T_0 = 780$ K; Volume $= 0.5\ m^3$; Volumetric flow rate $= 1\frac{m^3}{s}$

The temperature profile in a CSTR (Figure 9.9) shows the characteristics of two stage ignition as a result of the low and high temperature pathways. The cool flame region is more pronounced in the CSTR model. The results in a CSTR exhibit the phenomena of self ignition and cool flame behaviour using the regressed thermodynamic parameters.

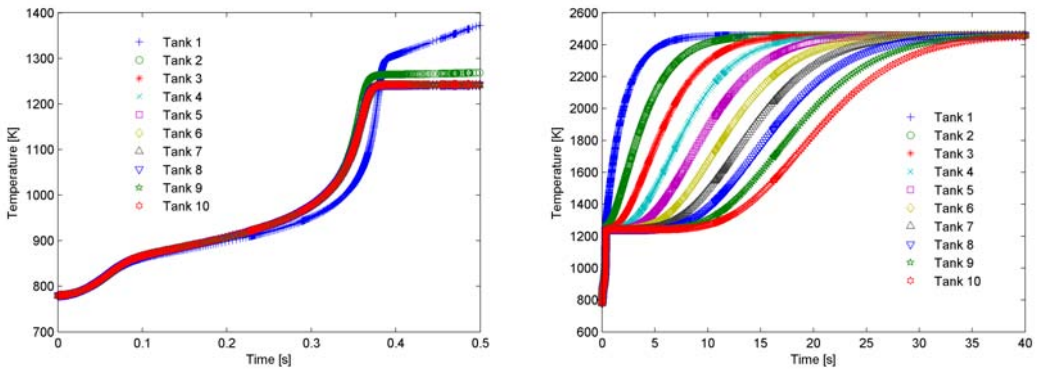


**Figure 9.11:** Temperature profile in a continuous stirred tank reactor. Molar composition: $iC_8H_{18}/O_2/N_2 = 1/12.5/47$. Initial conditions: $P_0 = 8.85$ bar; $T_0 = 780$ K; Volume per tank $= 0.5\ m^3$; Volumetric flow rate to each tank$= 1\frac{m^3}{s}$

Iso-octane combustion was simulated in a tanks-in-series model, Figure 9.11. The effluent from the first tank is the input into the second tank until the effluent from the last tank is taken as the exit stream. The results show how the cool flame is propagated through the system of tanks after which all the tanks reach a steady state temperature. The choice of exit stream from each the series of tanks can be considered to be a distance along the equivalent PFR. As such, the unsteady TIS model can in theory be used to model

an unsteady state PFR reactor, which in fact alludes to the overall objective of this thesis, namely the compartmentalisation of a complex geometry into a series of simpler regions.

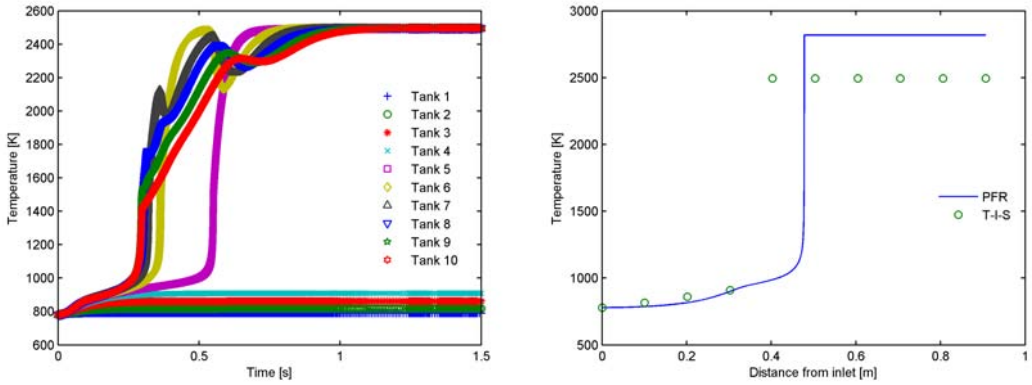


**Figure 9.12:** Temperature comparison between the PFR and a TIS model. Molar composition: $iC_8H_{18}/O_2/N_2 = 1/12.5/47$. Initial conditions: $P_0 = 8.85$ bar; $T_0 = 780$ K; Volume per tank = 5 $m^3$; Volumetric flow rate to each tank= $50\frac{m^3}{s}$

Figure 9.12 shows the temperature in the TIS and PFR models. The results show the PFR temperature prediction is 100 K higher than the TIS model. This may be due to the assumption of constant pressure in the PFR model. The PFR could be approximated by many smaller tanks but the system of equations that govern to TIS becomes numerically unstable at small volumes and high flow rates.

## 9.4 Conclusion

The reduced kinetic model has been successfully validated against experimental data using the batch reactor model. The fictitious components in PFR and CSTR models have also been validated against a full kinetic mechanism. Now that the idealised models are giving the correct trends they can be trusted in developing the greater CRN models.

# Chapter 10

# Combustion Dynamics

The dynamics of combustion provides a deeper insight into the non-linearity of the kinetic expressions and how the kinetic pathways, high temperature and low temperature, compete with each other. In order to investigate the dynamics of combustion, simulation studies were conducted on batch reactor models. This allows for elimination of the complicating fluid flow influence on the kinetics. A vector field that shows the systems trajectory towards the steady state is used to investigate the high temperature to low temperature transition and how the transition is influenced by temperature.



## 10.1 Vector Field Construction

The construction of a generic vector field for the dynamic analysis is explained in this section. There are 8 variables in the system and is given as follows:

1. $C_f$ - Concentration of Fuel
2. $C_X$ - Concentration of X-Intermediate
3. $C_{O_2}$ - Concentration of Oxygen
4. $C_I$ - Concentration of I-Intermediate
5. $C_Y$ - Concentration of Y-Intermediate
6. $C_P$ - Concentration of Product
7. $C_{N_2}$ - Concentration of Nitrogen
8. $T$ - Temperature

It is not feasible to investigate this 8D-space for dynamic features. Thus, the system is investigated using sectional 2D planes where the concentrations of the other intermediates not in the plane are taken at typical average values to ease the visualisation. The vector

components $(x, y)$ at a particular point in the 2D plane is given by the system of equations for the batch model. For the species concentration, the components are given by Equation 10.1

$$\frac{\partial C_i}{\partial t} = r_{net,i} \tag{10.1}$$

where the species net rate is given by $r_{net}$. The system reaches a steady state when $\frac{\partial C_i}{\partial t} = 0$ for both components in the plane. If the variable in the plane is temperature, Equation 10.2 is used to calculate the corresponding vector component.

$$\frac{\partial T}{\partial t} = \frac{-\sum_{i=1}^{n} H_i r_i + TR_{gas} \sum_{i=1}^{n} \frac{\partial C_i}{\partial t}}{-\sum_{i=1}^{n} C_i R_{gas} + \sum_{i=1}^{n} C_i Cp_i} \tag{10.2}$$

A constant heat capacity given in Schrieber et al. (1994) is used for the dynamics study. In this study, only the concentration planes are investigated as a function of temperature since the kinetics of combustion has a larger temperature feed back as opposed to chemical feedback (Griffiths, 1994).

## 10.2 Dynamic Analysis

Before the dynamic vector field is investigated, an initial investigation into the dynamics of the system is done by tracking how the system changes in relation to the steady state. Figure 10.1 shows the species concentration profiles and how the system position changes in relation to the steady state of the system.

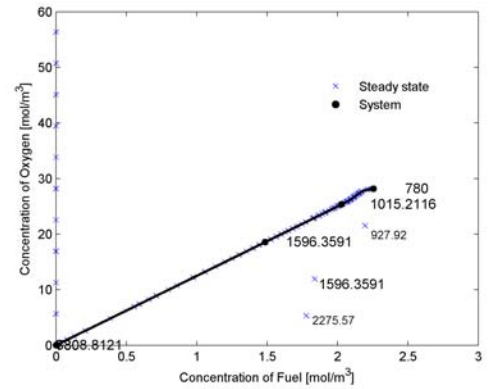


**(a)** Fuel and Oxygen

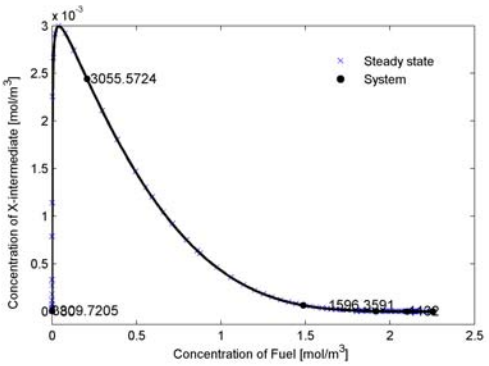


**(b)** Fuel and X-intermediate

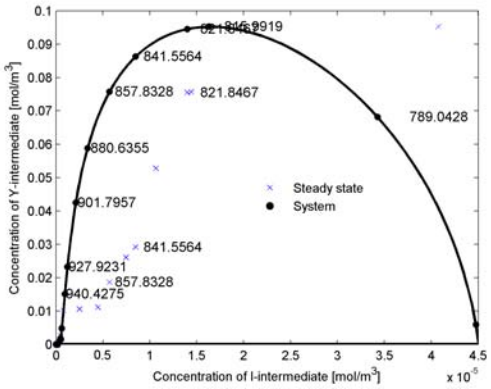


**(c)** Y-intermediate and I-intermediate

**Figure 10.1:** Current system state and steady-state state profiles as a function of temperature. The system position is indicated by the ◯. The steady state position calculated from the dynamics is indicated by ✕.



For the fuel and oxygen relation (see Figure 10.1a), and the fuel and X-intermediate relation (see Figure 10.1b), the current system's state is the same as the steady state of the system when the combustion event is occurring. However, Figure 10.1a shows that there are temperatures at which the current systems state and the steady state position are not the same. Both the fuel and oxygen concentrations at these temperatures are not the same as the steady state position. This could be a result of the low temperature pathway and high temperature pathway switching over in this temperature region.

Figure 10.1c shows the same trend in the Y-intermediate and I-intermediate plane. However, I-intermediate is at the correct steady state position but the Y-intermediate has deviated. The Y-intermediate steady state concentration is always lower that the systems current concentration since the system is not allowed to reach equilibrium and maintain the steady state concentration.

A more detailed look at the vector field of the high temperature X-intermediate and the free radical (I-intermediate) plane shows some dynamic features.

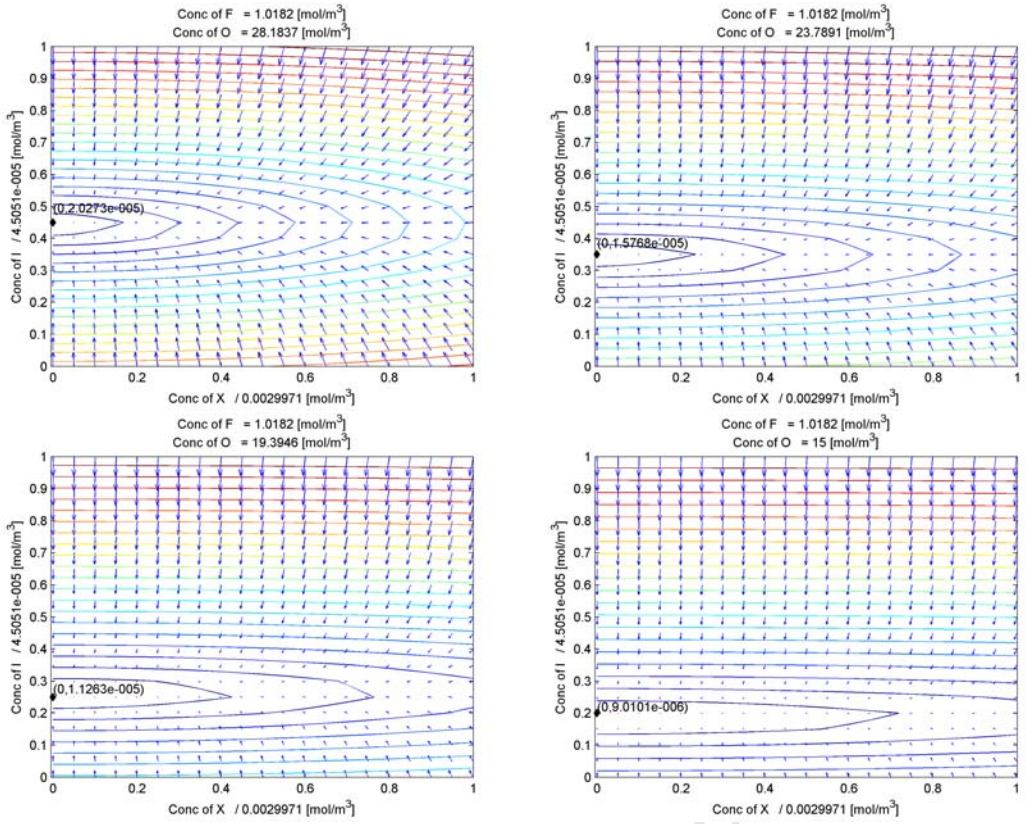


**Figure 10.2:** I-intermediate and X-intermediate dynamics as a function of fuel and oxygen concentration. The data point indicates the steady state position of the system. The colour of the contours indicate the magnitude of the vector with the direction indicated by the arrow.

The 2D domain given in Figure 10.2 is described to as the dynamic vector field. It maps the trajectory of the system towards the steady state. Every position in the domain consists of a direction and magnitude. The colour of the contours indicate the magnitude of the vector with the direction indicated by the vector arrow. The vectors may indicate that they converge to a particular point. This point is refer ed to as the attractor point. This attractor point in the vector field is the steady state at the given fuel and oxygen concentrations.

The high temperature and low temperature intermediate species can be freely formed and consumed such that any point in the vector can be identified as a starting position for experimental evaluations. As the fuel and/or oxygen is consumed, the steady state point begins to tend towards the origin, but note this is a trivial steady state at which the reaction rate drops to zero as a consequence of the concentrations tending to zero. There are always residual intermediates present due to the assumption of average values for the other species not in the plane. The shape of the vector field does not change but is slightly shifted giving an indication that the kinetic dependence on concentration is minimal as compared to temperature. Only one steady state position is observed in the vector field which is a trivial steady state. This indicates that no equilibrium exists between the high

temperature (X-intermediate) and low temperature intermediate (I-intermediate).

The vector field of the fuel and oxygen plane also shows some dynamic features.

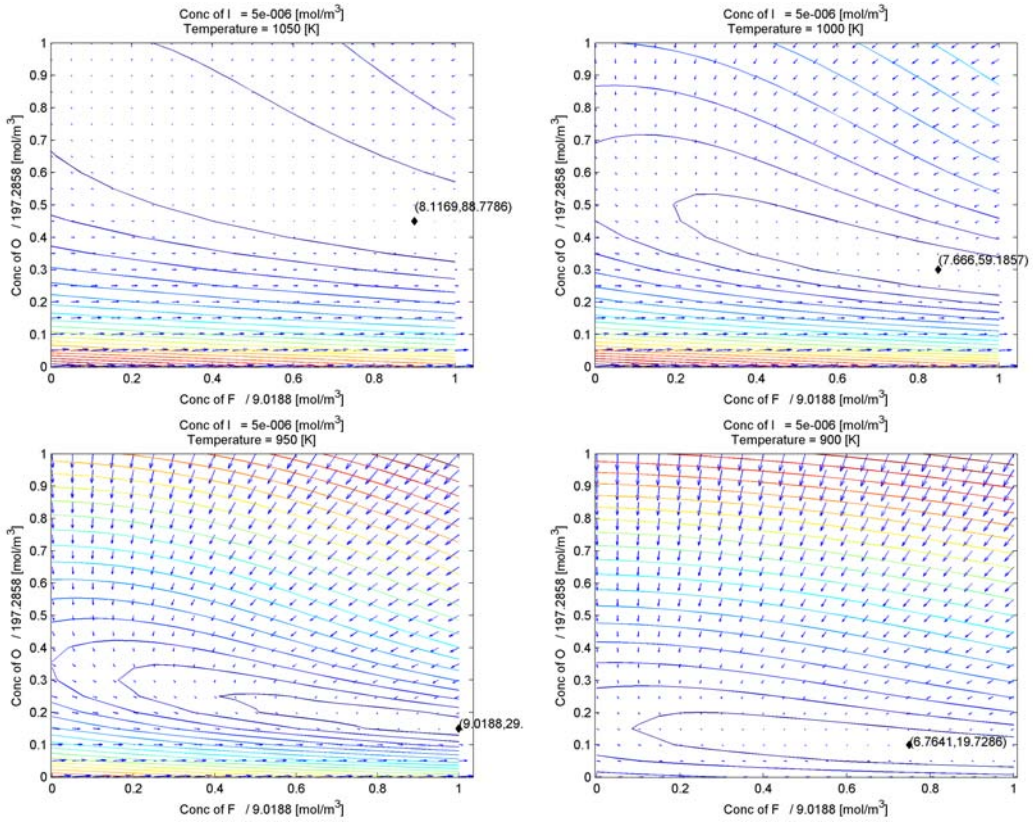


**Figure 10.3:** Fuel and Oxygen dynamics as a function of temperature and intermediate species concentration. The data point indicates the steady state position of the system. The colour of the contours indicate the magnitude of the vector with the direction indicated by the arrow.

The attractor point at coordinates $(8.12, 88.77)$ in the vector field (Figure 10.3) is the stable steady state at the given intermediate and temperature concentrations. Fuel and oxygen can not be freely formed but only consumed, so any concentration above the steady state point can be identified as a starting position for experimental evaluations. As the temperature is increased, the shape of the entire dynamic plane changes due to the strong temperature dependence of the kinetics. Again only one steady state is observed. The position of the steady state also changes as the temperature is increased.

## 10.3 Conclusion

The dynamics of combustion have been investigated. The results showed a region in which initial oxygen and fuel concentrations can be selected for experimental purposes. The dynamics did not reveal a clear distinction between the low temperature and high temperature kinetics. This may be due to the complex (8D space) interaction between the

kinetic pathways and the high non-linearity of the kinetic expressions. The results also confirmed that the kinetics of combustion has a larger temperature feed back as opposed to chemical feedback (Griffiths, 1994). This temperature feed back has implications on the CRN since the CRN is highly dependent on initial temperature.

# Chapter 11

# Inlet Velocity Effects

Computational Fluid Dynamics (CFD) simulations required to generate vector fields for CRN development have been performed. The geometry, boundary conditions and particular models adopted for turbulence and combustion chemistry are described in Chapter 7. For the current study, two geometries were investigated and a CRN was developed as was discussed in Chapter 8. The CRN will later be correlated to the input velocity in an attempt to make the CRN more predictive over a wide range of input conditions. In this section, the effect of inlet velocity on CFD field is investigated to ascertain whether the proposed CRN structure given in Chapter 8 needs to be updated as a function of velocity.

## 11.1 Double Inlet Reactor

Chapter 7 provides details regarding the CFD simulation of the double inlet reactor with the proposed CRN given in Chapter 8. The double inlet reactor was simulated at various inlet velocities to asses the effect of velocity on the network design. Figure 11.1 and Figure 11.2 shows two such inlet conditions.

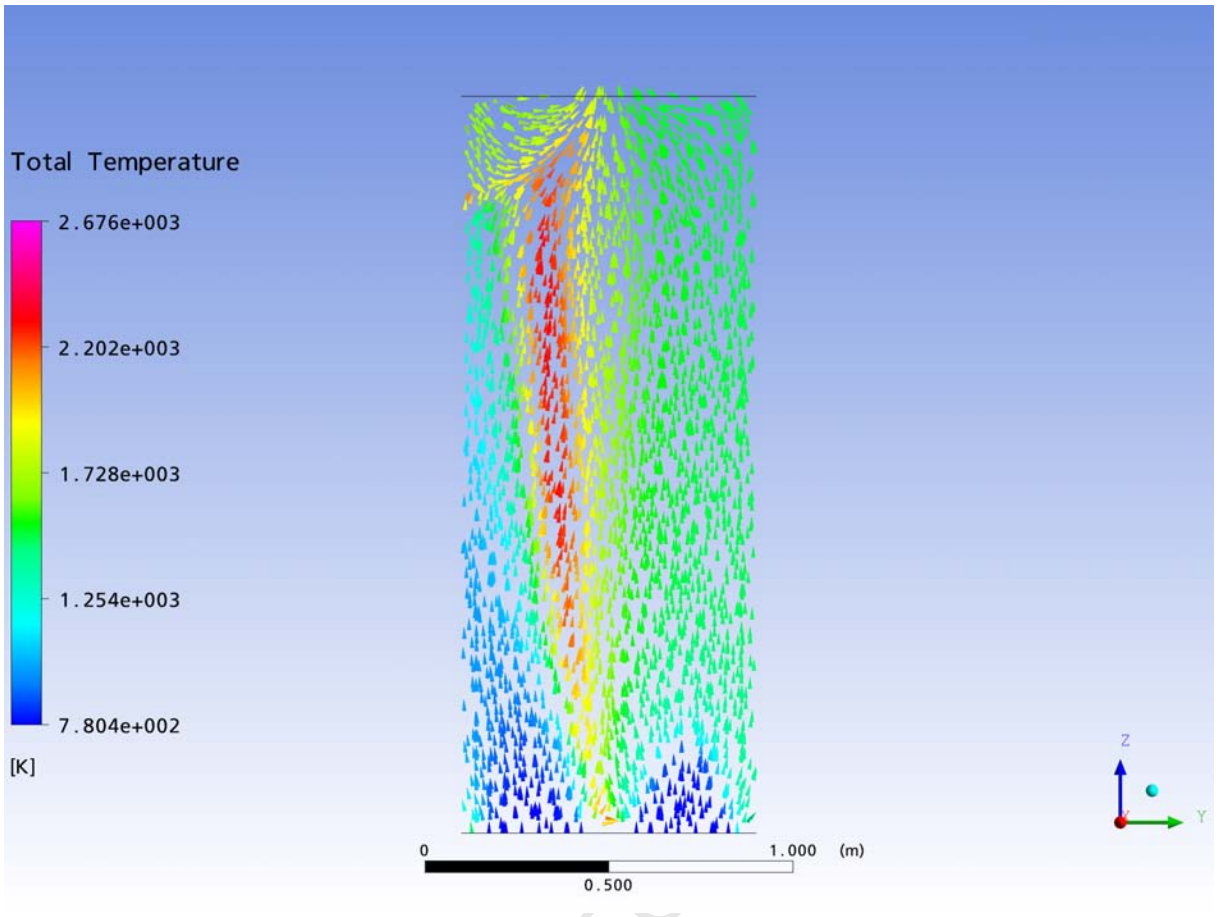


**Figure 11.1:** Velocity vector field at the $x = 0$ plane. The vectors are coloured by temperature. Inlet velocity = 50 m/s

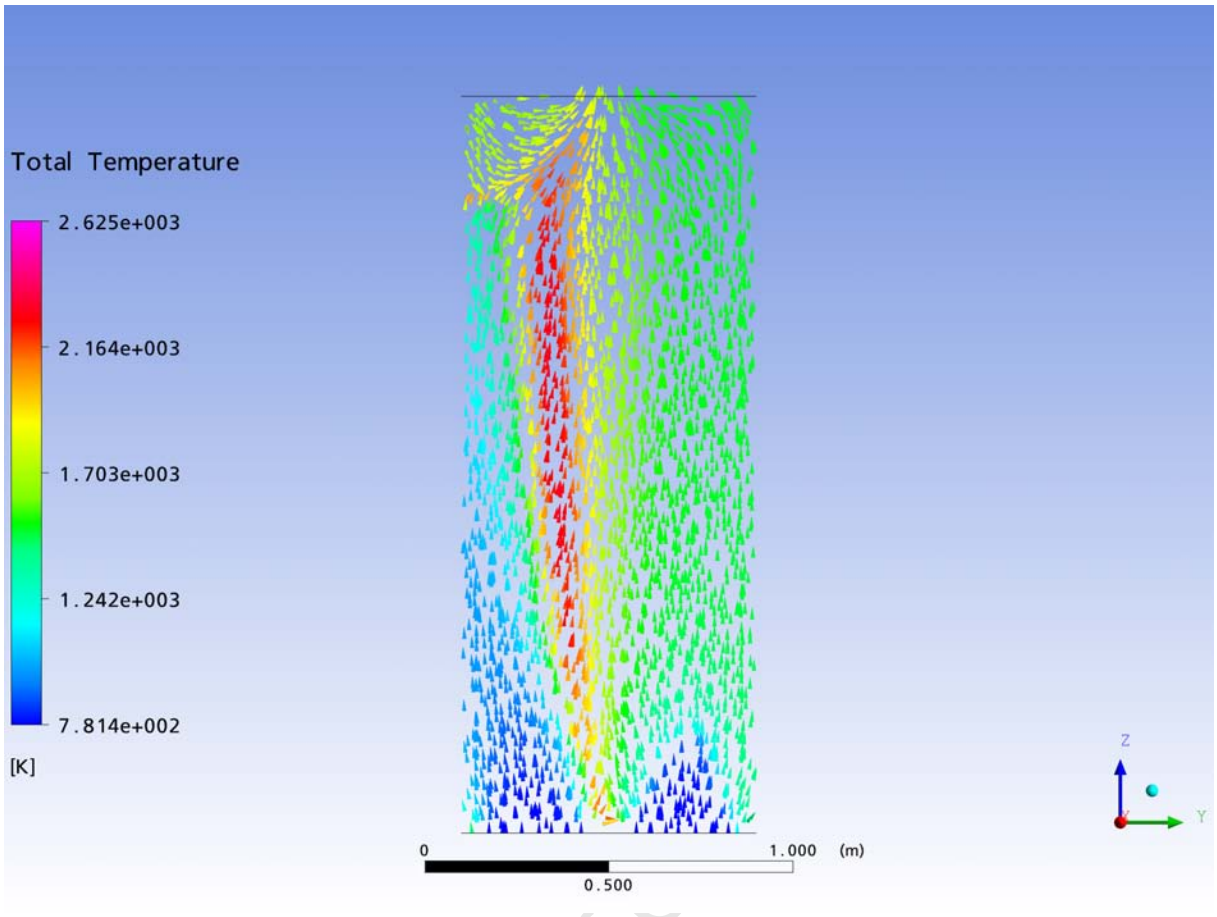


**Figure 11.2:** Velocity vector field at the $x = 0$ plane. The vectors are coloured by temperature. Inlet velocity = 100 m/s

It can be seen that as the inlet velocity is increased, the vector fields do not change and the flame is propagated in the same position at different input velocities. Since the vector fields do not change, the classification of zone (PFR or CSTR) and the structure of the network is unchanged. This also implies that the split flow fractions and volume fractions chosen for the network design does not change as the inlet velocity is varied. Since the network parameters and volume fractions are not affected by the input velocity, no correlation is investigated for this geometry.

## 11.2 Furnace

Details regarding the furnace CFD simulations and operation are given in Chapter 7 with the developed CRN given in Chapter 8. The furnace was also simulated at various inlet velocities to asses the effect of velocity on the network design. At a low inlet velocity, Figure 11.3 and Figure 11.4, the recirculation zone is centrally located with a large degree of circulation occurring to the left of the inlet. The flame propagation can clearly be seen in Figure 11.4 when looking along the inlet plane ($x = 4.24$) including a dead zone near the inlet.

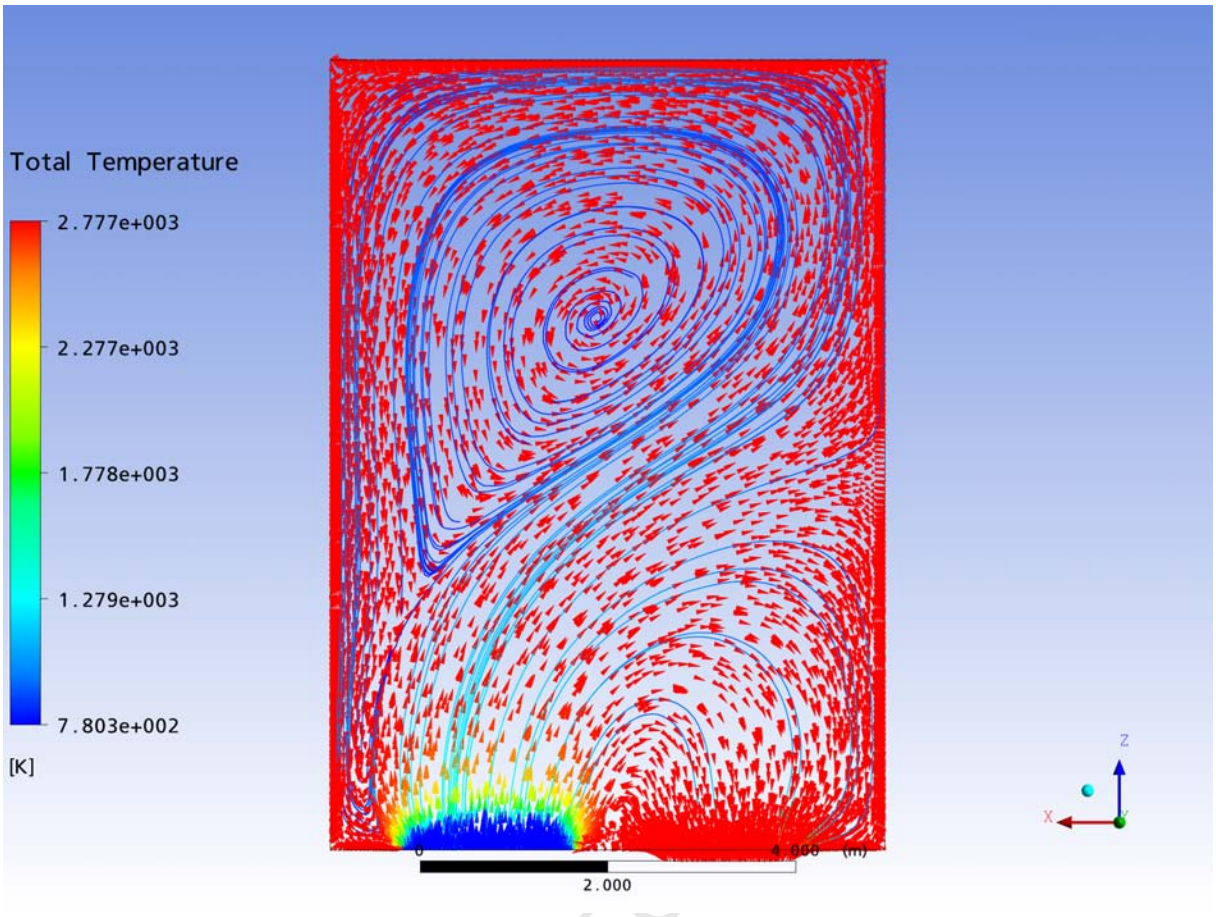


**Figure 11.3:** Velocity vector field at the $y = 1.15$ plane. The vectors are coloured by temperature. Inlet velocity = 26 m/s

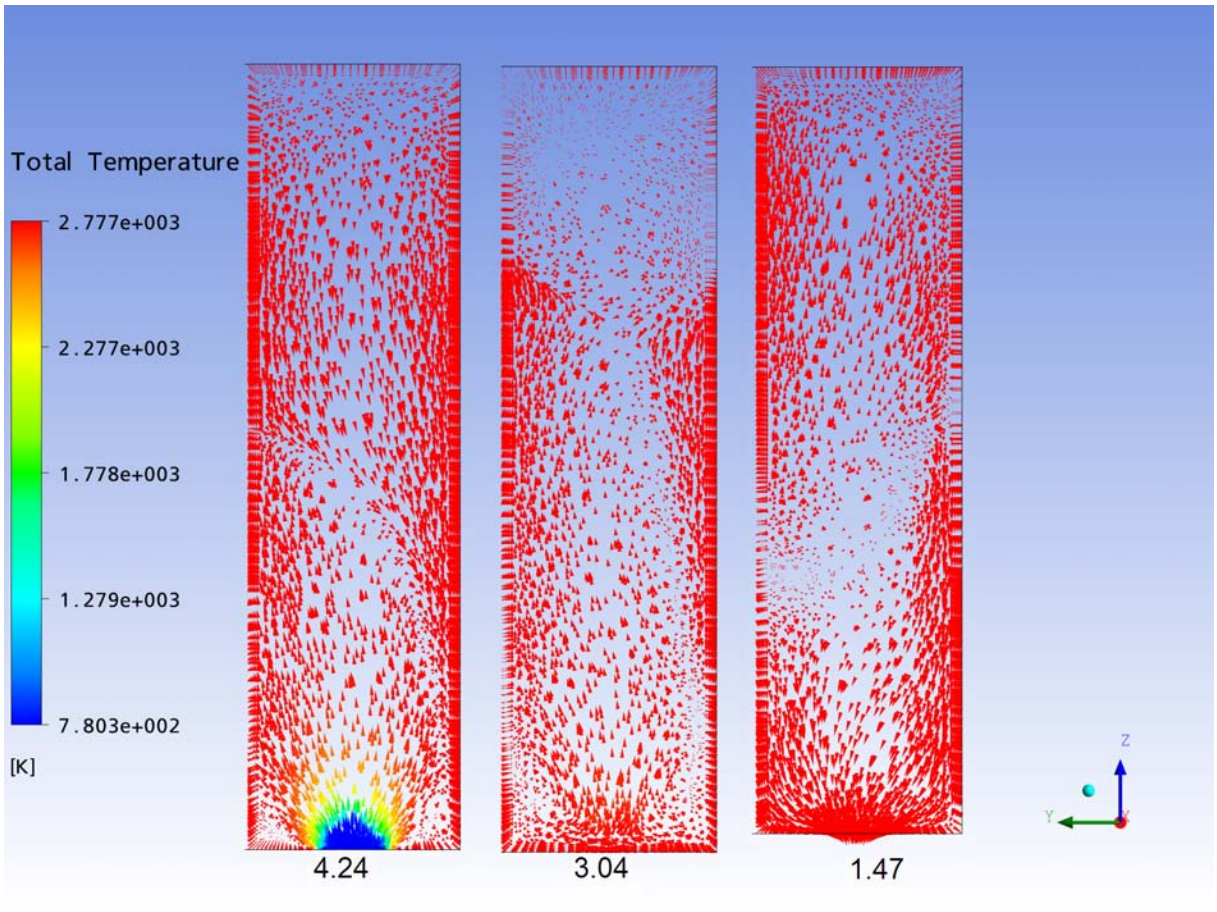


**Figure 11.4:** Velocity vector field at the various $x$ positions. The vectors are coloured by temperature. Vector fields from left to right: Inlet, Centre, Outlet . Inlet velocity = 26 m/s

As the velocity is increased (see Figure 11.5 and Figure 11.6), the recirculation zone shifts to the left. The small circulation occurring to the left of the inlet is minimised as well as the dead zones (Figure 11.6).

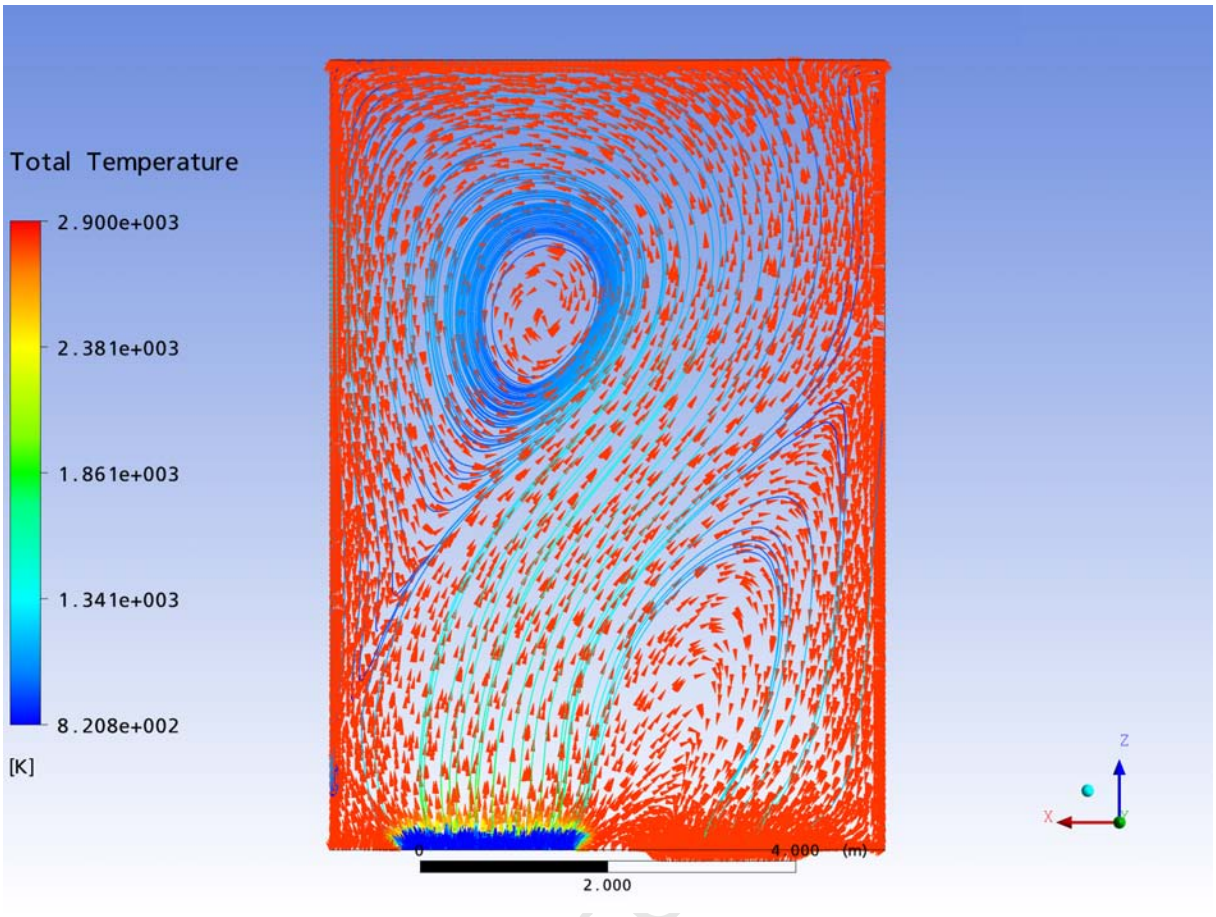


**Figure 11.5:** Velocity vector field at the $y = 1.15$ plane. The vectors are coloured by temperature. Inlet velocity = 326 m/s

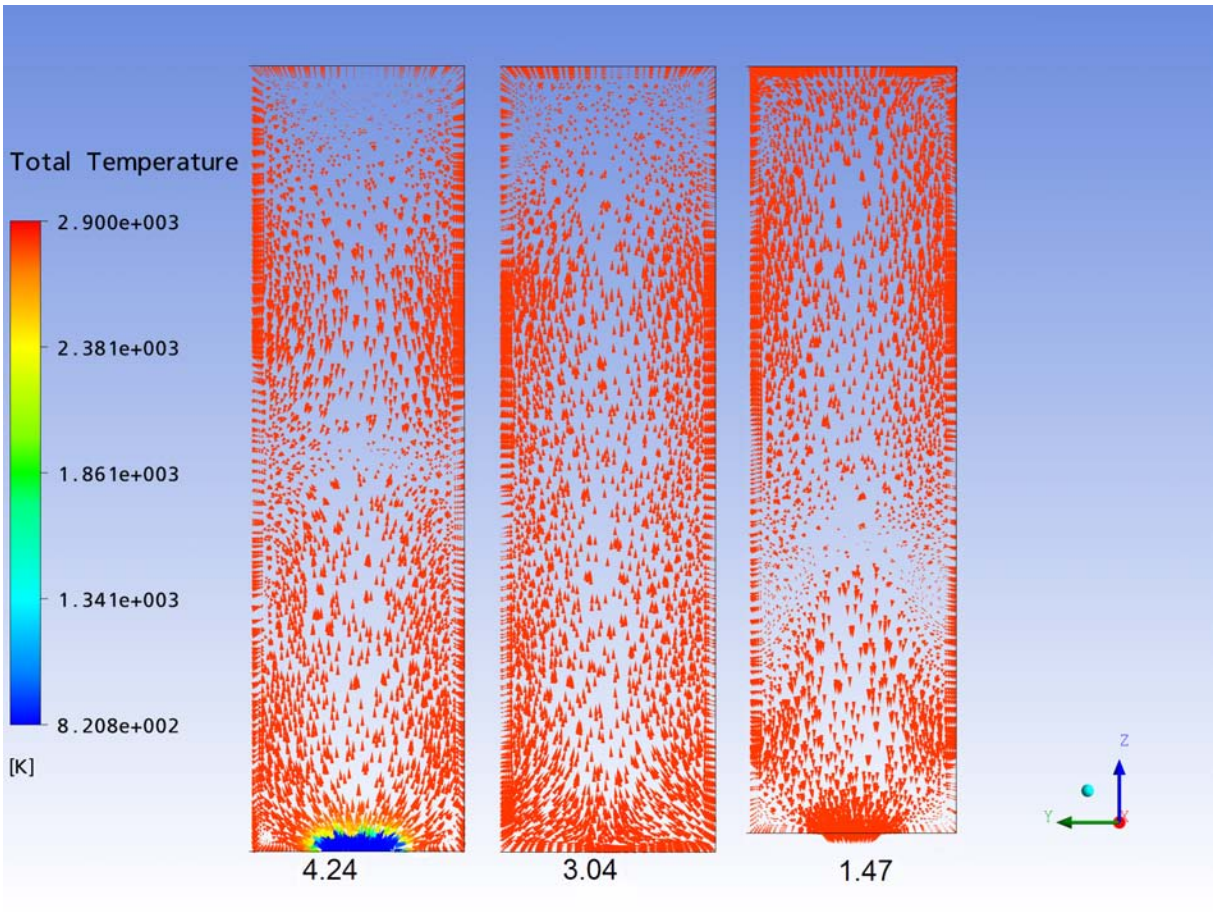


**Figure 11.6:** Velocity vector field at the various $x$ positions. The vectors are coloured by temperature. Vector fields from left to right: Inlet, Centre, Outlet . Inlet velocity = 326 m/s

It is evident that as the velocity increases, the flame is propagated more uniformly outward in the 3D space (Figure 11.4 and Figure 11.6). The flow is still not ideally plug flow since there exist a dispersion component to the flow in the ZX plane (Figure 11.3 and Figure 11.5). The results also show that the volume ratios of the three zones defined in Chapter 8 remains unchanged as the inlet velocity is increased. However, the behaviour of zone 1 (Z1) becomes more plug flow at higher inlet velocities. The volume ratios of the zones do not change but the flow fractions between them do. These flow splits will be correlated to the input velocity in an attempt to make the CRN more predictive as compared to current CRN models.

## 11.3 Conclusion

In the current study, two geometries were investigated and a CRN was developed. The effect of inlet velocity on the CFD field is investigated to ascertain whether the proposed CRN structure needs to be updated. It was found that for the simple geometry (Double Inlet reactor) the CRN structure and flow splits parameters of the network are not af-

fected by the input velocity. Thus, correlation of the CRN to the inlet velocity was not investigated.

For the advanced geometry (Furnace), the CRN structure was not affected by the inlet velocity but the flow split parameters of the network are affected. The flow split parameters can now be correlated to the inlet velocity to further the predictive capabilities of the CRN.

# Part IV

# Model Application

# Chapter 12

# Model Validation

In the preceding chapters, a kinetic model and thermodynamic properties of the pseudo species were proposed and successfully validated. In the present chapter, the reduced kinetic model and thermodynamic properties are now applied in the context of a Rapid Compression Machine (RCM) and assessed against experimental ignition time delay data for the purpose of validation.



## 12.1 Experimental Equipment

The experimental data (pressure trace curves) is obtained from the Sasol Advanced Fuels Lab (SAFL) based at the University of Cape Town. The experimental equipment used in this study is shown in Figure 12.1 with the dimensions given in Table 12.1. The operation of the RCM has already been discussed in Chapter 2.

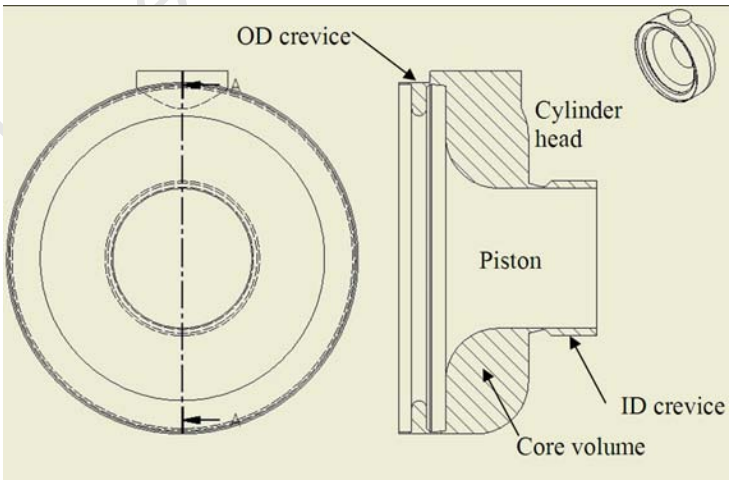


**Figure 12.1:** Experimental configuration of the rapid compression machine

| Parameter | Dimension |
|---|---|
| OD: | 50.02 mm |
| ID: | 19.85 mm |
| Effective bore: | 45.9 mm |
| Max clearance height: | 11.8 mm |
| Final volume: | 21.11 ml |
| Outer crevice: | 1.56 ml |
| Inner crevice: | 0.65 ml |
| Tot crevice volume: | 2.16 ml |

**Table 12.1:** Dimensions of the rapid compression machine

In the experimental plan, the systems initial pressure is constant and considered to be atmospheric (101.3 kPa). The two parameters varied in the experimental program are initial temperature and (final) compression ratio. The initial temperature is varied from $25^oC$ to $200^oC$. The compression ratio is defined by Equation 12.1

$$CR = \frac{V_i}{V_f} = \frac{V_f + V_s}{V_f} \tag{12.1}$$

where $V_i$ is the initial volume. The compression ratio is changed by varying the stroke distance since the final volume remains constant for each experiment; in other words, the initial volume is varied. The experimental data presented in this study is limited to stoichiometric mixtures of iso-octane and air.

The velocity history of the piston is obtained using the output from a oscilloscope. The period (peak-to-peak) between oscillations denotes the time taken for the piston to travel 2 mm. As the period decreases, the velocity increases. The piston is not fixed in position after the compression thus the maximum pressure obtained after combustion can not be accurately known. The experimental programme is outlined by way of the range of initial conditions (understood as the experimental inputs) with the resulting ignition delay times (experimental outputs) shown in Figure 12.2 and 12.3. As discussed in Chapter 2, the resulting ignition delay times are obtained using the pressure trace of the RCM.

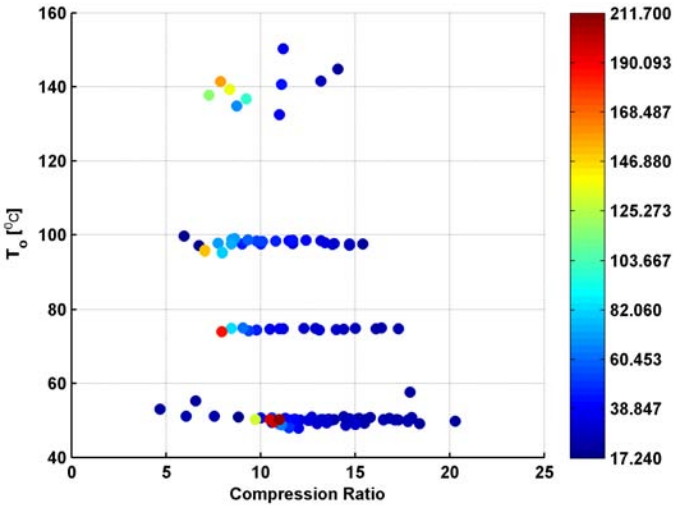


**Figure 12.2:** Data Field of initial conditions sampled by the rapid compression machine

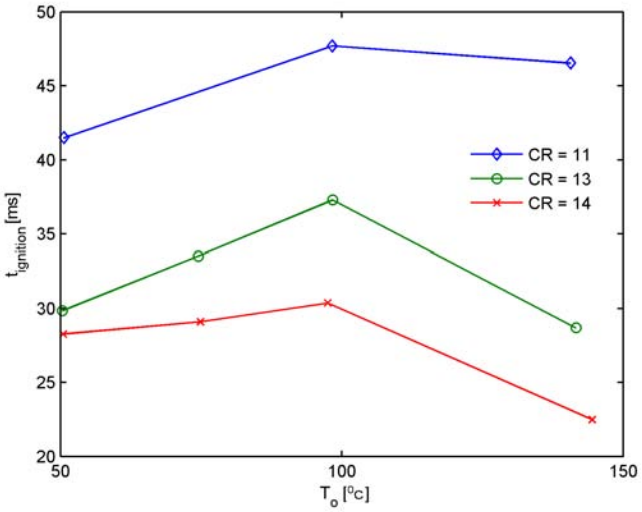


**Figure 12.3:** Experimental ignition time delay

The experimental error associated with the ignition time delay was not quantified due to the availability of repeated experimental conditions. Figure 12.3 shows that as the initial temperature increases, there is an increase in the ignition delay time followed by a decrease. This is characteristic of the negative temperature coefficient (NTC) region already discussed in Chapter 4 (Tanaka et al., 2003, Kirk-Othmer, 2001, Griffiths, 1994). The ignition delay decreases with an increase in the compression ratio which is expected since there is a the pressure feedback built into the kinetics. The concentration of the fuel and oxygen are higher at elevated pressures resulting in a decrease in the ignition delay. Since the experimental ignition time delay trends conform to what is expected, a RCM model based on reduced kinetics is capable of predicting the same results.

## 12.2 Proposed Model

The RCM model equations are derived based on the schematic system shown in Figure 12.4. The core gas region is assumed to be well mixed with heat loss occurring through the thermal boundary layer. The thermal boundary layer is assumed to be constant in thickness.

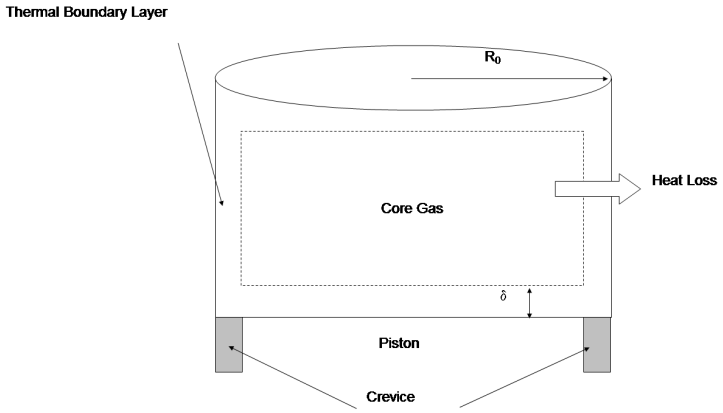


**Figure 12.4:** Model schematic for the RCM

### 12.2.1 System of Equations

In developing the material balance, we note that there are no flows across the system boundaries ($F_{in,i} = F_{out,i} = 0$), thus the mole balance for a species at any time within the RCM is given by Equation 12.2.

$$\frac{\partial N_i}{\partial t} = r_{net,i} V \tag{12.2}$$

The reactor is non isothermal but the energy balance must have the capacity for time varying system pressure and volume. The general energy balance for the system is given by Equation 12.3

$$\dot{Q} + \sum_{i=1}^{n} F_{in,i} H_{in,i} - \sum_{i=1}^{n} F_{out,i} H_{out,i} = \sum_{i=1}^{n} N_i \frac{\partial H_i}{\partial t} + \sum_{i=1}^{n} H_i \frac{\partial N_i}{\partial t} - V \frac{\partial P}{\partial t} - P \frac{\partial V}{\partial t} \tag{12.3}$$

where the extra term , $\frac{\partial V}{\partial t}$, accounts for the change in volume in the system, $H_i$ is the enthalpy of the $i^{th}$ species, $F_{in,i}, F_{out,i}$ is the flow of the $i^{th}$ species into or out of the reactor respectively and $\dot{Q}$ is the external energy contribution. Heat loss due to conduction and convection is modelled by Equation 12.4

$$\dot{Q} = UA(T_{core} - T_{\infty}) \tag{12.4}$$

where $U$ is the overall heat transfer coefficient, $A$ is the cross sectional area of the piston, $T_{core}$ is the temperature of the core, $T_\infty$ is the temperature of the room. The overall heat transfer coefficient is assumed as the parameter to be fitted to the data minimising the MSE between the model and the experimental data. Since there is no flow across the system boundaries ($F_{in,i} = F_{out,i} = 0$), the energy balance is given by Equation 12.5

$$\dot{Q} = \sum_{i=1}^{n} N_i Cp_i \frac{\partial T}{\partial t} + \sum_{i=1}^{n} H_i r_{net,i} V - V\frac{\partial P}{\partial t} - P\frac{\partial V}{\partial t} \tag{12.5}$$

where $Cp_i$ is the heat capacity of the $i^{th}$ species. The change in pressure can be related to the change in volume and number of moles using the ideal gas equation. The resulting pressure change is given by Equation 12.6

$$\frac{\partial P}{\partial t} = TR_{gas}\sum_{i=1}^{n}\frac{\partial\left[\frac{N_i}{V}\right]}{\partial t} + R_{gas}\sum_{i=1}^{n} C_i\frac{\partial T}{\partial t} \tag{12.6}$$

where $R_{gas}$ is the ideal gas constant. Substitution of the ideal gas relation into the energy balance yields the PDE that governs the temperature changes within the system (Equation 12.7).

$$\frac{\partial T}{\partial t} = \frac{\dot{Q} - \sum_{i=1}^{n} H_i r_{net,i} V + R_{gas}T\sum_{i=1}^{n} r_{net,i} V + P\frac{\partial V}{\partial t}(1 - \frac{1}{R_{gas}T})}{\sum_{i=1}^{n} N_i Cp_i + \sum_{i=1}^{n} N_i R_{gas}} \tag{12.7}$$

The volume change of the system ($\frac{\partial V}{\partial t}$ in Equation 12.7) is calculated using the velocity profile of the piston given by Equation 12.8

$$\frac{\partial V}{\partial t} = -AV_z \tag{12.8}$$

where $A$ is the cross sectional area of the piston. The RCM model has been derived and can now be applied to reacting and non-reacting systems.

## 12.3 Comparison with Data

The model that has been developed is now compared to the experimental data. The overall heat transfer coefficient is used as the free parameter in the simulation to obtain the lowest MSE between the experimental data and the model. The RCM model is tested on a non-reactive air mixture to asses the potential shortfalls in the model. The reactive mixtures experimental data is then used to test the RCM model and inference can then be drawn with regards to the kinetic mechanism and thermodynamic properties of the pseudo species.

### 12.3.1 Non-reactive Mixture

The non-reactive fluid used in this experiment is air. The experimental data obtained needs to be smoothed since it has a large degree of noise. The data is subdivided into subdomains of smaller volume afterwhich the data in a particular subvolume is averaged. The subvolumes need to be large enough to smooth the data but should not be too large such that the essential features of the data are lost. The result of the averaging the data is shown in Figure 12.5. Figure 12.5 shows that the complexity of the data is reduced by an order of 10 but the key features of the pressure trace is still maintained.

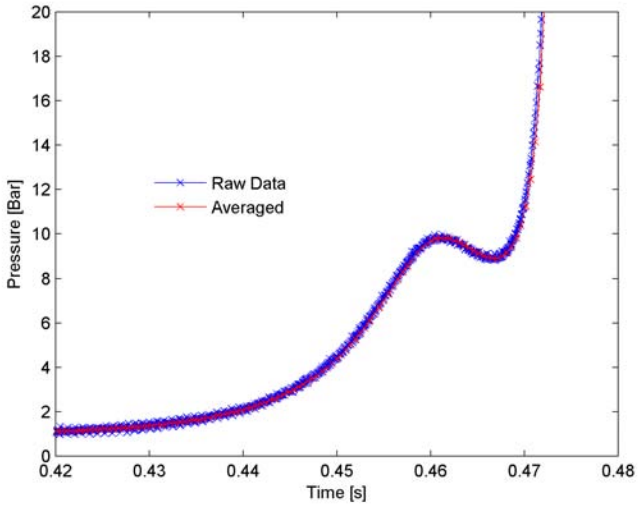


**Figure 12.5:** Smoothing of the RCM pressure data. Original resolution = 60000 data points. Smoothed resolution = 7919 data points. Non-reactive mixture. Molar composition: $O_2/N_2 = 21/79$, $T_0 = 293$ K, $CR = 11$.

The velocity profile of the piston, Figure 12.6, is used to obtain the volume change as the compression occurs. The true volume change within the RCM can be modelled with no assumptions being made as opposed to other studies (Mittal, 2006, Lee and Hochgreb, 1998).

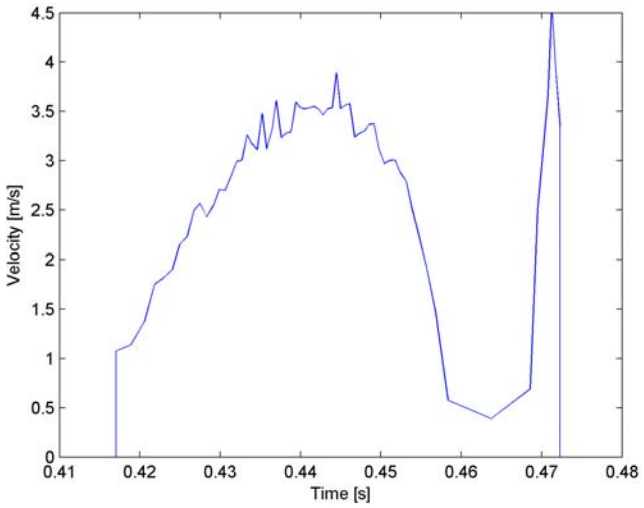


**Figure 12.6:** Piston velocity. Non-reactive mixture. Molar composition: $O_2/N_2 = 21/79$, $T_0 = 293$ K, $CR = 11$.

The RCM model can now be compared to the experimental data for a non-reacting system. The value of the heat transfer coefficient that results in the lowest MSE between the model and the data and giving the same experimental ignition time delay is given as $U = 382.7\frac{W}{K.m^2}$ . The results are shown in Figure 12.7.

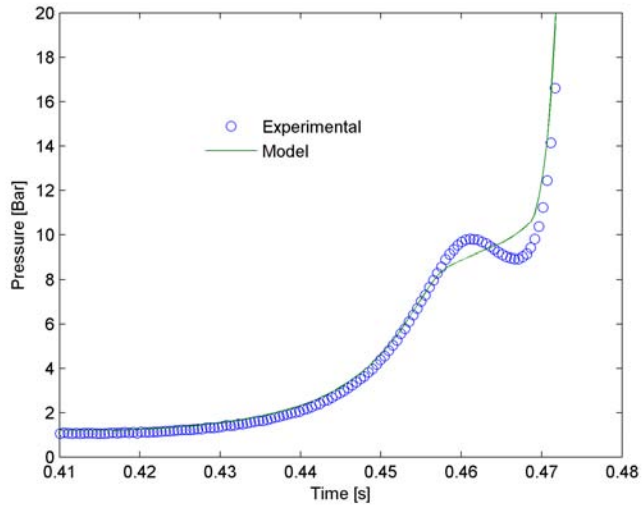


**Figure 12.7:** Model comparison. Non-reactive mixture. Molar composition: $O_2/N_2 = 21/79$, $T_0 = 293$ K, $CR = 11$.

The pressure trace predicted by the model has a good fit to the experimental data. The model does however fail to predict the pressure loss which is due to the heat transfer from the RCM. The model prediction improves once the pressure starts to increase again. This brings into question the proposed form of the heat transfer model but since the offset between the model and the data in this region is minor, it is deemed acceptable.

### 12.3.2 Reactive Mixture

The pressure trace predicted by the model for the non-reacting system showed a good fit to the experimental data; the model could then be tested for chemically reacting mixture of iso-octane. To test the chemically reactive RCM model, a set of initial conditions are chosen from Figure 12.2 where after the RCM model is simulated.

The value of the heat transfer coefficient that results in the lowest MSE between the model and the data for the chemically reactive case and giving the same experimental ignition time delay is given as $U = 54.5\frac{W}{K.m^2}$. The result for the heat transfer coefficient differs from the non-reactive case ($U = 382.7\frac{W}{K.m^2}$) mainly due to the number and vastly different chemical species present in the reactive case and the different temperature range being operated in. Both these factors affect the internal heat transfer coefficient. The results of the pressure trace for the model and experimental data are shown in Figure 12.8.

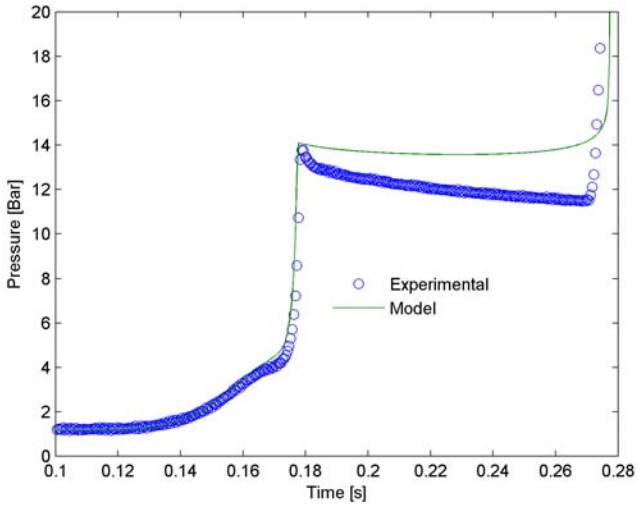


**Figure 12.8:** Chemically reactive mixture. Molar composition: $iC_8H_{18}/O_2/N_2 = 1/12.5/47$, $T_0 = 410$ K, $CR = 7.26$

Figure 12.8 shows that the model accurately predicts the pressure rise during the compression of the RCM and the experimental ignition time delay. The model again fails to predict the loss in pressure due to the heat transfer from the RCM to the surroundings. The heat loss in the reactive case is far greater than the non-reactive case since there is a larger temperature gradient. The heat transfer model can be proposed as a combination of conduction, convection and radiation components to further improve its prediction instead of the current proposal of an overall heat transfer coefficient model. Another contributor to the deviation in the RCM model is the low initial temperature of the experiment. The reduced kinetic model struggles to accurately predict the entire pressure trace at such a low initial temperature as was discussed in Chapter 9.1.

For the purpose of this study, the model predicts similar pressure trends and the same experimental ignition time delay, thus it is deemed acceptable.

## 12.4 Conclusion

The reduced kinetic model and thermodynamic properties were applied to the simulation of a RCM for a non-reactive and a chemically reactive experimental conditions. The RCM model for both cases showed a good fit with the experimental data. The chemically reactive ignition time delay was accurately predicted by the RCM model. However, the model does fail to accurately predict the heat loss in both case. The heat loss term can be improved by considering each type of heat loss (conduction, convection, radiation) instead of an overall heat loss term. Since the model does show good fits outside this region, the reduced kinetic model and the thermodynamic properties of the pseudo species can be considered as validated.

# Chapter 13

# Compartment Implementation

In the preceding chapters, a preliminary CRN structure has been proposed for the two geometries under investigation (Chapter 8). In addition, an investigation into the influence of inlet velocity on the simple geometry's (Double Inlet reactor) CFD field revealed that the CRN structure and flow splits parameters of the network is not influenced by the inlet velocity but for the advanced geometry (Furnace), the CRN the flow split parameters of the network are influenced by the inlet velocity (Chapter 11). In this section, the network parameters for the Double Inlet reactor are proposed and the results compared to that of the CFD simulation. The network parameters for the Furnace are correlated to the inlet velocity and the predictive nature of the CRN is compared with results of the CFD simulation.



## 13.1 Double Inlet Reactor

Chapter 7 provides details regarding the CFD simulation of the double inlet reactor with the proposed CRN given in Chapter 8. For ease of reference, the CRN developed is given in Figure 13.1.

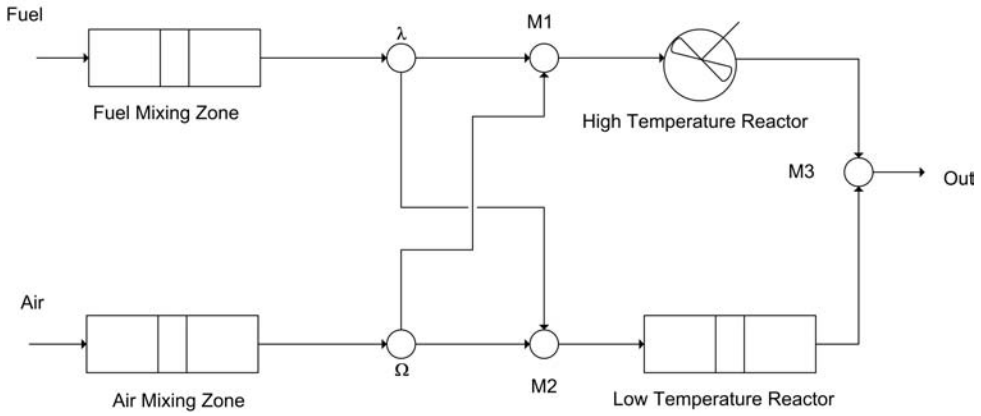


**Figure 13.1:** Proposed network based on the double inlet reactor flow fields

The network requires the following hydrodynamic parameters be identified before it can be solved:

1. $\lambda$ - Fraction of incoming fuel stream that is split to the low temperature reactor
2. $\Omega$ - Fraction of incoming air stream that is split to the low temperature reactor

Key points in the domain are identified (e.g. concentration and temperature at the reactor exit point) and are used for comparison purposes. The critical points are shown in Figure 8.3 with the results of the comparison given in Figure 13.2. The split fractions that result in the lowest error between the network prediction and the CFD simulation is given as follows:

- $\lambda = 0.9044$
- $\Omega = 0.1387$

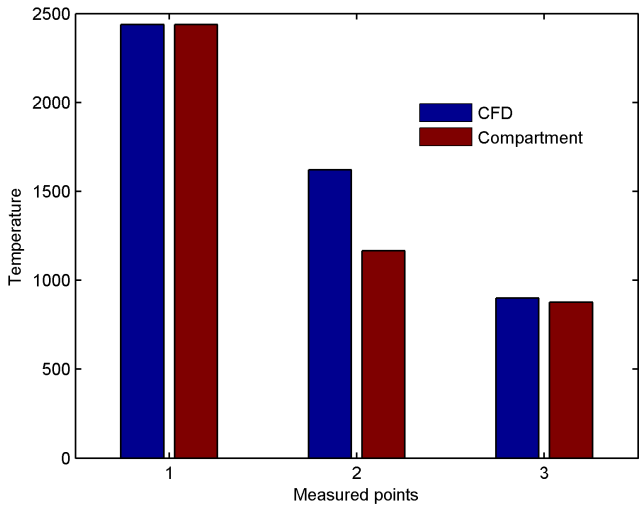


**Figure 13.2:** Comparison between the compartment model and the CFD at the measured points in the domain.

Figure 13.2 shows the network model predicts the same maximum temperature of the flame as well as the low temperature reactor exit temperature. The network model under predicts the exit temperature by 400 K when compared to the CFD. The offset between the CRN and CFD is a result of the turbulent mixing being considered in the CFD where as the network model does not account for this factor. The network model is solved within 20 CPU seconds compared to the CFD simulation of 2 CPU hours. Since the CRN is within good agreement with the CFD, the CRN can be used as a quick predictive tool for equipment optimisation purposes.

## 13.2 Furnace

A detailed description of the furnace CFD simulations and operation are given in Chapter 7 with the developed CRN given in Chapter 8. The proposed CRN developed in Chapter 8 is given in Figure 13.3.

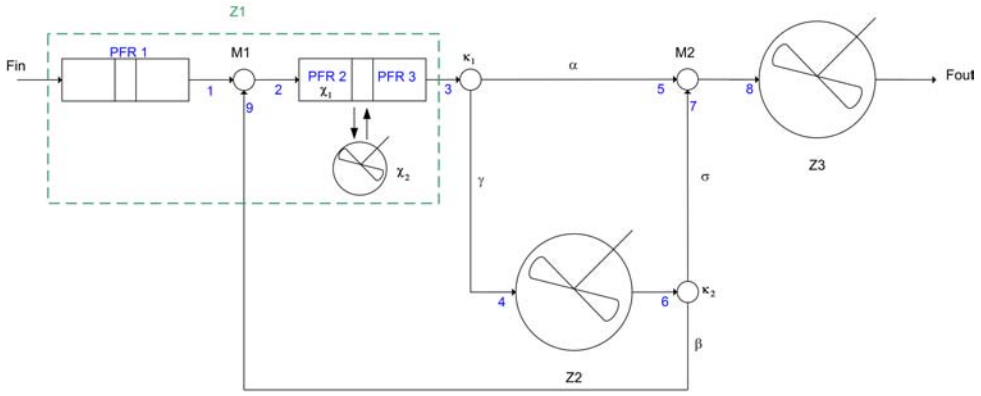


**Figure 13.3:** Proposed network based on the furnace flow fields

The furnace network requires certain parameters to be specified before it can be solved. These are:

1. $\kappa_1$ - Fraction of incoming stream that is split to zone 2
2. $\kappa_2$ - Fraction of incoming stream that is split to zone 1
3. $\chi_1$- Fraction of Z1 that is dedicated to PFR 2
4. $\chi_2$- Fraction of PFR 2 that is back mixed

The CFD furnace simulation was conducted at the various inlet velocity conditions given in Table 7.2. The network parameters were regressed against the CFD results at inlet velocities given in Table 13.1. The MSE is then calculated across the entire inlet velocity range.

| Velocity | CFD | CRN |
|---|---|---|
| 26 | Regression point | |
| 50 | Comparison point | |
| 100 | Comparison point | |
| 126 | Regression point | |
| 160 | Comparison point | |
| 200 | Comparison point | |
| 250 | Comparison point | |
| 300 | Comparison point | |
| 326 | Regression point | |
| 350 | Comparison point | |

**Table 13.1:** Cross correlation data points between the CRN and CFD

The parameters of the network ($\kappa_1$ , $\kappa_2$, $\chi_1$ , $\chi_2$ ) were optimised to achieve the lowest MSE at three inlet velocities.

Temperature is a key variable in the system as was shown by the combustion dynamics, Chapter 10. The comparison between the CRN and CFD is chosen to be the intersection of the $y = 1.15$ and the $x = 4.24$ plane since most of the combustion effects are dominant in this region. The plane intersection stretches across zone 1 and zone 2 but the comparison is based on zone 1 (Z1 in Figure 8.10) temperature profile since the flame front only exists in this zone. This occurs since the all the fuel is reacted in zone 1.

Three inlet velocities were chosen (Table 13.1) to cross correlate the network parameters taking a total CPU time of 48 minutes to solve the parameters at each flow rate. The temperature profile of the CRN using the optimised parameters and the temperature profile of the CFD are given in Figure 13.4.

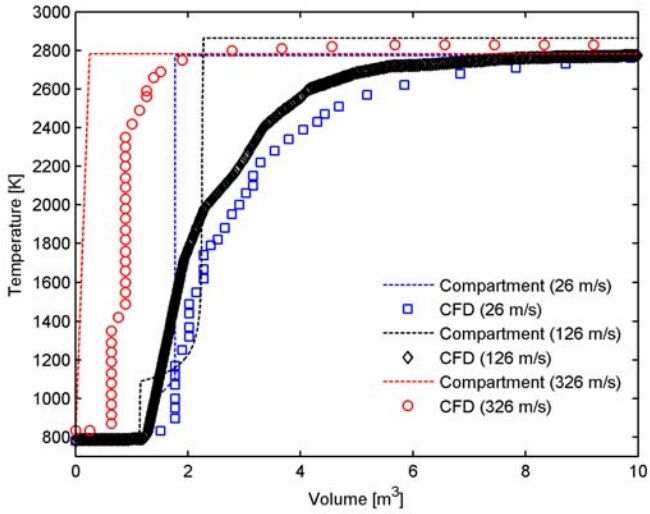


**Figure 13.4:** Temperature comparison between the compartment model and the CFD at the intersection of $y = 1.15$ and $x = 4.24$ plane in zone 1

Figure 13.4 shows that as the inlet velocity increases, the flame front exhibits more plug flow behaviour in zone 1. The model should therefore have a lower residual at higher flow rates since the flow in zone 1 is becoming more uniform, but this is not observed since the compartment model predicts the flame front at high inlet velocities (resulting in higher concentrations) will occur closer to the inlet point, causing the mixture to pre-ignite at higher flow rates. However, the final temperature predicted by the compartment model in all the zones correlates well to the CFD simulation.

The CRN parameters are now mathematically correlated using the parameters at the three input velocities. The optimised parameters are given in Figure 13.5 with the mathematical expression given in Table 13.2.

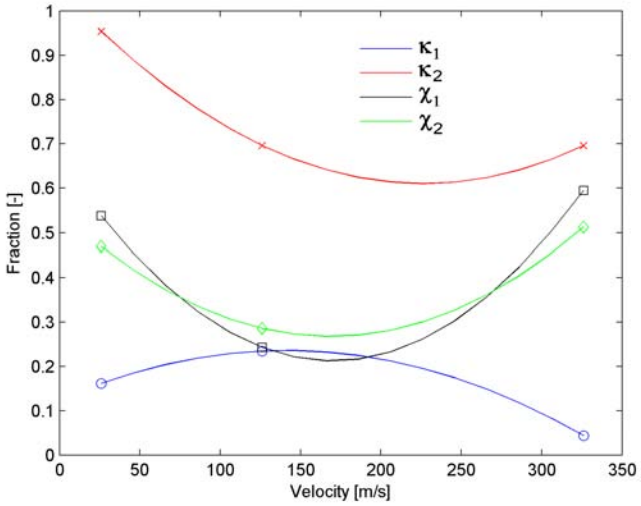


**Figure 13.5:** Polynomial fitting of the network data

| Coefficient | $a$ | $b$ | $c$ |
|---|---|---|---|
| $\kappa_1$ | $-5.61 \times 10^{-6}$ | 0.0016 | 0.124 |
| $\kappa_2$ | $8.55 \times 10^{-6}$ | $-0.0039$ | 1.04 |
| $\chi_1$ | $1.57 \times 10^{-6}$ | $-0.0053$ | 0.666 |
| $\chi_2$ | $9.91 \times 10^{-6}$ | $-0.0033$ | 0.549 |

$Parameter = a * VelocityIn^2 + b * VelocityIn + c$

**Table 13.2:** Mathematical expression of the network data



It must be noted that once the network parameters have been mathematically correlated, the network model can be used as a more predictive tool over a wide range of input conditions. This is a novel approach to parametrise industrial equipment over a wide range of inlet conditions while still being able to obtain a fast and reasonably accurate prediction of process conditions.

The CRN's predictive ability is tested at an inlet velocity of 50 m/s using the hydrodynamic parameters predicted by the correlation developed. The resulting temperature prediction is given in Figure 13.6.

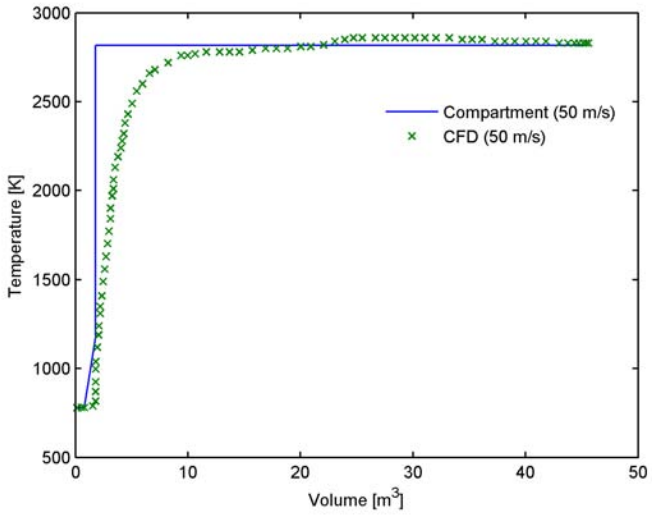


**Figure 13.6:** Interpolation ability of the network at the intersection of $y = 1.15$ and $x = 4.24$ plane

The maximum temperature predicted by the network corresponds well to the CFD simulation in zone 1, 2 and 3. The flame front is not entirely captured by the network due to the non ideal dispersive flow being modelled by a PFR with a back mixing component. The MSE between the CRN and CFD temperature profile was calculated at various inlet velocities and shown in Figure 13.7.

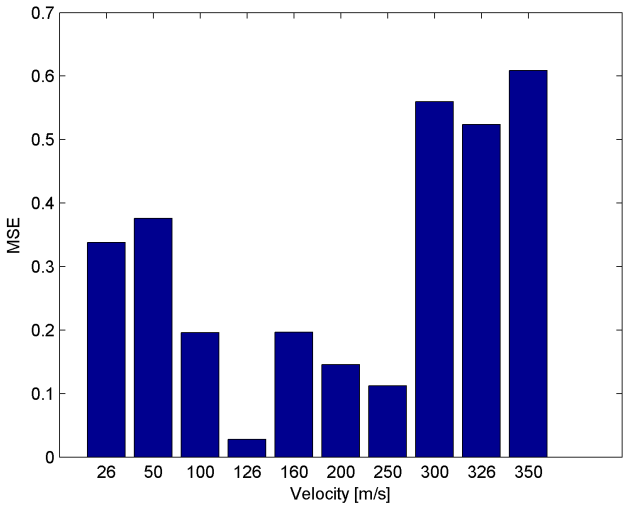


**Figure 13.7:** MSE between the CRN and CFD temperature profile for all inlet velocities

The velocity range is converted to the Reynolds number assuming a constant kinematic viscosity of air at the inlet temperature of 780 K (Equation 13.1).

$$R_e = \frac{uL}{\nu} = u\frac{2}{73.91 \times 10^{-6}} \tag{13.1}$$

The MSE between the CRN and CFD is higher at higher Reylonds numbers ( $> 6.7 \times 10^6$) due to the premature prediction of ignition given by the network. At a Reylonds range of [$2.7 \times 10^6$ - $6.7 \times 10^6$], the model is within reasonable accuracy. In this Reylonds range, the dispersive flow can be approximated using a PFR with a backmixing component as the model. The MSE between the CRN and CFD at Reynolds numbers below $2.7 \times 10^6$ is high since the flow becomes too dispersive for the network to capture.

In terms of CPU time, a mesh resolution of $700,000$ cells takes 8 CPU hours to complete whereas an interpolated network at the same inlet conditions takes 5 CPU seconds to solve. The CRN has the same accuracy as the CFD but is orders of magnitude faster and is more flexible in terms of varying input conditions.

## 13.3 Conclusion

The CRN for the Double inlet reactor was compared to the CFD simulation. The results showed that the CRN results were in good agreement with that of the CFD but solved orders of magnitude faster than the CFD. As such, combustion models developed with the technique are suitable tools in determining optimal designs, particularly in the case of complex geometries.

The CRN for the furnace was correlated over a wide range of inlet velocity conditions. Good agreement of CRN to the CFD model was found to be limited to a subset of inlet velocities, mainly lower inlet velocities since the CRN prematurely predicts the flame front at high inlet velocities. The novel cross-correlation of the network to an inlet condition of the furnace allows the CRN to adapt its temperature prediction orders of magnitude faster than the CFD.

# Part V

# Closure

The computational demand associated with simulating a combustion event is a direct consequence of two key elements, namely the chemical kinetics and computational fluid dynamics. The combustion kinetics consists of thousands of reactions and chemical species making quick evaluation of the reaction rates computationally expensive. The hydrodynamics of the system are traditionally assessed using CFD which is also computationally expensive. In the current study, a reduced kinetic model is proposed to simplify the kinetics and ease the computational demand. For the hydrodynamics, a chemical reactor network is proposed which serves as a surrogate for the hydrodynamics of the system. These simplifications are an attempt to develop a faster solving combustion model while still retaining accuracy. Each of the areas associated with the model development will now be described.

# Chapter 14

# Chemical Kinetics

## 14.1 Mechanism Validation

For the current study, a five-step reduced kinetic mechanism proposed by Schrieber et al. (1994) has been adopted that mimics the features of a detailed chemical kinetic mechanism, namely the phenomena of self ignition, cool flame, and NTC behaviour (Curran et al., 2002) using far fewer elementary reactions and computational resources needed. The reduced model is deemed a suitable alternative to the full kinetic mechanism for incorporation into a chemical reactor network. The reduced kinetic model was successfully validated against experimental data using the batch reactor model. The experimental data available in Schrieber et al. (1994) was used as a basis for kinetic validation and regression of the pseudo species heat capacities.

Thermodynamic properties for each species is needed before applying the compartmentalisation approach. The reduced model proposed by Schrieber et al. (1994) assumes that all the species have the same thermodynamic properties. The current study has further improved the estimation of these thermodynamic properties by using regression analysis.

The thermodynamic properties of the components where applied in the PFR and CSTR sub-models and were successfully validated against a full kinetic mechanism. The idealised sub-models could then trusted in developing the greater chemical reactor network model. The kinetics were further successfully validate in a Rapid Compression Machine (RCM) simulation by comparing the models ignition time delay to the experimental ignition time delay data.

## 14.2 Dynamics

The dynamics of combustion provided a deeper insight into the non-linearity of the kinetic expressions and how the kinetic pathways, high temperature and low temperature,

compete with each other. The results showed a region in which initial oxygen and fuel concentrations can be selected for experimental purposes. The dynamics did not reveal a clear distinction between the low temperature and high temperature kinetics. This may be due to the complex (8D space) interaction between the kinetic pathways and the high non-linearity of the kinetic expressions. The results also confirmed that the kinetics of combustion has a larger temperature feed back as opposed to chemical feedback (Griffiths, 1994). This temperature feed back has implications on the CRN since the CRN is highly dependent on initial temperature.

# Chapter 15

# Hydrodynamics

## 15.1 Computational Fluid Dynamics

Computational Fluid Dynamics (CFD) simulation were required to obtain velocity vector, composition and temperature scalar fields within the domain giving an insight into the hydrodynamics of the system. The CFD vector fields were simulated and used as the basis to conduct the hydrodynamic investigation to propose an equivalent chemical reactor network (CRN). The CFD simulations were also performed at various inlet velocities to ascertain its effect on the vector field and hence, the proposed CRN. This is a novel approach in the current study to correlate the CRN to an input parameter make the CRN more predictive without compromising speed.

In the current study, two geometries were investigated, a simple double inlet reactor and a more advanced furnace geometry. Both geometries under investigation were fully defined in terms of the CFD boundary conditions and relevant kinetic parameters.

The effect of inlet velocity on CFD field was investigated to ascertain whether the proposed CRN structure needed to be updated based on the inlet velocity. It was found that for the simple geometry (Double Inlet reactor) the vector field patterns and flow splits are not affected by the input velocity. This implies that the CRN structure and flow split parameters are not dependent on inlet velocity. Thus, correlation of the CRN to the inlet velocity was not investigated.

For the advanced geometry (Furnace), the vector field patterns (CRN structure) was not affected by the inlet velocity but the flow split parameters of the network were influenced. The flow split parameters were thus correlated to the inlet velocity to further the predictive capabilities of the CRN.

## 15.2 Compartmentalisation

The compartmentalisation uses the vector fields of the CFD simulation to propose an equivalent CRN. The plug flow reactor and the continuous stirred tank reactor models were identified as suitable idealised compartments for the CRN since each represents the opposite extrema in terms of the hydrodynamics properties. The validated reduced kinetic parameters were used in the PFR and CSTR submodels.

Literature revealed that a CRN done by Falcitelli et al. (2002a) considered the reactors in the network to be isothermal at the operative temperature computed from CFD temperature field by using an enthalpy conserving expression. This restricted the predictive nature of their network. An improvement presented in this study was made to allow the ideal reactors to operate at temperatures governed by the differential energy balance giving the current model a more predictive ability. This allows the ideal compartments to thermally interact since the exit temperature from the one compartment determines the inlet temperature to the other compartments.

The modified methodology was applied to the two geometries explained previously. The CRN developed for the double inlet reactor consisted of three PFR sub-models and one CSTR. The PFR's operate at different temperature ranges, high and low temperature pathways. Preliminary results show that the CRN for the double inlet reactor solved orders of magnitude faster than the CFD with good accuracy.

The CRN developed for the furnace consisted of two CSTR's and three PFR's. The CRN for the furnace was mathematically correlated to the input velocity through the network flow split parameters. Once again the CRN solved order of magnitude faster than the CFD model. Good agreement between the CRN and CFD model was found but was limited to a subset of inlet velocities, mainly lower inlet velocities since the CRN prematurely predicts the flame front at high inlet velocities. The novel cross-correlation of the network to an inlet condition of the furnace allows the CRN to adapt its temperature prediction orders of magnitude faster than the CFD.



## 15.3 Conclusion

The simplifications made in the current study are an attempt to develop a faster solving combustion model while still retaining accuracy. Using compartmentalisation as a tool to investigate the hydrodynamics and a reduced kinetic mechanism coupled to the network, a fast solving combustion model has been developed that can be applied to a wide variety of combustion systems ranging from the simple to the complex. The fast solving combustion model makes real time optimisation of a system possible.

# Bibliography

Battin-Leclerc, F., Glaude, P., Warth, V., Fournet, R., Scacchi, G., Come, G., 2000. Computer tools for modelling the chemical phenomena related to combustion. Chemical Engineering Science 55, 2883–2893.

Bird, R., Stewart, W., Lightfoot, E., 2002. Transport phenomena, 2nd Edition. Wiley.

Callahan, C., Held, T., Dryer, F., Minetti, R., Ribaucour, M., Sochet, L., Faravelli, T., Gaffuri, P., Ranzi, E., 1996. Experimental data and kinetic modeling of primary reference fuel mixtures. In: Twenty-Sixth Symposium (International) on Combustion/The Combustion Institute.

Chen, K., Karim, G., 1998. Evaluation of the instantaneous unsteady heat transfer in a rapid compression-expansion machine. Tech. rep., Department of Mechanical Engineering, University of Calgary, Alberta, Canada.

Claudel, S., Fonteix, C., Leclerc, J., Lintz, H., 2003. Application of the possibility theory to the compartment modelling of flow pattern in industrial processes. Chemical Engineering Science 58, 4005–4016.

Curran, H., Gaffuri, P., Pitz, W., Westbook, C., 2002. A comprehensive modeling study of iso-octane oxidation. Combustion and Flame 129, 253–280.

Duran, A., Carmona, M., Monteagudo, J., 2004. Modelling soot and sof emissions from a diesel engine. Chemosphere 56, 209–225.

Falcitelli, M., Pasini, S., Rossi, N., Tognotti, L., 2002a. Cfd + reactor network analysis: an integrated methodology for the modeling and optimisation of industrial systems for energy saving and pollution reduction. Applied Thermal Engineering 22, 971–979.

Falcitelli, M., Pasini, S., Tognotti, L., 2002b. Modelling practical combustion systems and predicting nox emissions with an integrated cfd based approach. Computers and Chemical Engineering 26, 1171–1183.

Griffiths, J., 1994. Reduced kinetic models and their application to practical combustion systems. Prog. Energy Combust. Sci. 21, 25–107.

Grosschmidt, D., Habisreuther, P., Bockhorn, H., 2007. Calculation of the size distribution function of soot particles in turbulent diffusion flames. Proceedings of the Combustion Institute 31, 657–665.

Kahandawala, M., Corera, S., Williams, S., Carter, C., Sidhu, S., 2006. Investigation of kinetics of iso-octane ignition under scramjet conditions. Tech. rep., Department of Mechanical and Aerospace Engineering, University of Dayton.

Kee, R., 2003. Chemically reacting flow : theory and practice. John Wiley & Sons.

Kirk-Othmer, 2001. Encyclopedia of Chemical Technology: Combustion science and technology. Wiley.

Law, C., 2007. Combustion at a crossroads: Status and prospects. Proceedings of the Combustion Institute 31, 1–29.

Lee, D., Hochgreb, S., 1998. Rapid compression machines: Heat transfer and suppression of corner vortex. Combustion and Flame 114, 531–545.

LeMoullec, Y., Gentric, C., Potier, O., Leclerc, J., 2010. Comparison of systemic,compartmental and cfd modelling approaches: Application to the simulation of a biological reactor of waste water treatment. Chemical Engineering Science 65, 343–350.

Machrafi, H., Lombaertb, K., Cavadiasa, S., Guibertb, P., Amouroux, J., 2005. Reduced chemical reaction mechanisms: experimental and hcci modelling investigations of autoignition processes of iso-octane in internal combustion engines. Fuel 84, 2330–2340.

Mattiussi, C., 2002. Reference discretization strategy for the numerical solution of physical field problems. Advances in imaging and electron physics 121, 143–279.

Menter, F., Kuntz, M., Langtry, R., 2003. Ten years of industrial experience with the sst turbulence model. In: Turbulence, Heat and Mass Transfer 4. Begell House.

Mittal, G., 2006. A rapid compression machine - design, characterisation and autoignition investigations. Ph.D. thesis, Department of Mechanical and Aerospace Engineering: Case western reserve university.

Muller, U., Peters, N., Linan, A., 1992. Twenty fourth symposium (international) on combustion. In: The Combustion Institute, Pittsburgh.

Owston, R., Magi, V., Abraham, J., 2007. A numerical study of thermal and chemical effects in interactions of n-heptane flames with a single surface. Combustion and Flame 148, 127–147.

Peters, N., 2000. Turbulent combustion. Cambridge University Press.

Ponsich, A., Azzaro-Pantel, C., Domenech, S., Pibouleau, L., Pigeonneau, F., 2009. A systemic approach for glass manufacturing process modeling. Chemical Engineering and Processing 48, 1310–1320.

Ranade, V., 2002. Computational flow modelling for chemical reactor engineering. Academic press.

Ranzi, E., Faravelli, T., Gaffuri, P., Sogaro, A., D'Anna, A., Ciajolo, A., 1997. A wide-range modeling study of iso-octane oxidation 108, 24–42.

Schrieber, M., Sakak, A., Ligens, A., Griffiths, J., 1994. A reduced thermochemical model for the autoignition of fuels with variable octane ratings. In: Twenty-Fifth Symposium (International) on Combustion. pp. 933–940.

Shampine, L., Reichelt, M., 1997. The matlab ode suite. Tech. rep., Mathematics Department, Southern Methodist University, Dallas.

Singha, J., Balthasara, M., Krafta, M., Wagnerb, W., 2005. Stochastic modeling of soot particle size and age distributions in laminar premixed flames. Proceedings of the Combustion Institute 30, 1457–1465.

Tanaka, S., Ayala, F., Keck, J., 2003. A reduced chemical kinetic model for hcci combustion of primary reference fuels in a rapid compression machine. Combustion and Flame 133, 467–481.

Tu, J., Yeoh, G., Liu, C., 2008. Computational Fluid Dynamics: A Practical Approach. Elsevier.

Turns, S., 2000. An introduction to combustion: Concepts and applications. McGraw-Hill.

Veynante, D., Vervisch, L., 2002. Turbulent combustion modeling. Progress in Energy and Combustion Science 28, 193–266.

Warnatz, J., Deutschmann, O., 2005. Detailed kinetic modelling of the oxidation and combustion of large hydrocarbons using an automatic generation of mechanisms. Master's thesis, Universität Heidelberg.

Warnatz, J., Maas, U., Dibble, R., 2006. Combustion: Physical and chemical fundamentals, Modeling and simulation, Experiments, Pollutant formation, 4th Edition. Springer.

Wells, G., Ray, W., 2005. Methodology for modeling detailed imperfect mixing effects in complex reactors. American Institute of Chemical Engineers 51, 1508–1520.

Westbrook, C., Mizobuchi, Y., Poinsot, T., Smith, P., Warnatz, J., 2005. Computational combustion. Proceedings of the Combustion Institute 30, 125–157.

Widenhorn, A., Noll, B., Aigner, M., 2008. Numerical characterization of the reacting flow in a swirled gasturbine model combustor. In: High Performance Computing in Science and Engineering. Springer.

Zienkiewicz, O., Taylor, R., 2000. The Finite Element Method, 5th Edition. Vol. 3. Butterworth Heinemann.

Zucca, A., Marchisioa, D., Barresia, A., Foxb, R., 2006. Implementation of the population balance equation in cfd codes for modeling soot formation in turbulent flames. Chemical Engineering Science 61, 87–95.